Atomic and Molecular Ions with Photon Resonators for Quantum Information Science

by

Molu Shi

B.S. Physics and Mathematics
University of Toronto, 2009

Submitted to the Department of Physics
in partial fulfillment of the requirements for the degree of

Doctor of Philosophy

at the

MASSACHUSETTS INSTITUTE OF TECHNOLOGY

September 2015

Signature redacted

Author .....
Department of Physics
Aug 28, 2015

Signature redacted

Certified by.....
Isaac L. Chuang
Professor, Departments of Physics and EECS
Thesis Supervisor

Signature redacted

Accepted by .....
Nergis Mavalvala
Professor of Physics, Associate Department Head for Education

Atomic and Molecular Ions with Photon Resonators for Quantum Information Science

by

Molu Shi

Submitted to the Department of Physics
on Aug 28, 2015, in partial fulfillment of the
requirements for the degree of
Doctor of Philosophy

Abstract

With continued development of laser-atom interaction, systems of trapped ions offer a promising platform for the realization of fault-tolerant quantum information processing (QIP). Much progress with single atomic and molecular ion qubits has been made both in theory and experiment on the fundamental building blocks for scalable QIP architectures. Nonetheless, difficulty still remains for quantum network implementation and spectroscopy protocols for atomic and molecular ions, respectively. The objective of this thesis is to design and test the ion trap integration with photon resonators, which can facilitate coherent ion-photon state transfer in quantum networks, and microwave spectroscopy for molecular ion rotational states.

The first part of the thesis describes a novel planar trap design with an integrated optical cavity. Proposals for photon number memory with trapped ions are presented, and experimental implementation for single ion cavity QED is explored. In addition, a study of vacuum-induced scattering loss increase is performed for mirror coatings at several temperatures and wavelengths, from which a method of retaining cavity finesse was developed.

In the second part, an experiment is proposed for microwave quantum logic spectroscopy of molecular ions. With a cavity field to facilitate entanglement between co-trapped single atomic and molecular ions, a reliable and non-destructive spectroscopy method, as well as molecular ground state cooling can be realized.

Thesis Supervisor: Isaac L. Chuang
Title: Professor, Departments of Physics and EECS

Acknowledgments

I owe my thanks to many people, without whom the thesis is not possible. I thank my adviser Prof. Isaac Chuang, who introduced me to the field of quantum information science in 2009, and has continuously advised my research ever since, with patient guidance, inspiring insights, and secured funding support. It has been a great opportunity working with Ike to have the freedom to explore theoretical as well as experimental aspects in quantum information science. I also want to express my thanks to Prof. Vladan Vuletić and Prof. Marin Soljačić as my thesis committee members, who offered insightful feedback on my projects. I need to thank Prof. Leonid Levitov as well, who has served as my academic adviser for six years and always pointed to me the right departmental resources when need.

The tremendous help I received from my lab mates must also be acknowledged. I entered MIT with little experimental experience. Peter Herskind mentored me on almost every single aspect on how to become an AMO physicist, from soldering electronic components to operating an ion trapping experiment. Shannon Wang, Tony Kim and Paul Antohi were extremely useful resources for my training in linux and python programming, electronics, and mechanical design. I followed Yufei Ge and Shannon Wang through many trap fabrication processes, the experience of which lead to the recipe developed for the trap in my experiment. Many thanks should also be given to my lab partner Michael Gutierrez, who I collaborated the most at MIT. His dedication on most software development and the lab laser system maintenance is essential for our experiment. I should also thank Tailin Wu and Helena Zhang, who continue to make progress in our experiment with Michael in the past year. Lots of my insight in research also comes from helpful discussions with Amira Eltony, Jeff Russom, Hans H. Andersen, Anders Mortensen, Dorian Gangloff, Alexei Bylinskii, Adam McCaughan, and many students, postdocs, and faculties at MIT CUA. Special thanks should also be given to many technicians and staffs at CUA, NSL, MTL, CMSE, Physics department, and many MIT machine shops for their friendly technical and administrative supports.

I would also like to thank all my friends from MIT Fuyun Chinese Comedy Club, for their strong supports during my founding and chairing period, and for their efforts in maintaining the club after I stepped down. I need to thank those who gave me invaluable help to recover from the health crisis in summer 2013, especially Su Wang and Mingyu Xue.

Of course, my deepest thank should be given to my parents, who encouraged me to pursue education after high school in 2005, and supported me financially ever since. This thesis is dedicated to them, together with my wife Yi Wang, my other biggest discovery during my PhD.

Contents

List of Figures

List of Tables

Part I

Introduction

Chapter 1

Introduction

Ever since man wrote down their first equations, it has become an integral part of human nature to describe the observed with mathematical models, and to predict the unknowns through computation. With continued expansion of the horizon of the explored mathematical world, the scale and complexity of computation, and hence our desire for faster and more reliable computational tools escalates as well. On the other hand, the investigation in new computational technologies never stops. Each breakthrough in algorithm or computational hardware development in the history has always triggered revolutionary advancement in all scientific fields. Today, as the world enters the information era and our exploration of nature moves into the quantum level, the demand of computational power has again quickly exponentiated [Fey48]. Although much effort remains to improve the current computational architecture [Chu36, Tur38, Sha48] and the efficiency of electronic computers still grow promisingly as Moore's law[Moo65], many researches have focused on exploring new ways of computing.

As one most promising model, quantum computing is shown in many cases, to be able to result in exponential faster algorithms than those based on electronic computers. The key difference underlying this intriguing advantage lies in the new way information is encoded in quantum computers. Unlike in electronic (classical) computers where a bit assumes two states, a quantum bit (qubit) is represented by

a unit vector in a two dimensional complex plane. Quantum information encoded in an n-qubit system therefore lives in a 2^n-dimensional complex space spanned by the tensor product of n qubits. Compared to the 2^n memory of an n-bit classical computer, the encoding in this much richer space also allows for the possibilities of new efficient algorithms.

With the concept proposed to efficiently simulate quantum mechanical systems [Fey48, Llo96], quantum computing has found potential applications in many fields such as database search [Gro97], factoring of large numbers [Sho83], and systems of linear equations [HHL09]. On the other hand, tremendous efforts have been made to search for the optimal implementation of quantum computers. Different prototypes have been constructed from a variety of quantum systems, including quantum optics [CY95, O'B07], nuclear magnetic resonances [GC97, VSB+01], Josephson junctions [MOL+99, MNAU02], neutral atoms [BCJD99, ALB+07], and trapped atomic [CZ95, WMI+98] and molecular ions [DeM02, YN13]. The goal was not only to realize the advantage in processing efficiency for a single quantum computer, but also to implement a scalable quantum network, with reliable interconnections allowing for communications among individual computers.

This thesis investigate two models in quantum computing systems, trapped atomic and molecular ions, and the use of photon resonators for quantum interconnect implementation and qubit operation improvement. In this chapter, we give a brief introduction to quantum information science using trapped atomic and molecular ions, and outline the scope of this thesis.

1.1 Quantum information science

Quantum information science (QIS) seeks to construct a new information architecture based on the law of quantum mechanics, for computation and communication. Similar to electronic computers, the most elementary component of a quantum computer is a binary register, called a *quantum bit*, or for short, a *qubit*. This conceptual binary

register is composed of two discrete quantum levels $|\downarrow\rangle$ and $|\uparrow\rangle$, which in general, can be thought of as any two level system such as the two polarization states of a photon [CY95], or two spin states of a nucleus [GC97]. Binary (or gate) operations on qubits are facilitated via their coupling to external excitation, which flips the qubit state from $|\downarrow\rangle$ to $|\uparrow\rangle$ and vice versa. For instance, in the case of a nuclear or photon qubit, qubit flips are done through polarizing optics, and resonant magnetic field coupling, respectively. A wave function $|\psi\rangle$ for this two-level system can be written as a superposition of $|\downarrow\rangle$ and $|\uparrow\rangle$:

$$|\psi\rangle = |\downarrow\rangle + e^{i\phi}\beta|\uparrow\rangle, \tag{1.1}$$

where the information is encoded in the complex plane spanned by the relative phase $e^{i\phi}$. For multiple qubits, the total wave function $|\Psi\rangle$ is represented by the tensor product of wave functions for each individual qubits, resulting in a 2^n dimensional space for information encoding. Because of this new representation of information, many efficient algorithms for applications inaccessible by classical information processing have been discovered [Fey48, Sho83, Llo96, Gro97, HHL09].

1.1.1 Qubit implementation

While quantum computers offer exciting advancement in information science, the experimental implementation can be quite challenging. Although conceptually, all two level systems can be considered as qubits, the way they can respond to external fields set further benchmarks to their candidacy for experimental implementation. On one hand, because of undesired coupling to environment noise (decoherence), most two level system approximations are only accurate within the excited state life time (decoherence time). To reduce computational errors in this time frame, desired quantum systems should use minimal time for computation relative to decoherence. On the other hand, coupling to a third stable quantum state might be necessary in many systems, to allow for measurement to distinguish the binary states $|\downarrow\rangle$ and $|\uparrow\rangle$. A more comprehensive list, known as the DiVincenzo criteria is com-

piled in Ref. [DiV00], based on which different quantum systems have been proposed and tested for qubit implementation. This includes for instance, polarization states of photons [CY95, O'B07], spin states of nuclei [GC97, VSB+01], phase and flux states in Josephson junctions [MOL+99, MNAU02], and assemble states of atom clouds [BCJD99, ALB+07]. In Sec. 1.2, we explain in particular the implementation with trapped atomic [CZ95, WMI+98] and molecular ions [DeM02, YN13].

1.1.2 Network of quantum computers

Similar to a conventional computer network, a quantum network consists of three parts: 1) quantum computers as the network nodes, 2) quantum channels for information transmission, and 3) interconnects between the computers and interconnects to map information between stationary and flying qubits. The importance for establishing a quantum network is not only for long-distance quantum state teleportation [BBC+93], but for its key role in distributed computation and secure communication.

As in a classical computer network, distributed quantum computation provide computing resources equally over the network, which overcomes any constraints on local quantum computers. Distributed computation also allows for more efficient information processing [CEHM99]. In particular, the overall space for information grows exponentially with the size of the quantum network, vs linearly in a classical computer network [Kim08]. While for a network of k classical computers, each with n bits of RAM, the total dimension of state space grows as $k2^n$, a quantum network with equal size can have a state space dimension of 2^{kn}.

Another advantage of a quantum network is that secure communication prototcol can be established for cryptographic key distribution [BB14]. By randomizing the measurement bases of transmitted and received photon qubits, and confirming selected measurement results for common bases, eavesdropping activities can be faithfully detected, and shared keys can be securely distributed.

1.2 Ion trap implementation

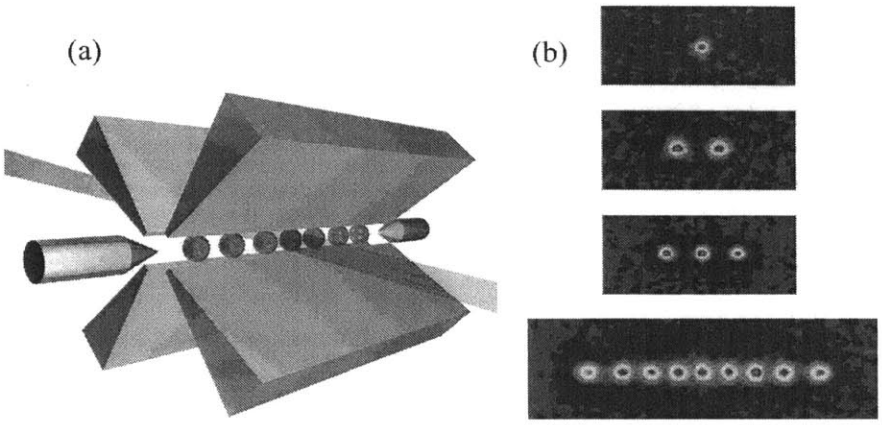

Figure 1-1: (a) Schematic showing a linear ion chain confined in an ion trap (linear Paul trap) consisting of four RF electrodes and two end-cap (DC) electrodes. A laser beam is shown to address a single ion qubit transition. (b) Camera images of few ions. Images by courtesy of University of Innsbruck.

Trapped ions have now become one of the most promising qubit implementations for QIS. Figure 1.2 shows a schematic of atomic ions trapped in a Paul trap. In such architecture, ionized atoms or molecules are spatially confined in radio frequency (RF) electromagnetic fields. Qubit transitions are chosen between the ground and a meta-stable internal state of the ions. Coherent light sources are used to to facilitate qubit state flips, and to further reduce the ions' kinetic energy for stable confinement via Doppler cooling. The scattered photons from the ions during Doppler cooling can be used for ion imaging and qubit state detection.

Because the trapped ion system can be enclosed in an ultra-high vacuum (UHV) environment (typically 10^{-10} - 10^{-11} torr), background noise disturbance to the quantum system can be significantly reduced; and because of the stable spatial confinement, qubit state detection signals can be averaged over sufficient time to improve the signal to noise ratio (SNR). Furthermore, the stable isotope structure allows for the replication of identical qubit copies, making it possible to construct a scalable quantum computing architecture. Since the advantage of trapped-ion systems are considered in the original proposal by Cirac and Zoller [CZ95], continued progress

has been made towards experimental implementations, with atomic and molecular ions, respectively. Because of the rich level structure in polar molecules involving vibration and rotational states, the techniques to manipulate both the internal and external states are quite different for atomic and molecular ions. We show the state-of-art proposals and experimental implementations for both systems in Sec. 1.2.1 and Sec. 1.2.2

1.2.1 Atomic ions

Two types of transitions are commonly chosen for qubit implementation in atomic ion systems: electric quadruple, and magnetic dipole transitions (See for instance, Ref. [MSW+08] and Ref. [HAB+14]) [1]. In both implementations, the Hamiltonian governing the laser-ion interaction are well characterized. For system scaling, 2D arrays [KMW02] of trapped ions based on microfabricated ion trap chips [CBB+05] have been proposed, and the scheme of entangling adjacent ions via Coulomb interactions has implemented in various experiments with linear chains of ions [SKK+00, HHR+05]. Besides the qubit transition (internal) in trapped ions, the motional state (external) is usually involved in QIS, especially for ion entanglement operations [Hom06]. Optical pumping and sideband cooling [DBIW89] are used, for the internal and external state initialization, with the state-of-art fidelity (see Ref. [NC00] for definition) of 99.991% [MSW+08] and 99.9% [Roo00] achieved, respectively. As a more accurate figure of merit for gate-to-coherent time ratio with all noise source included, the gate fidelity for both optical [MSW+08] and spin [HAB+14] qubits have been measured close to unity for single qubit gates, allowing for fault tolerant quantum computing [Sho]. Because any multiple qubit gate can be re-expressed as a sequence of single qubit gates and CNOT gates [DiV00], implementations of the two in many experiment such as Ref. [HAB+14, BHLL14] can sufficiently provide a universal set of quantum gates. Individual qubit addressing has been demonstrated in many experiment involving multiple trapped ions in linear chains as well [SKK+00, HHR+05].

[1] also referred as optical and spin qubit, respectively

For quantum network implementation, current experimental efforts focus on implementing proposals for both deterministic [CZKM97, Kim08] and probabilistic [DLCZ01] approaches. For the former, photon resonators (usually Fabry-Pérot cavities) are used as quantum interconnects between network nodes and channels. Mapping between stationary (ion) and flying (photon) qubits is facilitated via strong coupling in the framework of cavity quantum electrodynamics (cavity QED, see Chap. 3). Although cavity QED has been demonstrated in photon resonators with ion crystals [HDM+09], single ion cavity QED still remains to be implemented. For the latter, projective measurement on the ion emitted photons over the network is used to generate heralded entanglement between ions. Although first experimental demonstrations [MMO+07] have low yields in entangled ion pairs due to limited light collection efficiency, continued progress has been made recently to increase the limit via optical cavities [CSF+13, MRR+14].

1.2.2 Polar molecular ions

The rotational states of molecules are promising candidates for qubit implementation. Continued progress on experimental verification of DiVincenzo criteria has been made since DeMille's proposal [DeM02]: Using a planer trap architecture, scalable quantum computing can be realized in similar ways as atomic ions, with qubit transitions addressed by coherent microwave [SHDC13] or Raman [DM12, Lei12] laser sources, and ion-ion interactions facilitated via Coulomb forces. In terms of gate fidelity, on one hand, similar to atomic ion spin qubits, the microwave qubit level spacing for trapped molecular ions suggests a coherent time of several hundreds of ms [SBC+11]. In addition, the small magnetic moments due to the large nuclear mass (opposed to that of electrons) also imply less sensitivity to magnetic field noise, compared to atomic ion spin qubits. On the other hand, a fast gate time (~ns) can still be obtained due to the permanent large dipole moment of polar molecular ions. Sec. 7.2.1 in Chap. 7 shows an example for $SrCl^+$ molecules. Arbitrary single qubit rotations can be implemented via microwave addressing, and similar to atomic ions, Coulomb interactions

between trapped ions can be used for CNOT gate implementation, resulting in the bases for universal quantum gate construction. Two flying qubits are envisioned for polar molecular ion based quantum networks. For short distances (several meters), polar molecules can couple to single microwave photons in microwave cavities integrated to planar ion traps [SBC+11, Ant11], which can directly be used for remote entanglement generation. Although not specific to polar molecules, single microwave photon generation [HSG+07], detection [JRH+10, BLS+10], and remote qubit entanglement generation [RSM+14] have all been demonstrated in experiments. For long distance, microwave photons can be converted to optical photons via e.g. an opto-magneto-mechanical quantum interface [XVT14], and transmitted through optical fibers.

Although showing great promise for scalability, gate fidelity, universal gate and flying qubit implementation, it is difficult to implement an efficient spectroscopy method for polar molecules for state initialization and detection. Several indirect spectroscopic approaches are proposed [DM12, Lei12, SHDC13], but only a few realized in experiment [CGD+10]. Furthermore, due to the long wavelength of microwaves, individual qubit addressing can be non-trivial. Raman lasers can be used in place of microwaves, which however trades off the compatibility of all-on-chip microwave integration.

1.3 Thesis scope and contributions

This thesis is outlined as follows:

Part I of the thesis presents an introduction to quantum information science and basic ion trapping technologies. In particular, besides the brief overview of QIS in the proceeding sections in this chapter, Chapter 2 describes the dynamics of trapped ions, and the coupling between the ion internal and motional states.

Part II and Part III present the thesis contributions to QIS with atomic and molecular ions, respectively.

1.3.1 Atomic ion and optical cavity

Part II of this thesis work contributes partial solutions to the following challenges for QIS with atomic ions.

Two-ion quantum node for two-photon quantum memory

In a deterministic quantum network [CZKM97, Kim08], quantum state of single photons can be mapped to single ions via strong coupling in optical cavities. With multiple ions, not only can the ion-photon coupling be enhanced, the quantum state of multiple photon states can be converted and stored with ions. In Chapter 3, after a brief overview of the formalism of ion-photon interaction, we present an experiment design where using two ions, a two-photon quantum memory can be realized in the deterministic quantum network architecture. In particular, detailed pulse sequence and analysis of experimental feasibility with $^{88}Sr^{+}$ ions are presented.

Microfabricated ion traps with optics integration

An important step towards single-ion-single-photon interconnect in an deterministic quantum network is to realize cavity QED for a single trapped ion. Although experimental demonstration on cavity QED has been achieved for ion crystals [HDM+09] and single neutral atoms[Kim98], it remains difficult for single trapped ions. To get a sufficiently large coupling efficiency in a stable cavity configuration, a close distance between ions and cavity mirror(s) is required. This can result in photo-induced charging on the mirror dielectric surfaces, which can affect trapping stability and induce undesired micromotions [WHL+11].

One possible solution provided in this thesis is a novel design of cavity-trap system. With a planer ion trap fabricated directly on a mirror surface, and leaving an small aperture on the central ground electrode, a stable short cavity can be formed with a waist of several microns. The ion exposure to dielectric material, and hence possible charging issues are minimized to the size of the aperture. With the promising results

from our proof-of-principle experiment at cryogenic temperature [HWS+11], Chap. 4 in this thesis presents an implementation at room temperature, which avoids possible ion-cavity alignment during temperature cycles necessary for cryogenic systems, and paves the way for optical cavity integration.

Cavity finesse decay and recovery in high vacuum systems

Another challenge for ion-photon interfaces is to construct and maintain a high finesse optical cavity in UHV systems. The state-of-art technology to fabricate high reflectivity mirrors for optical cavities uses Ta_2O_5 and SiO_2 alternating dielectric layer coatings, and typically finishes the coating with Ta_2O_5 for its higher index of refraction [Sit83, RTKL92]. Evidence from many experiments have shown a scattering loss increase for this type of coatings under UHV [SLM+12, BMS+13, CBK+13, Cet11], which can strongly affect QIS experiments. Moreover, no experiments have yet been performed to understand the scattering loss increase mechanism in such systems, nor to reverse the incurred loss efficiently.

In this thesis, we also constructed an experiment to study this loss mechanism under controlled vacuum pressure and temperature, and obtained result to support our hypothesis that the incurred loss is due to oxygen depletion from surface oxides. An in-situ method to recover the optical cavity from the induced scattering loss as well. This experiment is presented in Chap. 5

1.3.2 Molecular ion and quantum logic spectroscopy

In part III of the thesis, partial solutions are given to the challenge of molecular ion rotational state spectroscopy.

For QIS with polar molecular ions, single ion rotational state spectroscopy (readout and initialization) and individual ion addressing can be challenging, because of the lack of close transitions, and longer wavelength of microwave fields than typical ion spacing.

We proposed a scheme to use quantum logic spectroscopy [SRL+05] to overcome both challenges. When co-trapped with a single atomic ion, entanglement through their common motional bus can be used to map quantum states between the two. Therefore, readout and initialization of the molecule can be facilitated by heralded measurement on the atom. A spatially varying AC stark shift field by a laser field is used to enhance the internal-to-motional state coupling for the molecular ion. Furthermore, the switching of this field can turn on/off the inter-ion quantum state mapping, and hence provide single molecular qubit addressing, despite the long microwave wavelength. This method can also be used for ground state cooling in molecular ion rotational states. The work is presented in Chap. 6 and Chap. 7.

1.4 Contributions of coworkers

All above works are completed through collaborations with my co-workers.

The project on optics-integrated traps was initiated by Peter Herskind based on David Leibrandt's original proposal, and Peter's leadership continued till the mid phase of the second half of the project - for tests at room temperature. Shannon Wang led the trap tests for the first phase at cryogenic temperature. During the second phase of experiment at room temperature, Michael Gutierrez designed and simulated the new trap, and together with Richard Rines, and Helena Zhang, provided great support in terms of maintaining the laser optics, pulse programmer, and other control software for the experiment. I also followed Yufei Ge to practice nanofabrication techniques till the early phase of the second experiment.

The work on cavity loss studies is completed through collaboration with the Vuletić lab. Dorian and his coworkers performed half of the experiment with cavities tested for coatings for 370 nm lasers. Michael Gutierrez helped to simplify the experiment complexity and programmed the first script to allow for automatic data analysis. Kai Aichholz helped to write the graphical user interface for one function generator control software. Tailin Wu operated part of the experiment with me, and is currently

leading the project for further studies.

The theoretical work of molecular ion spectroscopy was initiated by Peter, who formulated the framework of effective Lamb Dicke parameter generation. Prof. Michael Drewsen provided ideas to simplify the spectroscopy protocol.

My advisor Isaac Chuang contributed great insights, and initiated the collaborations throughout all projects.

1.5 Publications

The following is a full list of my publications related to this thesis work.

1. D. Ganloff, M. Shi, et al, *Preventing and Recovering from Vacuum-induced Optical Losses in Ta_2O_5 Mirror Coatings*, Vol. 23, Issue 14, pp. 18014-18028 (2015)

2. A. Eltony, D. Ganloff, M. Shi, et al, *Technologies for trapped-ion quantum information systems*, arXiv:1502.05739 (2015)

3. M. Shi, et al, *Microwave quantum logic spectroscopy and control of molecular ions*, N. J. Phys. 15(2013) 113019

4. P. F. Herskind, S. X. Wang, M. Shi, et al., *Microfabricated surface ion trap on a high-finesse optical mirror*, Opt. Lett. 36, 3045-3047 (2011)

Chapter 2

Ion trapping fundamentals

Since its ground breaking experiments in 1950's for mass spectroscopy [Pau90], ion traps has provided breakthrough technologies for manipulation of single quantum particles [Win13]. For trapped-ion quantum computers, stable trapping at UHV is essential. The long ion storage time allows for better spectroscopy signals averaging. The spatial confinement provides stable overlap with the laser fields for cooling and qubit addressing, and the fine control of quantized harmonic motion enables all two qubit gates based on Coulomb interactions. In this Chapter, we overview the theoretical background of the ion trapping techniques.

2.1 Trapped ion dynamics

Because the solution to Laplace's equation does not allow local potential minima in static electric fields, a time-dependent field is needed to provide 3D ion confinement. A fast oscillating field (typically RF frequency) in a linear Paul trap can result in stable trapping in certain regime, where the ion motion can be approximated by a superposition of harmonic motion in a pseudo static potential, and an oscillation with the same frequency as the RF field. We present below an analytic formalism to illustrate some basic aspects of ion trapping dynamics.

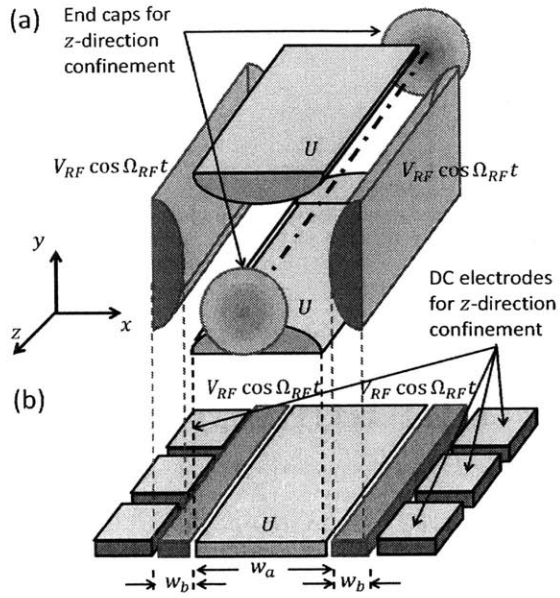

Figure 2-1: (a) Standard linear Paul trap geometry. The cross-section of the trap electrode inner surface forms a hyperbola defined in Eq. 2.1. With DC and RF potential applied on the electrodes, ions can be confined in the x-y plane at the hyperbolic center. Confinement in the z-direction can be realized using DC voltage end caps. (b) With the electrodes reconfigured on the same plane (top electrode removed, and potential at infinity is taken at zero DC), similar quadruple field for trapping can be realized.

2.1.1 Paul traps

The standard configuration of a linear Paul trap can be found in Fig. 2.1-a , where the edge of the electrode cross-section form a symmetric hyperbola, with the origin located at the trap center:

$$\frac{x^2 - y^2}{r_0^2} = \pm 1. \tag{2.1}$$

With one pair of electrodes biased with an RF potential $V_{RF}\cos(\Omega_{RF}t)$, and the other pair biased with DC potential U, the potential near the trap center follows

$$\phi_r(x, y, t) = \frac{x^2 - y^2}{2r_0^2}(U - V_{RF}\cos(\Omega_{RF}t)). \tag{2.2}$$

The xy-plane, or typically referred as radial motion of an ion with charge Q and mass m driven by such potential is governed by the standard Mathieu equation

$$\begin{aligned} \frac{d^2x}{d\tau^2} + (a - 2q\cos(2\tau))x = 0, \\ \frac{d^2y}{d\tau^2} - (a - 2q\cos(2\tau))y = 0, \end{aligned} \tag{2.3}$$

where the dimensionless parameters follow

$$q = \frac{2QV_{RF}}{mr_0^2\Omega_{RF}^2}, \quad a = \frac{4QU}{mr_0^2\Omega_{RF}^2}. \quad \tau = \Omega_{RF}t/2. \tag{2.4}$$

In the regime where $a \ll q \ll 1$ (typically U is set to ground and hence $a = 0$), an approximate solution for Eq. 2.3 can be obtained by separating the ion motion into a large-amplitude slow motion, and small-amplitude fast motion. In particular, with

$$r_i = \rho_i + \delta_i\cos(2\tau), \quad r_i = \{x, y\}, \tag{2.5}$$

Equation 2.3 gives

$$\frac{d^2}{d\tau^2}(\rho_i + \delta_i\cos(2\tau)) \pm (a - 2q\cos(2\tau))(\rho_i + \delta_i\cos(2\tau)) = 0,$$

and hence

$$\delta_i = \mp q\rho_i/2, \tag{2.6}$$

where we have neglected the terms $d^2\rho_i/d\tau^2$, a, and $\delta_i\cos(2\tau)$, respectively, and approximated $\int 2q\cos(2\tau)\rho_i d\tau = \rho_i \int 2q\cos(2\tau)d\tau$ for short time scales.

For the large-time-scale motion, by substituting Eq. 2.6 back to 2.3 and averaging out the fast oscillation, we get

$$\begin{aligned} \frac{1}{\pi}\int_0^\pi d\tau \frac{d^2}{d\tau^2}(\rho_i + \delta_i\cos(2\tau)) &= \mp\frac{1}{\pi}\int_0^\pi d\tau(a - 2q\cos(2\tau))\left(1 \mp \frac{q}{2}\cos(2\tau)\right)\rho_i \\ \frac{d^2\rho_i}{d\tau^2} &= -(q^2/2 \mp a)\rho_i \simeq -\frac{q^2}{2}\rho_i, \end{aligned} \tag{2.7}$$

where again, for short-time-scale averaging, we approximated $\int d\tau \rho_i = \rho_i \int d\tau$. The solution of this decoupled differential equation takes a form of simple harmonic oscillation, with an effective potential

$$\Phi = \frac{1}{2} m \left[\frac{q\Omega_{RF}}{2\sqrt{2}} \right]^2 (x^2 + y^2), \tag{2.8}$$

and frequency

$$\omega_{sec,r} = \frac{q\Omega_{RF}}{2\sqrt{2}} \tag{2.9}$$

The fast and slow oscillation $\delta_i \cos(2\tau)$ and ρ_i are referred as the micromotion and radial secular motion of the trapped ions, which oscillate at the RF frequency Ω_{RF} (See Eq. 2.4), and secular frequency $\omega_{sec,r}$. The effective potential Φ is called the pseudo potential. Another useful quantity in trap characterization is the trap depth, defined as

$$\Phi_0 = \frac{1}{2} m\omega^2 r_0^2 = \frac{Q^2 V_{RF}^2}{4mr_0^2 \Omega_{RF}^2}. \tag{2.10}$$

This approximate solution is valid only in the regime $a \ll q \ll 1$. In general, bound trajectories of ion motion exist in a closed region in the q-a space, which can be obtained using analytic or numerical methods [Bar03]. Illustration of ion motions with several large values of q's and a's can be found in Ref. [Kim11], via numerical solutions.

In the z (axial) direction, two end caps orthogonal to the z-axis with equal DC potentials placed at $\pm z_0$ can be used to confine the motion. In the approximation that these end caps have infinite areas, the resultant potential $\phi_a(z)$ does not affect the ion dynamics in the xy-plane, and the motion in the z-direction can be approximated with a simple harmonic oscillation, with an axial secular frequency $\omega_{sec,a}$ given by

$$\omega_{sec,a} = \frac{\sqrt{a_z}\Omega_{RF}}{2}, \quad a_z = \frac{4Q}{m\Omega_{RF}^2} \left[\frac{d^2\phi_a(z)}{dz^2} \right]_{z=0}. \tag{2.11}$$

2.1.2 Surface electrode traps

In surface electrode ion traps, similar trapping potentials can be generated with the trap electrode configuration shown in Fig. 2.1-b. For such symmetric electrode configuration, analytic forms of the the trap parameters can be determined by the field (DC, and RF, respectively) and trap geometry [Hou08]. In particular,

$$q = \frac{16QV_{RF}}{\pi m\Omega_{RF}^2}\frac{w_b}{(w_a+w_b)^2\sqrt{w_a(w_a+2w_b)}}, \tag{2.12}$$

$$\Phi_0 = \frac{Q^2V_{RF}^2}{\pi^2 m\Omega_{RF}^2}\left[\frac{w_b}{(w_a+w_b)^2+(w_a+w_b)\sqrt{2w_aw_b+w_a^2}}\right]^2, \tag{2.13}$$

$$y_0 = \frac{1}{2}\sqrt{2w_aw_b+w_a^2}, \tag{2.14}$$

where w_a and w_b are the widths of the DC and RF electrodes, respectively, and $\omega_{sec,r}$ follows Eq. 2.9. Besides the trap characteristic parameters defined in Sec. 2.1.1, such as q, $\omega_{sec,r}$ and Φ_0, the ion equilibrium position y_0, known as the trap height is also needed to fully characterize a planar ion trap. Unlike the other quantities, y_0 is purely determined by the trap geometry. Nonetheless, by driving the central ground electrode with RF field with phase locked to the RF rail, y_0 can be slightly adjusted[Wes08, Cet11]. Instead of the the end caps, extra segmented DC electrodes are used to provide confinement in the axial direction (see Fig. 2.1-b). In such case, the axial secular frequency $\omega_{sec,a}$ is similar to that defined Eq. 2.11, but with the total changed to partial derivatives with z.

2.2 Qubit-motional state coupling

In trapped-ion QIS, many two qubit gates require ion entanglement facilitated through common-motion state phonons [CZ95, MS99], and some even require qubit initialized to the motional ground state [CZ95]. The manipulation of the ion motional state is not through direct mechanical perturbation, but rather using indirect, more precisely controlled qubit addressing via qubit-to-motional state coupling. Because of

the spatial field variation, the ion motion couples to its internal state transitions by perturbing the two-level qubit state Hamiltonian. In this section, we formulate the dynamics for trapped-ion qubit addressed by laser fields, and derive the Hamiltonian for the ion qubit-to-motional coupling.

We consider an ion with mass m, charge Q, and trapped in a harmonic potential with secular frequency ω_{sec} in either radial or axial direction. The ion internal state can be modeled as a two level system with the ground and excited state $|\downarrow\rangle$ and $|\uparrow\rangle$ separated by energy spacing $\hbar\omega_0$ ($\hbar \equiv h/(2\pi)$, h being the Planck constant). The quantization axis is defined by the field direction of the addressing laser field which is linearly polarized and follows

$$\mathbf{E} = \hat{z}E_0 \left(e^{i(kx-\omega t)} + h.c.\right)/2, \tag{2.15}$$

where E_0 and ω, are the laser field strength and frequency, respectively, and $k \equiv 2\pi/\lambda$ is the wave number (λ being field wavelength).

Without loss of generality, the full Hamiltonian for a two level system confined in a harmonic potential in a laser field follows

$$\begin{aligned} H &= H_{at} + H_{mot} + H_I, \\ &\equiv \hbar\omega_0\sigma_z + \hbar\omega_{sec}a^\dagger a + \frac{\hbar\Omega_R}{2}(\sigma^+ + \sigma^-)\left(e^{i(kx-\omega t)} + h.c.\right), \end{aligned} \tag{2.16}$$

where the internal, motional, and ion-laser interaction dynamics are described by $H_{at} \equiv \hbar\omega_0\sigma_z$, $H_{mot} \equiv \hbar\omega_{sec}a^\dagger a$, and $H_I \equiv \hbar\Omega_R(\sigma^+ + \sigma^-)\left(e^{i(kx-\omega t)} + h.c.\right)/2$, respectively. a and $a^\dagger$ are the annihilation and creation operators for the ion motional states $|n\rangle$. $\sigma_z \equiv |\uparrow\rangle\langle\uparrow| + |\downarrow\rangle\langle\downarrow|$, $\sigma_+ \equiv |\uparrow\rangle\langle\downarrow|$ and $\sigma_- \equiv |\downarrow\rangle\langle\uparrow|$ are the Pauli spin matrices, and $\Omega_R = QE_0|\langle\uparrow|z|\downarrow\rangle|/\hbar$ is the Rabi frequency.

With the quantized motion $x = \sigma_0(a^\dagger + a)$ (where $\sigma_0 = \sqrt{\hbar/(2m\omega_{sec})}$ being the motional ground state wave packet size in the harmonic potential), the interaction

Hamiltonian can be written as

$$H_I = \frac{\hbar\Omega_R}{2}(\sigma^+ + \sigma^-)\left(e^{i(\eta(a^\dagger+a)-\omega t)} + h.c.\right), \tag{2.17}$$

where we defined the Lamb Dicke parameter η as

$$\eta = 2\pi\sigma_0/\lambda. \tag{2.18}$$

With $\eta \ll 1$ (referred as the Lamb-Dcike regime), we can expand $e^{i\eta(a^\dagger+a)} = 1 + i\eta(a^\dagger + a)$, and H_I thus follow $H_I = H_c + H_r + H_b$, where

$$\begin{aligned} H_c &= \frac{\hbar\Omega_R}{2}(\sigma^+ + \sigma^-)e^{-i\omega t} + h.c., \\ H_r &= \eta\frac{\hbar\Omega_R}{2}(\sigma^+ a + \sigma^- a^\dagger)e^{-i\omega t} + h.c., \\ H_b &= \eta\frac{\hbar\Omega_R}{2}(\sigma^+ a^\dagger + \sigma^- a)e^{-i\omega t} + h.c.. \end{aligned} \tag{2.19}$$

The full Hamiltonian thus follows $H = H_{at} + H_{mot} + H_c + H_r + H_b$. When evaluating the time-dependent transition probability for H using rotating wave approximation (RWA) [CT92], the contributions from H_I all vanish[1] except H_c, H_r and H_b, for laser frequency close to $\omega = \omega_0$, $\omega = \omega_0 - \omega_{sec}$ and $\omega = \omega_0 + \omega_{sec}$, respectively. These three resonant transitions are referred as the carrier, red sideband, and blue sideband transitions of the qubit. H_r and H_b couple the internal state to the motional state transitions via the interaction terms $\sigma^+ a, \sigma^- a^\dagger, \sigma^+ a^\dagger \sigma^- a$, and the corresponding Rabi frequencies follow

$$\Omega_{n,n-1} = \frac{2}{\hbar}\langle n-1, \uparrow |H_r| \downarrow, n\rangle = \eta\sqrt{n}\Omega_R, \tag{2.20}$$

$$\Omega_{n,n+1} = \frac{2}{\hbar}\langle n+1, \uparrow |H_b| \downarrow, n\rangle = \eta\sqrt{n+1}\Omega_R. \tag{2.21}$$

The red sideband transitions can be used for sideband cooling, which uses the internal-motional coupling to remove phonon excitation with optical fields [WI79].

[1] Valid only when the qubit transition linewidth $\Gamma \ll \omega_{sec}$, known as the resolved sideband regime.

Part II

Atomic ion and optical cavity

Chapter 3

Theory of ion-photon interaction

In an atomic ion based quantum computer, the ability to manipulate ion-photon interaction is essential, as it facilitates all aspects of QIS, including control, gate operation, detection, and stationary-to-flying qubit conversion. For control, gate operation and detection, implementation of efficient ion-photon interface has demonstrated significant improvement towards scalable QIS (See for instance, Ref. [LLVC09, CSF+13, CBK+13], respectively). For conversion between stationary to flying qubit, research efforts still focus on the experiment realization of deterministic as well as probabilistic quantum network. In this thesis, we focus on the former, where deterministic state mapping between ions and photons is implemented in an optical cavity, in the frame work of cavity quantum electrodynamics (QED). This chapter focuses on the theoretical formalism of cavity QED and quantum network model, as well as an experimental design for a two-ion quantum memory implementation with $^{88}Sr^{+}$ ions. Sec. 3.1 and 3.2 review the formalism in literature. The work of a two-ion quantum node design in Sec. 3.3 and 3.4 is original.

3.1 Cavity QED

Cavity quantum electrodynamics, or cavity QED is the study of quantum dynamics of electromagnetic fields in cavity resonators. With the boundary confinement

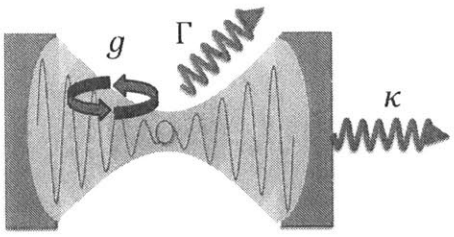

Figure 3-1: Schematic of a cavity QED system. A single ion is trapped at the mode waist of a cavity field, with which the internal transition is at resonance, at coupling strength g. The decoherence rate of the cavity and ion is denoted κ (See Appendix A for definition) and Γ, respectively.

imposed by the cavity, photons with well-defined modes act as single quantum excitation. Such excitation can couple to quantum systems with the same resonant frequencies, and exhibit interesting dynamics between a stationary and a flying quantum system [Kim98]. Cavity QED has been implemented in many physical systems, such as atoms with optical [Kim98] or microwave cavities[Har13], Josephson junctions [GDS09], and quantum dots [KRG+03]. For trapped-ion based quantum computers, realization of cavity QED is essential for the construction of a deterministic quantum network [CZKM97, Kim08]. We begin by briefly overviewing the theoretical formalism for cavity QED below.

3.1.1 Hamiltonian

A schematic depicting a typical model for cavity QED systems is shown in Fig. 3.1, where a two-level atom with energy spacing $\hbar\omega_A$ interacts with a photon excitation $\hbar\omega_C$ in a Fabry-Pérot cavity, via coupling strength g, which follows

$$g = \frac{d_e}{\hbar} E_C \equiv \frac{d_e}{\hbar}\sqrt{\frac{\hbar\omega_C}{2\epsilon_0 V}} = d_e\sqrt{\frac{\omega_C}{2\hbar\epsilon_0 V}} \tag{3.1}$$

where d_e is the dipole moment of the two-level atom, and E_C is the quantized electric field in the cavity. The mode volume occupied by the photon field is represented by V, and ϵ_0 is the vacuum electric permittivity.

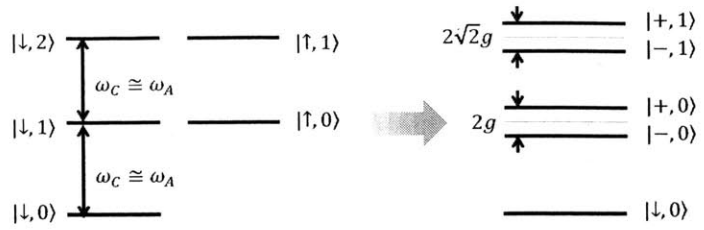

Figure 3-2: Level diagram of the coupled ion-photon system. On the left and right, are the level diagrams of a non-interacting, and resonant cavity ion system, respectively. For the latter, the frequencies satisfy $\omega_C \simeq \omega_A$. With coupling strength g, the degeneracy in each manifold is lifted by $2\sqrt{n}g$, resulting in a Rabi doublet.

The dynamics of the system is described by the Jaynes-Cummings model [JC63]

$$H = -\hbar\omega_A\sigma^\dagger\sigma - \hbar\omega_C c^\dagger c + \hbar g\left(c^\dagger\sigma + c\sigma^\dagger\right) \tag{3.2}$$

The three terms from left to right represent the dynamics of the atom, photon, and atom-photon interaction, respectively. The raising and lowering operators of the atom are given by $\sigma^\pm = |\uparrow\rangle\langle\downarrow|, |\downarrow\rangle\langle\uparrow|$, and the creation and annihilation operators of the photon excitation are represented by $c^\dagger$ and c, respectively.

Because of the interaction term $\hbar g\left(c^\dagger\sigma + c\sigma^\dagger\right)$ involves exchange of photon with atom excitation, the Jaynes-Cummings Hamiltonian can be decomposed to a set of vacuum Rabi doublets (See Fig. 3.1.1):

$$H = \begin{pmatrix} H_N & \cdots & \cdots & \cdots & 0 \\ \vdots & \ddots & & & \vdots \\ \vdots & & H_n & & \vdots \\ \vdots & & & \ddots & \vdots \\ 0 & \cdots & \cdots & \cdots & H_1 \end{pmatrix}, \tag{3.3}$$

where

$$\begin{aligned} H_n &= n\hbar\omega_C|\downarrow,n\rangle\langle\downarrow,n| + ((n-1)\hbar\omega_C + \hbar\omega_A)|\uparrow,n-1\rangle\langle\uparrow,n-1| \\ &+ \hbar\sqrt{n}g\left(|\uparrow,n-1\rangle\langle\downarrow,n| + |\downarrow,n\rangle\langle\uparrow,n-1|\right). \end{aligned} \tag{3.4}$$

The eigenstates for each vacuum Rabi doublet take the form

$$|\pm, n\rangle = \mp\frac{1}{\sqrt{2}}\sqrt{1 \pm \frac{\delta_{CA}^2}{\sqrt{\delta_{CA}^2 + 4ng^2}}}|\downarrow, n\rangle - \frac{1}{\sqrt{2}}\sqrt{1 \mp \frac{\delta_{CA}^2}{\sqrt{\delta_{CA}^2 + 4ng^2}}}|\uparrow, n-1\rangle, \quad (3.5)$$

with energy splitting

$$E_{\pm,n} = \hbar\left(n\omega_C - \frac{\delta_{CA}}{2}\right) \pm \frac{\hbar}{2}\sqrt{\delta_{CA}^2 + 4ng^2}, \quad (3.6)$$

where $\delta_{CA} = \omega_C - \omega_A$ is the cavity-to-atom detuning, and the Rabi frequency between the two eigenstates follows $\Omega_R = (E_{+,n} - E_{-,n})/\hbar = \sqrt{\delta_{CA}^2 + 4ng^2}$. In the near-resonance limit with $\delta_{CA} \ll g$,

$$|+, n\rangle \simeq |\downarrow, n\rangle, \quad |-, n\rangle \simeq |\uparrow, n-1\rangle, \quad \Omega_R \simeq 2\sqrt{n}g. \quad (3.7)$$

3.1.2 Effect of decoherence and optical Bloch equation

The Janynes-Cummings Hamiltonian in Eq. 3.2 describes the dynamics of a closed system formed by the atom and photon excitation, where density matrix $\rho(t)$ evolves as

$$\frac{\partial\rho}{\partial t} = -\frac{i}{\hbar}[H, \rho]. \quad (3.8)$$

The system can couple to the environment via two mechanisms of decoherence, namely atomic spontaneous emission and cavity decay, which are generally measured by Γ and κ, respectively. While the expression for κ is derived in Appendix A (See Eq. A.9), Γ follows

$$\Gamma = \frac{d_e^2\omega_A^3}{3\pi\epsilon_0\hbar c^3}, \quad (3.9)$$

where d_e is the dipole moment between the atomic state $|\downarrow\rangle$ and $|\uparrow\rangle$, and c is the speed of light in vacuum. To include the decoherence mechanisms, Eq. 3.8 is modified

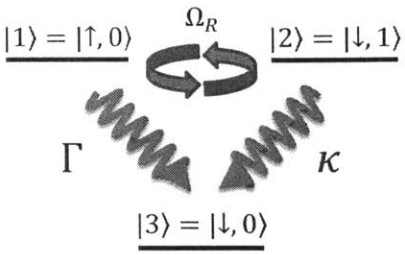

Figure 3-3: Level diagram involved in Purcell effect modeling using optical Bloch equation. A single photon excitation is involved in a cavity QED system. State $|1\rangle = |\uparrow, 0\rangle$ and $|2\rangle = |\downarrow, 1\rangle$ are coupled via a Rabi frequency Ω_R, and both decay to $|3\rangle = |\downarrow, 0\rangle$ at rate Γ and κ, respectively.

with the Lindblad terms $L_\alpha(\rho)$, and becomes the optical Bloch equation (OBE):

$$\begin{aligned} \frac{\partial \rho}{\partial t} &= -\frac{i}{\hbar}[H, \rho] + \Sigma_\alpha L_\alpha(\rho) \\ &\equiv -\frac{i}{\hbar}[H, \rho] + \Sigma_\alpha \left(L_\alpha \rho L_\alpha^\dagger - \frac{1}{2}(\rho L_\alpha^\dagger L_\alpha + L_\alpha^\dagger L_\alpha \rho) \right), \end{aligned} \tag{3.10}$$

where the loss L_α are given by

$$L_\alpha = \{\sqrt{\Gamma}\sigma^-, \sqrt{\kappa}c\}, \tag{3.11}$$

and the Lindblad super-operator is defined as $L_\alpha(\rho) \equiv L_\alpha \rho L_\alpha^\dagger - \frac{1}{2}(\rho L_\alpha^\dagger L_\alpha + L_\alpha^\dagger L_\alpha \rho)$.

One important aspect in cavity QED is the cavity field modification to the atomic emission spectrum, which can be obtained by solving the OBE for the triplet system, spanned by the states

$$|1\rangle = |\uparrow, 0\rangle, \quad |2\rangle = |\downarrow, 1\rangle, \quad |3\rangle = |\downarrow, 0\rangle. \tag{3.12}$$

In the near-resonance limit, $|1\rangle$ and $|2\rangle$ oscillates with $\Omega_R \simeq 2g$. With the the system initially in state $|1\rangle$, and in the limit $\Gamma \ll g \ll \kappa$, the excited state population of the atom, represented by the matrix element ρ_{11} of the density matrix, follows

$$\rho_{11} \simeq -\frac{4g^2}{\kappa}\rho_{11}. \tag{3.13}$$

Compared to spontaneous decay, the atom decays with a new rate $\Gamma_c = 4g^2/\kappa$. The ratio between Γ_c and the spontaneous decay rate Γ is the referred as the Purcell factor, or cooperativity of the cavity η_C, with

$$\eta_C = \frac{4g^2}{\kappa\Gamma}. \tag{3.14}$$

As an important figure of merit of a cavity QED system, the cooperativity η_C measures the ratio of the scattered photon number from the atom into the cavity and that into the free space[1]. In QIS, as we can see in the following sections (see also Ref. [DP04, GALS07]), a quantum interconnect based on cavity QED requires $\eta_C \gg 1$, which is referred as the strong coupling regime.

Another two important forms of η_C are

$$\eta_C = \frac{3}{4\pi^2}\frac{\lambda_C^3}{V}Q, \quad Q = \frac{\omega_C}{\kappa}, \tag{3.15}$$

$$= \frac{24\mathcal{F}}{\pi k_0^2 w_0^2} \tag{3.16}$$

where the first expression is obtained using Eq. 3.1,3.9, and $\lambda_C = 2\pi c/\omega_C$. This is the first expression derived by E. M. Purcell, and shows that η_C is independent of the properties of the atom. The second expression is obtained based on the first, using $\kappa = c\pi/(L\mathcal{F})$ from Eq. A.9, where $\mathcal{F}$ is the cavity finesse, and $V = \pi w_0^2 L/4$ for a Gaussian laser mode (L is the cavity length) [Cet11]. It shows further that the dependence of η_C on the cavity is only on the finesse $\mathcal{F}$ and the waist size w_0, but not the cavity length L.

3.2 Quantum Network

One important application of cavity QED systems is the quantum interconnect in the deterministic quantum network [CZKM97], the schematic of which is depicted in Fig. 3.2 (for single ion case). Two quantum nodes are connected by a photonic

[1] See also Chapter 4 of [Lei09]

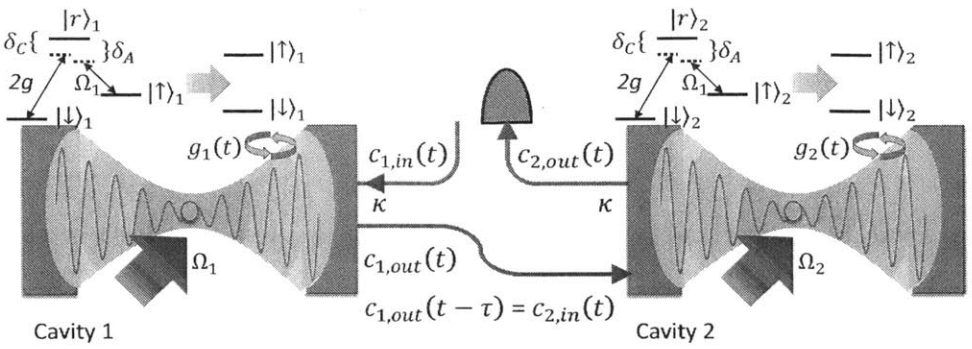

Figure 3-4: Schematic of a deterministic quantum network for single ions. The two nodes in the network consist of trapped ions, which couple to a flying qubit via a coherent mapping to photons in optical cavities as the quantum interconnects. Photons bearing the state from ions in cavity 1, transmit through the photonic channel between the two nodes (represented by the field operator $c_{1,out}(t)$ and $c_{2,in}(t)$), and are mapped to the state of the ion in cavity 2. To maximize the coupling fidelity, the coupling strength $g_{1,2}(t)$ needs to follow a particular time dependent pattern. This is facilitated by coupling the ion state $|\downarrow\rangle_{1,2}$ and $|\uparrow\rangle_{1,2}$ using a Raman scheme via a state $|r\rangle_{1,2}$, which gives a tunable effective coupling strength $g_{1,2}(t)$ to the cavity field.

channel (e.g. an optical fiber), through which a photon as the flying qubit transmits with negligible loss. Trapped ions, as stationary qubits in the cavity, are coupled to photons via cavity QED. The goal, is to map the ion state in cavity 1 to a photon sate, and then reversely to the ion state in cavity 2. To maximize the fidelity, one needs to be able to control the ion-photon interaction strength $g(t)$ in each cavity, which can be facilitated through a Raman process in a three-level Λ configuration. We begin by reviewing the formalism in Ref. [CZKM97] for a single ion case in each cavity, and then move to the formalism for multiple ions.

With a single ion in each cavity (Fig. 3.2), the goal is to realize the mapping

$$(\alpha|\downarrow\rangle_1 + \beta|\uparrow\rangle_1)|0\rangle \otimes |\downarrow\rangle_2|0\rangle_2 \rightarrow |\downarrow\rangle_1|0\rangle_1 \otimes (\alpha|\downarrow\rangle_2 + \beta|\uparrow\rangle_2)|0\rangle, \tag{3.17}$$

where from left to right, the quantum state represents the atomic and photon number excitation, in cavity 1 and 2, respectively. To precisely reverse the ion-to-photon state mapping, the cavity resonance is not matched directly with the energy spacing between $|\downarrow\rangle$ and $|\uparrow\rangle$, but close to the transition to the third level $|r\rangle$. The interaction between $|\downarrow\rangle$ and $|\uparrow\rangle$ is then facilitated through a Raman transi-

tion [PGCZ95, MMK+95, LE96, MBR+04], with the $|\uparrow\rangle \rightarrow |r\rangle$ transition controlled by an addressing laser. The effective cavity interaction strength with the two level system $\uparrow, \downarrow$ is then a function of Ω, which can be varied by tuning the laser intensity.

3.2.1 Hamiltonian

The Hamiltonian H_i $(i = 1, 2)$ of the Λ system in the cavity i, with the $|r\rangle$-to-$|\downarrow\rangle$ spacing $\hbar\omega_A$, cavity photon energy $\hbar\omega_C$, and Raman laser phase $\omega_L t + \phi_i(t)$ follows

$$H_i = \hbar\omega_C c_i^\dagger c_i + \hbar\omega_A \sigma_i^+ \sigma_i^- + \hbar g(\sigma_i^+ c_i + \sigma_i^- c_i^\dagger) + \frac{\hbar}{2}\Omega_i(t)\left[e^{-i[\omega_L t + \phi_i(t)]}|r\rangle_i\langle\uparrow| + h.c.\right], \tag{3.18}$$

where c_i is the photon field annihilation operator, and $\sigma_i^\pm$ is the raising and lowering operator of the $|\downarrow\rangle_i \rightarrow |r\rangle_i$ transition. The coupling strength and Rabi frequency between the cavity photon and $|\downarrow\rangle_i \rightarrow |r\rangle_i$ transition, and between the laser and $|\uparrow\rangle_i \rightarrow |r\rangle_i$ are represented by g and $\Omega_i(t)$, respectively.

In order to suppress spontaneous Raman scattering, the laser is is assumed to be far-detuned from the atomic transition, i.e. $|\delta_A| \gg \Omega_{1,2}(t), g$, with $\delta_A \equiv \omega_L - \omega_A$. In such case, the state $|r\rangle$ can be eliminated from Eq. 3.18, resulting in a Jaynes-Cummings-like Hamiltonian in the co-rotating frame of the laser [MBR+04]

$$H_i = -\hbar\delta_C c_i^\dagger c_i + \hbar\frac{g^2}{\delta_A} c_i^\dagger c_i |\downarrow\rangle_i\langle\downarrow| + \hbar\delta\omega_i(t)|\uparrow\rangle_i\langle\uparrow| - i\hbar g_i(t)\left[e^{i\phi_i(t)}\sigma_i^+ c_i + h.c.\right]. \tag{3.19}$$

where

$$\delta\omega_i(t) \equiv \frac{\Omega_i^2(t)}{4\delta_A}, \quad g_i(t) \equiv \frac{g\Omega_i(t)}{2\delta_A}. \tag{3.20}$$

Equation 3.19 suggests a method of coherent mapping between an effective two level atom ($|\downarrow\rangle$, $|\uparrow\rangle$) and photon excitation, with a tunable coupling strength $g_i(t)$.

3.2.2 Network photon and quantum Langevin equation

The network photons, as represented by the field operators $c_{1,out}(t)$ and $c_{2,in}(t)$ can be modeled as loss with respect to the cavity QED system 1 and 2. We have already

shown that a system with loss can be modeled by adding the Lindblad terms to OBE (see Eq. 3.1.2), which modifies the dynamics of the quantum system. Here to model the dynamics of the loss itself, it is convenient to introduce the quantum Langevin equation, where in the Heisenberg picture, the cavity annihilation operator evolves as [Ste13]

$$\begin{aligned} \frac{dc_i}{dt} &= -\frac{i}{\hbar}[c_i, H_i] - \frac{\kappa}{2}c_i - \sqrt{\kappa}c_{i,in}(t), \\ c_{i,out}(t) &= c_{i,in}(t) + \sqrt{\kappa}c_i(t). \end{aligned} \tag{3.21}$$

We assume negligible loss in the quantum channel, so the input excitation $c_{2,in}(t) = c_{1,out}(t-\tau)$, where τ is the time delay for photon transmission along the quantum channel. Equation 3.21 thus becomes, for cavity 2 in particular,

$$\frac{dc_2}{dt} = -\frac{i}{\hbar}[c_2, H_2] - \frac{\kappa}{2}c_2 - \kappa c_1(t-\tau) - \sqrt{\kappa}c_{1,in}(t-\tau). \tag{3.22}$$

We can simplify the above equations by transforming operators in the first cavity into the time-delayed operators, namely,

$$c_1(t-\tau) \to c_1(t), \quad c_{1,in}(t-\tau) \to c_{1,in}(t), \quad g_1(t-\tau) \to g_1(t), \quad \phi_1(t-\tau) \to \phi(t).$$

The quantum Langevin equations for both cavity thus reduce to

$$\frac{dc_1}{dt} = -\frac{i}{\hbar}[c_1, H_1] - \frac{\kappa}{2}c_1 - \sqrt{\kappa}c_{1,in}(t), \tag{3.23}$$

$$\frac{dc_2}{dt} = -\frac{i}{\hbar}[c_2, H_2] - \frac{\kappa}{2}c_2 - \kappa c_1(t) - \sqrt{\kappa}c_{1,in}(t). \tag{3.24}$$

3.2.3 Approach to determine $g(t)$ for deterministic quantum mapping

We recall that the goal is to choose a correct waveform of $g_{1,2}(t)$, in order to maximize the fidelity of quantum state mapping in Eq. 3.17. Here we outline the approach used in Ref. [CZKM97], but choose not to go into the detailed solution for $g_{1,2}(t)$. Rather,

we discuss in brief in the next section, the experimental requirement for an ion-cavity system to implement this scheme, which leads to our experiment described in Chapter 4.

To determine the waveform of $g_{1,2}(t)$, it is equivalent to solve for $g_{1,2}(t)$ and a system wave function $\Psi(t)$, according to the following effective Hamiltonian H_{eff} [CZKM97], in the language of quantum trajectories.

$$H_{eff} = H_1 + H_2 - i\hbar\frac{\kappa}{2}\left(c_1^\dagger c_1 + c_2^\dagger c_2 + 2c_2^\dagger c_1\right), \tag{3.25}$$

which describe the system dynamics when no photons are detected through the output of cavity 2. According to Eq. 3.21, the output $c_{2,out}(t)$ follows

$$c_{2,out}(t) = c_{1,in}(t) + \sqrt{\kappa}(c_1(t) + c_2(t)). \tag{3.26}$$

We further impose that the system is in absence of any driving field. That is, together with Eq. 3.26

$$c_{1,in}(t)|\Psi(t)\rangle = 0, \tag{3.27}$$

$$(c_1(t) + c_2(t))|\Psi(t)\rangle = 0. \tag{3.28}$$

Two additional conditions in Ref. [CZKM97] are imposed, so that $g_{1,2}(t)$ can be completely determined. That is

$$g_2(t) = g_1(-t), \quad \text{time-reversal symmetry}, \tag{3.29}$$

$$g_1(t > 0) = \text{const.}. \tag{3.30}$$

We here skip the solution part, and proceed to the analysis of experimental requirement for the scheme implementation, and the generalization of the scheme to a two-ion case.

3.2.4 Requirement for implementation

Several loss mechanisms in this scheme are also considered in Ref. [CZKM97], which need to be minimized in order to achieve high fidelity performance.

First, decoherence is neglected in the ion-cavity Hamiltonian (Eq. 3.18 and 3.19). The auxiliary state $|r\rangle$ decays to state $|\downarrow\rangle$ and $|\uparrow\rangle$ via spontaneous rate $\Gamma_\downarrow$ and $\Gamma_\uparrow$, respectively. Because the probability of the ion in the state $|r\rangle$ scales as $p_r \sim (\Omega_{1,2}^2/4 + 4g_{1,2}^2)/\delta_A$, and the total decoherence rate scales as $p_r(\Gamma_\downarrow + \Gamma_\uparrow)$, it thus requires

$$\frac{\Omega_{1,2}^2 + 4g_{1,2}^2}{4\delta_A^2} \ll \kappa, \frac{g_{1,2}\Omega_{1,2}}{2\delta_A}. \tag{3.31}$$

When $\kappa \sim g_{1,2}\Omega_{1,2}/\delta_A$, the above inequality reduces to the condition for strong coupling (see Eq. 3.14)

$$\frac{4g_{1,2}^2}{\kappa(\Gamma_\downarrow + \Gamma_\uparrow)} \gg 1. \tag{3.32}$$

A second source of decoherence is due to the control field. In particular, it consists of the Raman and qubit laser frequency instability, cavity mechanical instability, and magnetic field noise, which are measured by the laser linewidth γ_Ω, γ_L, cavity lock linewidth γ_{cav}, and B-field noise level $\mu_B B_{rms}$, respectively ($\mu_B \equiv$ Bohr magneton). They should also satisfy

$$\gamma_\Omega + \gamma_L + \gamma_{cav} + \mu_B B_{rms}/\hbar \ll \kappa, \frac{g_{1,2}\Omega_{1,2}}{2\delta_A}. \tag{3.33}$$

Finally, to maximize the directionality of the photon transmission, the cavity should be designed asymmetric; to minimize the scattering and absorption photon loss, the cavity should be in the transmission dominant limit. That is

$$\mathcal{T}_{1,2}, \mathcal{T}_{2,1} \gg \mathcal{T}_{1,env}, \mathcal{T}_{2,env}, \mathcal{L}_{1,2}, \tag{3.34}$$

where $\mathcal{T}_{1,2}$ an $\mathcal{T}_{2,1}$ are mirror transmission of cavity 1 and 2 towards cavity 2 and 1, respectively, whereas $\mathcal{T}_{1,env}$ and $\mathcal{T}_{2,env}$ are those towards the environment thermal bath. $\mathcal{L}_{1,2}$ denotes the scattering and absorption loss in cavity 1 and 2, respectively.

3.3 Two ion quantum node

A typical ion trap implementation of quantum computer consists of multiple ions interacting via Coulomb fields [KMW02]. To realize a quantum network based on the deterministic model in Ref. [CZKM97], it is desired to have a protocol to map a multiple qubit state to photon states. However, with the maximum number of excitation n, the number of quantum states scales as 2^n and $n+1$ for an n-ion and n-photon system, respectively. A photon number state is therefore not a good quantum number for communication in the framework of deterministic multi-ion quantum network. Nonetheless, a multiple ion system can still be useful, for two reasons. First, instead of a single ion, an n-ion crystal can provide an enhancement of ion-cavity coupling strength of $\sqrt{n}$, which can be used as a transducer for strong coupling between a single ion and a single photon [LLC+11, Lei09]. Secondly, because the the information space for an n-ion system is larger than that of an n-photon system, the former can be used for photon quantum storage [GZ04, DP04, GALS07, LST09]. Furthermore, because of the individual addressability in an n-ion system, a photonic gate can be implemented for the incoming photons. In this section, we generalize the scheme in Sec. 3.2 to a 2-ion 2-photon case, and demonstrate an approach for converting a photon number state to ion state for quantum memory and photonic gate. The goal is to map an arbitrary photon number state to that of two ions, i.e.

$$\begin{aligned} & |\downarrow_1\downarrow_2\rangle(\alpha_0|0\rangle_L + \alpha_1|1\rangle_L + \alpha_2|2\rangle_L)|0\rangle_{ph} \\ \rightarrow \quad & \left(\alpha_0|\downarrow_1\downarrow_2\rangle + \alpha_1|\tilde{\uparrow}\rangle + \alpha_2|\uparrow_1\uparrow_2\rangle\right)|0\rangle_L|0\rangle_{ph}, \end{aligned} \tag{3.35}$$

where we have indexed the photon number quantum state with subscript L, and introduced the phonon number state $|n\rangle_{ph}$ and collective two-ion excited state $|\tilde{\uparrow}\rangle \equiv (|\downarrow_1\uparrow_2\rangle + |\uparrow_1\downarrow_2\rangle)/\sqrt{2}$. These two states are essential to realize the mapping in Eq. 3.35. For the former, because the ion-photon Hamiltonian only connects the two states within the same Rabi doublets (See Sec. 3.1.1), another quantum register is needed in addition to the ion and photon states, to facilitate the mapping $|2\rangle_L \rightarrow$

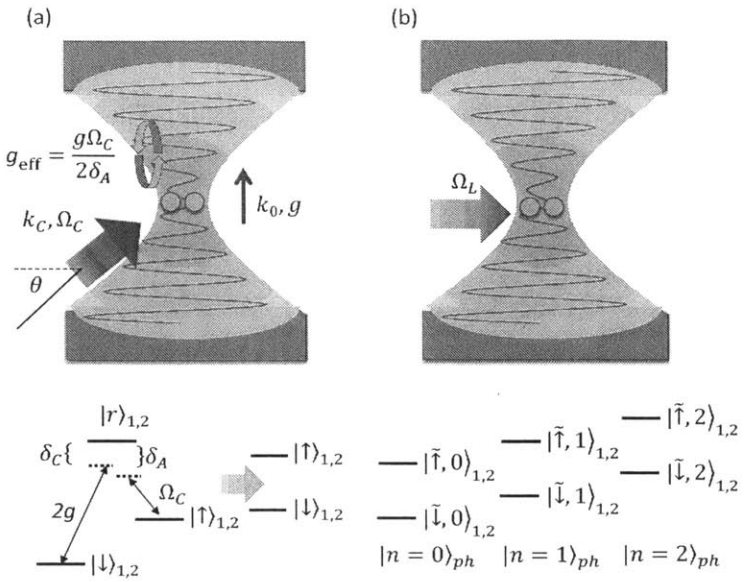

Figure 3-5: Schematic showing the cavity QED system with two ions, as the quantum interconnect for a two-ion node. (a) two ions are trapped in symmetry with respect to the cavity field spatial profile, which are indistinguishable to the field. A Raman scheme is employed so that a tunable cavity-ion interaction can be realized as in Sec. 3.2. The wave vector for the cavity and Raman beam is labeled k_0 and k_C, respectively. The angle between k_C and the ion chain axis is labeled θ. (b) with a laser directly addressing the $|\downarrow\rangle_{1,2} \rightarrow |\uparrow\rangle_{1,2}$ transition, phonon excitation $|n\rangle_{ph}$ in the ion's motional state can couple to the two ion collective state via sideband transitions. The carrier transition Rabi frequency is labeled Ω_L

$|\uparrow_1\uparrow_2\rangle$. For the latter as we will show immediately in the following, because a cavity field addresses both ions simultaneously, it is the collective excitation state that interacts with the photons in the cavity-ion Hamiltonian.

We illustrate the procedure for Eq. 3.35 in the following in detail. In order to be precise about the collective state, we first setup the formalism below.

3.3.1 Mapping between single photon to collective two ion states

We consider that two ions are indistinguishable with respect to the cavity field. That is, the trapping configuration allows the cavity field experienced by the two ions to be always equal. One way to realize this configuration is shown in the schematic in Fig.3.3-a, where the two-ion chain are trapped orthogonal to the cavity axis, with the

midpoint overlapped with that of the field Gaussian profile. The same Λ-structure of ion internal structure is used to enable a tunable cavity-ion interaction strength

$$g_{\text{eff}} = \frac{g\Omega_C}{2\delta_A}, \tag{3.36}$$

where we denote the Rabi frequency of the $|\uparrow\rangle_{1,2} \rightarrow |r\rangle_{1,2}$ transition Ω_C, to be distinguished from Ω_L, the Rabi frequency for directly addressed transition between $|\downarrow\rangle$ and $|\uparrow\rangle$, introduced later in this section. We use the same notation as the single ion model in Sec. 3.2, except that the index {1,2} now refers to the two ions. Because the two ions are indistinguishable, their Rabi frequencies Ω_C, Ω_L, and cavity coupling strength g, g_{eff} are identical.

The interaction Hamiltonian of the cavity QED system H_I^C is the sum of that of either ion interacting with the cavity field:

$$\begin{aligned} H_I^C &= H_{I1}^C + H_{I2}^C \\ &\equiv \hbar g_{\text{eff}} \left(|\uparrow_1\downarrow_2\rangle\langle\downarrow_1\downarrow_2| c + |\downarrow_1\downarrow_2\rangle\langle\uparrow_1\downarrow_2| c^\dagger \right) \\ &+ \hbar g_{\text{eff}} \left(|\downarrow_1\uparrow_2\rangle\langle\downarrow_1\downarrow_2| c + |\downarrow_1\downarrow_2\rangle\langle\downarrow_1\uparrow_2| c^\dagger \right). \end{aligned} \tag{3.37}$$

By defining the two ion collective state $|\tilde{\downarrow}_C\rangle$ and $|\tilde{\uparrow}_C\rangle$, and collective coupling strength $\tilde{g}_C$ as

$$|\tilde{\downarrow}_C\rangle \equiv |\downarrow_1\downarrow_2\rangle, \quad |\tilde{\uparrow}_C\rangle \equiv \frac{1}{\sqrt{2}} \left(|\downarrow_1\uparrow_2\rangle + |\uparrow_1\downarrow_2\rangle \right), \quad \tilde{g}_C \equiv \sqrt{2} g_{\text{eff}}, \tag{3.38}$$

the interaction Hamiltonian H_I can be reduced to

$$H_I^C = \hbar\tilde{g}_C \left(|\tilde{\uparrow}_C\rangle\langle\tilde{\downarrow}_C| c + |\tilde{\downarrow}_C\rangle\langle\tilde{\uparrow}_C| c^\dagger \right). \tag{3.39}$$

3.3.2 Mapping between single ion to collective two ion states

The schematic showing coupling between the ion collective state to phonon excitation is presented in Fig. 3.3-b, where a laser beam addressing the direct $|\downarrow\rangle_{1,2} \rightarrow |\uparrow\rangle_{1,2}$

transition incidents on both ions, with Rabi frequency Ω_L along the ion-chain axis. To ensure the ions are addressed indistinguishably, the laser waist is set to the midpoint of the ion chain.

We aim to establish a mapping between the collective ion state and the collective motional state of the ion via sideband transitions. For a single ion Lamb Dicke parameter η, the effective Lamb Dicke parameter for an N-ion linear crystal follows $\eta_N = \eta/\sqrt{N}$ [KKC+12]. Therefore the Hamiltonian for the system can be written as

$$\begin{aligned} H_I^L &= H_{I1}^L + H_{I2}^L \\ &\equiv \hbar\frac{\eta\Omega_L}{2\sqrt{2}}\left(|\uparrow_1\downarrow_2\rangle\langle\downarrow_1\downarrow_2|a + |\downarrow_1\downarrow_2\rangle\langle\uparrow_1\downarrow_2|a^\dagger\right) \\ &+ \hbar\frac{\eta\Omega_L}{2\sqrt{2}}\left(|\downarrow_1\uparrow_2\rangle\langle\downarrow_1\downarrow_2|a + |\downarrow_1\downarrow_2\rangle\langle\downarrow_1\uparrow_2|a^\dagger\right), \end{aligned} \tag{3.40}$$

where a represents the annihilation operator of the motional phonon.

Similar to the collective ion state defined for H_I^C, we can reduce H_I^L to

$$H_I^L = \hbar\eta\frac{\tilde{\Omega}_L}{2}\left(|\tilde{\uparrow}_L\rangle\langle\tilde{\downarrow}_L|a + |\tilde{\downarrow}_L\rangle\langle\tilde{\uparrow}_L|a^\dagger\right), \tag{3.41}$$

where the collective ion state $|\tilde{\downarrow}_L\rangle$ and $|\tilde{\uparrow}_L\rangle$, and Rabi frequency $\tilde{\Omega}_L$ are

$$|\tilde{\downarrow}_L\rangle \equiv |\downarrow_1\downarrow_2\rangle, \quad |\tilde{\uparrow}_L\rangle \equiv \frac{1}{\sqrt{2}}\left(|\downarrow_1\uparrow_2\rangle + |\uparrow_1\downarrow_2\rangle\right), \quad \tilde{\Omega}_L \equiv \Omega. \tag{3.42}$$

Not surprisingly, we have the two collective ion state equal:

$$|\tilde{\downarrow}\rangle \equiv |\tilde{\downarrow}_C\rangle = |\tilde{\downarrow}_L\rangle, \quad |\tilde{\uparrow}\rangle \equiv |\tilde{\uparrow}_C\rangle = |\tilde{\uparrow}_L\rangle, \tag{3.43}$$

which can be used to facilitate the coupling to both photon and phonon states.

3.3.3 Pulse sequence

With the same collective ion state coupled to phonon and photon states, we can use it to perform the mapping between the phonon number and photon number states.

In particular, to realize Eq. 3.35, the following pulse sequences are employed:

1. π-pulse between $|\tilde{\downarrow}\rangle|2\rangle_L$ and $|\tilde{\uparrow}\rangle|1\rangle_L$:

   Beginning with an arbitrary two-photon state and no phonon or ion excitation, we apply a π-pulse between the photon number and the collective ion state in the two-photon manifold, resulting in

   $$\begin{aligned} & |\tilde{\downarrow}\rangle(\alpha_0|0\rangle_L + \alpha_1|1\rangle_L + \alpha_2|2\rangle_L)|0\rangle_{ph} \\ \rightarrow \quad & \alpha_0|\tilde{\downarrow}\rangle|0\rangle_L|0\rangle_{ph} + \alpha_1\left(\beta_1|\tilde{\downarrow}\rangle|1\rangle_L + \beta_2|\tilde{\uparrow}\rangle|0\rangle_L\right)|0\rangle_{ph} - i\alpha_2|\tilde{\uparrow}\rangle|1\rangle_L|0\rangle_{ph}, \end{aligned} \tag{3.44}$$

   where due to the Rabi frequency difference between the $\left(|\tilde{\downarrow}\rangle|2\rangle_L, |\tilde{\uparrow}\rangle|1\rangle_L\right)$ and $\left(|\tilde{\downarrow}\rangle|1\rangle_L, |\tilde{\uparrow}\rangle|0\rangle_L\right)$ manifolds, the π-pulse on the former results in the rotation $|\tilde{\downarrow}\rangle|1\rangle_L \rightarrow \beta_1|\tilde{\downarrow}\rangle|1\rangle_L + \beta_2|\tilde{\uparrow}\rangle|0\rangle_L$ in the latter, with

   $$\beta_1 = \cos(\sqrt{2}\pi/2), \quad \beta_2 = -i\sin(\sqrt{2}\pi/2). \tag{3.45}$$

   We will show in step 3 and 4 that this extra phase can be removed by applying a $3\pi/2$ between $|\tilde{\downarrow}\rangle|1\rangle_L$ and $|\tilde{\uparrow}\rangle|1\rangle_L$, followed by a phonon-to-collective-state mapping.

2. Red sideband π-pulse between $|\tilde{\uparrow}\rangle|0\rangle_{ph}$ and $|\tilde{\downarrow}\rangle|1\rangle_{ph}$:

   To further map the photon number excitation to that of the ions, we should now push the excitation created in step 1 to the phonon register, i.e. to apply a red sideband on the collective ion excitation state, resulting in

   $$\alpha_0|\tilde{\downarrow}\rangle|0\rangle_L|0\rangle_{ph} + \alpha_1\left(\beta_1|\tilde{\downarrow}\rangle|1\rangle_L\rangle|0\rangle_{ph} - i\beta_2|\tilde{\downarrow}\rangle|0\rangle_L|1\rangle_{ph}\right) - \alpha_2|\tilde{\downarrow}\rangle|1\rangle_L|1\rangle_{ph}. \tag{3.46}$$

3. $3\pi/2$-pulse between $|\tilde{\downarrow}\rangle|1\rangle_L$ and $|\tilde{\uparrow}\rangle|0\rangle_L$:

   With the ion register emptied to that of the phonon, we can now again, map the photon excitation to the ion. This time, a $3\pi/2$-pulse is used to create an

anti-symmetry between $\beta_1|\tilde{\downarrow}|1\rangle_L$ and $\beta_2|\tilde{\uparrow}|0\rangle_L$, resulting in

$$\alpha_0|\tilde{\downarrow}\rangle|0\rangle_L|0\rangle_{ph} + i\alpha_1\left(\beta_1|\tilde{\uparrow}\rangle|0\rangle_{ph} - \beta_2|\tilde{\downarrow}\rangle|1\rangle_{ph}\right)|0\rangle_L - i\alpha_2|\tilde{\uparrow}\rangle|0\rangle_L|1\rangle_{ph}. \quad (3.47)$$

4. Red sideband π-pulse between $|\tilde{\uparrow}\rangle|1\rangle_{ph}$ and $|\tilde{\downarrow}\rangle|2\rangle_{ph}$:

With a red sideband applied to the collective ion state on the $\left(|\tilde{\uparrow}\rangle|1\rangle_{ph}, |\tilde{\downarrow}\rangle|2\rangle_{ph}\right)$ manifold, the two-photon excitation is now completely transferred to that of the phonons, i.e.

$$-i\alpha_2|\tilde{\uparrow}\rangle|0\rangle_L|1\rangle_{ph} \rightarrow -\alpha_2|\tilde{\downarrow}\rangle|0\rangle_L|2\rangle_{ph}, \quad (3.48)$$

and terms in the bracket in Eq. 3.47 becomes

$$\begin{aligned} & \beta_1\left(-i\beta_1|\tilde{\uparrow}\rangle|0\rangle_{ph} - \cancel{i\beta_2|\tilde{\downarrow}\rangle|0\rangle_{ph}}\right) - \beta_2\left(-\cancel{i\beta_1|\tilde{\downarrow}\rangle|1\rangle_{ph}} - i\beta_2|\tilde{\uparrow}\rangle|0\rangle_{ph}\right) \\ = \quad & -i\left(\beta_1^2 - \beta_2^2\right)|\tilde{\uparrow}\rangle|0\rangle_{ph} = -i|\tilde{\uparrow}\rangle|0\rangle_{ph}. \end{aligned} \quad (3.49)$$

The whole expression thus becomes

$$\alpha_0|\tilde{\downarrow}\rangle|0\rangle_L|0\rangle_{ph} + \alpha_1|\tilde{\uparrow}\rangle\rangle|0\rangle_L|0\rangle_{ph} - \alpha_2|\tilde{\downarrow}\rangle|0\rangle_L|2\rangle_{ph}. \quad (3.50)$$

5. π-pulse between $|\tilde{\downarrow}\rangle|1\rangle_L$ and $|\tilde{\uparrow}\rangle|0\rangle_L$:

We have successfully removed the undesired phase $\beta_{1,2}$, taking the advantage that the Rabi frequency ratio between manifold $\left(|\tilde{\uparrow}\rangle|1\rangle_{ph}, |\tilde{\downarrow}\rangle|2\rangle_{ph}\right)$ and $\left(|\tilde{\uparrow}\rangle|0\rangle_{ph}, |\tilde{\downarrow}\rangle|1\rangle_{ph}\right)$ is the same as between $\left(|\tilde{\downarrow}\rangle|2\rangle_L, |\tilde{\uparrow}\rangle|1\rangle_L\right)$ and $\left(|\tilde{\downarrow}\rangle|1\rangle_L, |\tilde{\uparrow}\rangle|0\rangle_L\right)$. At this stage, we have converted the two-photon excitation to that of phonons. To convert it to pure ion excitation, while trying to avoid any additional undesired phase, we'd like to hide the middle term in previous result from the effect of red sideband π-pulses, by converting the excitation to photon. That is, by applying a π-pulse between $|\tilde{\downarrow}\rangle|1\rangle_L$ and $|\tilde{\uparrow}\rangle|0\rangle_L$, we have

$$\alpha_0|\tilde{\downarrow}\rangle|0\rangle_L|0\rangle_{ph} - i\alpha_1|\tilde{\downarrow}\rangle\rangle|1\rangle_L|0\rangle_{ph} - \alpha_2|\tilde{\downarrow}\rangle|0\rangle_L|2\rangle_{ph}. \quad (3.51)$$

6. Red sideband π-pulse between $|\tilde{\downarrow}\rangle|2\rangle_{ph}$ and $|\tilde{\uparrow}\rangle|1\rangle_{ph}$, and between $|\tilde{\downarrow}\rangle|1\rangle_{ph}$ and $|\tilde{\uparrow}\rangle|0\rangle_{ph}$:

   To completely transfer the phonon excitation to the ions, we perform two consecutive red sideband π-pulses on the two individual ions 1 and 2, in the manifold $\left(|\tilde{\downarrow}\rangle|2\rangle_{ph}, |\tilde{\uparrow}\rangle|1\rangle_{ph}\right)$ and $\left(|\tilde{\downarrow}\rangle|1\rangle_{ph}, |\tilde{\uparrow}\rangle|0\rangle_{ph}\right)$, respectively. This requires the laser pulse to focus on either ion individually. Experimentally, this implies additional optical paths besides that in Fig. 3.3. The resultant wave function reads

$$\alpha_0|\tilde{\downarrow}\rangle|0\rangle_L|0\rangle_{ph} - i\alpha_1|\tilde{\downarrow}\rangle)|1\rangle_L|0\rangle_{ph} + \alpha_2|\uparrow_1\uparrow_2\rangle|0\rangle_L|0\rangle_{ph}. \tag{3.52}$$

7. $3\pi/2$-pulse between $|\tilde{\downarrow}\rangle|1\rangle_L$ and $|\tilde{\uparrow}\rangle|0\rangle_L$:

   Finally, we convert the middle term's photon excitation back to that of the ion. To remove the phase, we use a $3\pi/2$-pulse. Similar to step 5, the final result is

$$\left(\alpha_0|\downarrow_1\downarrow_2\rangle + \alpha_1|\tilde{\uparrow}\rangle) + \alpha_2|\uparrow_1\uparrow_2\rangle\right)|0\rangle_L|0\rangle_{ph}, \tag{3.53}$$

   as we aimed for in Eq. 3.35 via this protocol.

8. two-ion phase gate:

   We have completely described a pulse sequence to realize a quantum memory for photon number states. Nonetheless, the system can be used as a photonic gate for two-photon excitation. Using e.g. a Mølmer-Sørensen gate [SM99], one can flip the sign for the last term before step 7, so the result in step 7 becomes

$$\left(\alpha_0|\downarrow_1\downarrow_2\rangle + \alpha_1|\tilde{\uparrow}\rangle) - \alpha_2|\uparrow_1\uparrow_2\rangle\right)|0\rangle_L|0\rangle_{ph}. \tag{3.54}$$

   Reverting the gates above would then give the photon number state

$$\alpha_0|0\rangle_L + \alpha_1|1\rangle_L - \alpha_2|2\rangle_L. \tag{3.55}$$

3.3.4 Generalization to multiple ions

The protocol we have described above can be easily generalized to a system of N ions [LLC+11, Lei09]. The advantage of an N-ion system is that first it can be used as a quantum memory for an N-photon system. Secondly, even for a single or 2-photon mapping, the $\sqrt{N}$ enhancement for coupling strength can be quite useful, for the mapping can be done to a collective ion state as a transducer, then to a single ion. The formalism generalization for an N-ion system is described as follows.

Because the field strength on each ion can be different, the collective ion excitation state for ion-photon coupling is not a trivial symmetric wave function as in Eq. 3.42, but a rather complicated wave function

$$|\tilde{\uparrow}_C\rangle \equiv \sum_{k=1}^{N} \frac{\Omega_{k,C} g_k}{2\delta \tilde{g}_C} |\uparrow_k\rangle \bigotimes_{l\neq k}^{N} |\downarrow_l\rangle, \tag{3.56}$$

where

$$\tilde{g}_C \equiv \sqrt{\sum_{k=1}^{N} \left| \frac{\Omega_{k,C} g_k}{2\delta} \right|^2}. \tag{3.57}$$

The subscript k denotes the Rabi frequency for the Raman process and coupling strength to the cavity field for the k^{th} ion.

Similarly, the collective excitation state for ion phonon coupling reads

$$|\tilde{\uparrow}_L\rangle \equiv \sum_{k=1}^{N} \frac{\Omega_{k,L}}{\tilde{\Omega}_L} |\uparrow_k\rangle \bigotimes_{l\neq k}^{N} |\downarrow_l\rangle, \tag{3.58}$$

where

$$\tilde{\Omega}_L \equiv \sqrt{\frac{\sum_{k=1}^{N} |\Omega_{k,L}|^2}{N}}, \tag{3.59}$$

with the ion-position specific quantities indexed by k.

As we can see above, $|\tilde{\uparrow}_C\rangle$ and $|\tilde{\uparrow}_L\rangle$ are not necessarily equal. To use our protocol,

it is necessary to establish a phase matching condition where $|\tilde{\uparrow}_C\rangle = |\tilde{\uparrow}_L\rangle$. That is

$$\frac{\Omega_{k,C} g_k}{2\delta \tilde{g}_C} = \frac{\Omega_{k,L}}{\tilde{\Omega}_L}. \tag{3.60}$$

Because both hands of the equation are normalized quantities, we only need to consider the position dependence of g_k, $\Omega_{k,C}$ and $\Omega_{k,L}$. In the configuration depicted in Fig. 3.3,

$$g_k \sim e^{-r_k^2/w_0^2}, \quad \Omega_{k,C} \sim e^{i\cos\theta k_C r_k} e^{-(r_k \sin\theta)^2/w_L^2}, \quad \Omega_{k,L} \sim e^{ik_L r_k}, \tag{3.61}$$

where the position of each ion is denoted as r_k. For each laser and cavity field, the wave number is represented by k_C, k_L, k_0, and the Gaussian waist is denoted w_C, w_L, w_0. To satisfy the phase matching condition, the wave vector of the lasers are chosen so that

$$\cos\theta k_C = k_L, \tag{3.62}$$

and the laser waist is chosen so that

$$e^{-(r_k \sin\theta)^2/w_L^2} e^{-r_k^2/w_0^2} \sim \text{const.}, \tag{3.63}$$

which suggests to use collimated laser beams, and a cavity with a large waist relative to the ion chain length. We will show an experimental design based on this configuration in the next section, where strong coupling for a single ion can be possible. An alternative configuration is also suggested in Ref. [LLC+11, Lei09], for which the ion chain size is not limited with respect to the cavity waist. However, a scalable design of an integrated cavity-ion system is quite challenging for this configuration. The plane where the ion chain lives is in orthogonal to the cavity axis, making the photolithograhpic technique inaccessible for a ion-cavity integrated system (See, e.g. Ref. [HWS+11]).

The pulse sequence for an m-photon ($m < N$) quantum memory is the same as in the two ion case, except that step 1-7 needs to be duplicated to map down the

m-photon excitation. In step 6, m particular ions need to be chosen in the N-ion chain, which are individually addressed.

3.3.5 Requirement for implementation

The experimental requirement for implementing the above two-photon protocol include all three conditions for single ion implementation (See Eq. 3.32 through 3.34)[2]. In addition, the following conditions need to be fulfilled for the trapping of multiple ions

4. Photon and phonon decay:

   Because cavity photons experience decay process during the time the ion internal states are interacting with the phonon, we need to make sure that the decay rate is negligible compared to the Rabi frequency. The same principle applies to the phonon decoherence during the cavity QED process, except that in general, the phonon numbers increase, rather than decay. This decoherence rate is referred as heating rate $d\bar{n}/dt$. Written in equations, these two conditions result in

   $$\kappa \ll \eta\Omega_L, \quad \frac{d\bar{n}}{dt} \ll \tilde{g}. \tag{3.64}$$

5. Trapping of a chain of N ions:

   The trap secular frequency[3] for the radial ($\omega_{sec,r}$) and axial direction ($\omega_{sec,a}$) must satisfy [WMI+98]

   $$\omega_{sec,r} > 0.73N^{0.86}\omega_{sec,a}. \tag{3.65}$$

6. Ground state cooling for a chain of N ions.

7. Ability of individual addressing for each ion (two ions at least for the two photon excitation mapping).

[2] For Eq. 3.32, an enhancement of $\sqrt{N}$ is added to the condition for strong coupling regime
[3] See Sec. 2.1.1.

8. Frequency discrimination for the motional phonon $|n\rangle_{ph}$ (center of mass at least).

9. Phase matching:

$$1 - |\langle \tilde{e}_L | \tilde{e}_C \rangle|^2 \ll 1 \tag{3.66}$$

3.4 Two-ion experiment design with $^{88}Sr^+$ qubit

In this section, we present a design for a two-ion experiment, in which the pulse sequence for a two-photon quantum memory can be implemented. The schematic follows that presented in Fig. 3.3. The level structure of $^{88}Sr^+$ and the scheme for the Λ configuration is presented in Sec. 3.4.1. The detailed system design and evaluation is presented in Sec. 3.4.2.

3.4.1 $^{88}Sr^+$ Qubit and vacuum stimulated Raman transitions

A diagram for $^{88}Sr^+$ qubit level structure is shown in Fig. 3.4.1-a,c. The lowest three energy levels of a hydrogen-like $^{88}Sr^+$ ion are used for qubit implementation. Between the ground state $5S_{1/2,m_j=-1/2}$ and a meta-stable state $4D_{5/2,m_j=-5/2}$ (decoherence time 390 ms), a qubit transition $|\downarrow\rangle \rightarrow |\uparrow\rangle$ is defined. A 674 nm laser is used for this qubit addressing. To initialize the qubit to $|\downarrow\rangle$, the population in the $5S_{1/2,m_j=1/2}$ state and all magnetic sublevels of $4D_{5/2}$ need to be pumped through the $5P_{3/2}$ state via transition $5S_{1/2,m_j=1/2} \rightarrow 4D_{5/2,m_j=-3/2}$, and followed by a 1033 nm repumping transition. The state in $5P_{3/2}$ decays to the desired ground state $5S_{1/2,m_j=-1/2}$ and other states through spontaneous emission, and the latter can be repumped back again to $5P_{3/2}$ by repeating the initialization procedure. The qubit transition is also used for resolved sideband cooling on the ion motional state (See Sec. 2.2).

For qubit detection, a 422 nm Doppler transition between the $5S_{1/2}$ and $5P_{1/2}$ state is used. The scattered photon in this transition can be detected using a photo-multiplier tube (PMT), if the ion is in the ground state. Otherwise it remains dark.

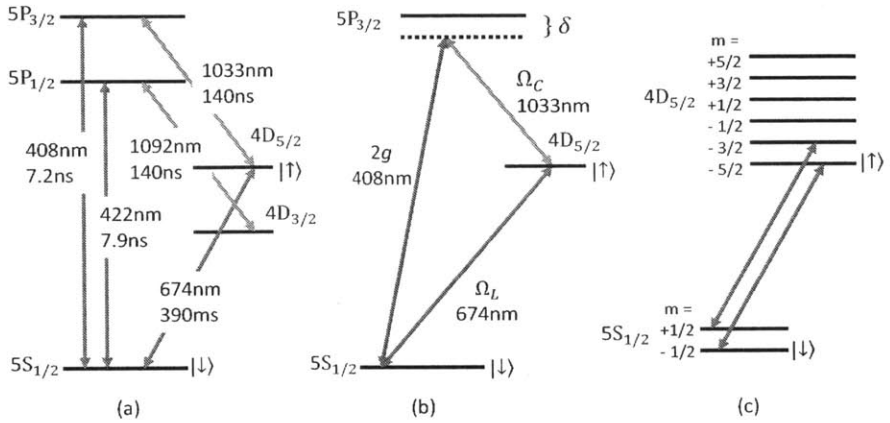

Figure 3-6: Atomic level structure for $^{88}Sr^{+}$ qubit implementation. (a) Wavelengths and decoherence time for relevant qubit operating transitions. Qubit transition is implemented on the 674 nm $5S_{1/2}$–$4D_{5/2}$ quadruple transition. The 422 nm $S_{1/2}$–$P_{1/2}$ dipole transition is used for Doppler cooling and qubit detection. If the ion is in the $|\downarrow\rangle$ state, it can scatter Doppler photons from an incident 422 nm laser, which can be detected through a PMT. Otherwise the ion remains dark. The 1092 nm laser is used to repump the population from $4D_{3/2}$ state to ensure Doppler cooling and detection efficiency. The 1033 nm laser is used to pump states from $|\downarrow\rangle$ to $|\uparrow\rangle$ via the $5P_{3/2}$ state for qubit initialization. The 408 nm laser is the used for the Raman scheme cavity coupling shown in (b). (b) Raman scheme and Λ structure chosen for cavity QED. Compared to Fig. 3.2 and Fig. 3.3, the $5S_{1/2}$, $4D_{5/2}$ and $5P_{1/2}$ state are used for $|\downarrow\rangle$, $|\uparrow\rangle$ and $|r\rangle$, respectively. For simplicity, we use the same detuning for the cavity and Raman transition, i.e. $\delta_C = \delta_A = \delta$. (c) Magnetic sublevels for qubit transition. Due to Zeeman splitting, the qubit transition is chosen to be the transition between $5S_{1/2,m_j=-1/2}$ and $4D_{5/2,m_j=-5/2}$. The population in $5S_{1/2,m_j=1/2}$ is pumped out via the $5S_{1/2,m_j=1/2} \rightarrow 4D_{5/2,m_j=-3/2}$ and 1033 nm repumping transitions.

During the detection process, the ion population in $5P_{1/2}$ can decay to the $4D_{3/2}$ state, which is repumped back using a 1092 nm laser. This Doppler cycle is not only used for detection, but also for initial cooling of the ion motion prior to sideband cooling, to allow for stable trapping.

The Raman scheme (c.f. Fig. 3.2 and Fig. 3.3) for ion-cavity coupling is shown in Fig. 3.4.1, where the cavity and Raman transitions are chosen to be $5S_{1/2,m_j=-1/2} \rightarrow 5P_{3/2,m_j=-3/2}$ and $4D_{5/2,m_j=-5/2} \rightarrow 5P_{3/2,m_j=-3/2}$, respectively. For simplicity, we have chosen $\delta_C = \delta_A = \delta$.

3.4.2 System design and evaluation

A system for single (few) ion cavity QED is difficult to implement. Of all requirements for experiment, the strong coupling condition is the first one we need to consider. The scaling $\eta_C \sim \mathcal{F}/w_0^2$ in Eq. 3.16 suggests that a desired cavity system design with a large finesse and small cavity waist.

The former requires high-reflectivity dielectric mirrors [RTKL92], and the latter requires a short ion-mirror distance and a small mirror radius of curvature (ROC), for cavity mode stability [ME88]. However, because dielectric materials are found charging, and hence affecting trapping potentials in the vicinity of laser fields [WHL+11], a design with short ion-mirror distance is usually extremely challenging. Experimental efforts now focus on reducing the amount of mirror exposure to the ions. One method is to use laser-machined micro-mirrors, which have been integrated to many experiment involving cavity QED [HSC+10, SMD+13, BMS+13]. The ROC and effective area of such micro-mirrors can be as small as a $\sim$100 μm. In this section, we present a design where the micro-mirrors are used. In addition, the cavity axis is designed normal to the trap plane, so the cavity mode goes through an aperture in the trap central electrode, which further shields the ion exposure to mirrors.

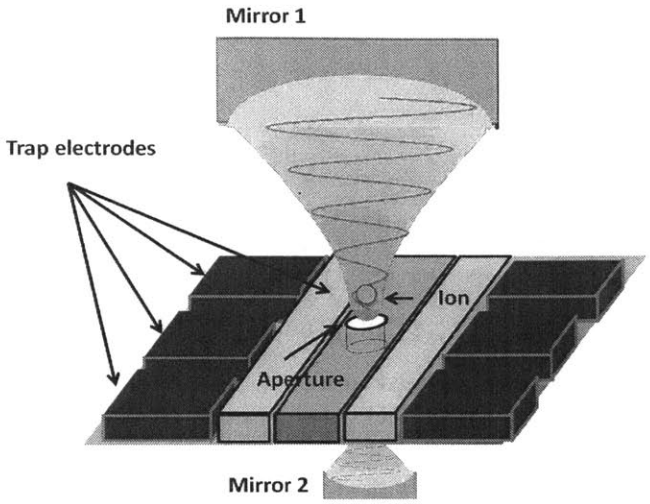

Figure 3-7: Schematic of the cavity trap design. A planar ion trap is inserted between two curved cavity mirrors, which form a cavity mode through the central aperture of the trap. The cavity is designed such that the ROC for the bottom and top mirror follows $R_2 \ll R_1$, and the cavity length L satisfies $R_1 < L < R_1 + R_2$. In such case, the cavity waist, and hence the ion position is much closer to mirror 2, which contributes predominantly to the dielectric surface charging noise. This noise can be minimized by the shielding effect provided by the trap aperture, which can be made as small as close to the scale of the cavity waist (limited by the cavity clipping loss). In place of the single ion depicted, a two-ion chain can be formed along the trap axis, orthogonal to the cavity axis, allowing for the implementation of configuration in Fig. 3.3.

Cavity trap design

A schematic of the ion-cavity system is presented in Fig. 3.4.2, where a planar ion trap is inserted between two curved cavity mirrors. At the center of the central ground electrode is an aperture, through which a cavity mode can be formed. The cavity is designed such that the ROC for the bottom and top mirror follows $R_2 \ll R_1$, and the cavity length L satisfies $R_1 < L < R_1 + R_2$. In such case, the cavity waist, and hence the ion position is much closer to mirror 2, which contributes predominantly to the dielectric surface charging noise. This noise can be minimized by the shielding effect provided by the trap aperture, which can be made as small as close to the scale of the cavity waist (limited by the cavity clipping loss).

System evaluation

The cavity-trap system shown in Fig. 3.4.2 is originally proposed in Ref. [Lei09], and a prototype of the trap without the upper cavity mirror is realized in Ref. [HWS+11, Wan12] at cryogenic temperature. In addition, more efforts in realizing the cavity-trap system at room temperature are shown in Chapter 4 and Chapter 5. As the last part of this chapter, we evaluate the experimental feasibility in this system for our two-photon quantum memory protocol.

The requirements for experiment implementation are summarized in Eq. 3.32 through 3.34, and Eq. 3.64 through 3.66. We examine each requirement with the planned experimental parameters listed in Table 3.1

1. Strong coupling:

   Because of the Λ configuration and Zeeman splitting, the cavity cooperativity η_C in Eq. 3.16 for the strong coupling regime $\eta_C \gg 1$ is modified by two factors, which becomes

   $$\frac{24\mathcal{F}}{\pi k_0^2 w_0^2}\frac{\Gamma_{P_{3/2}\to S_{1/2}}}{\Gamma_{P_{3/2}}}C_{P_{3/2,m_j=-3/2}\to S_{1/2,m_j=-1/2}} = 91 \gg 1, \tag{3.67}$$

   where the two correction terms from left to right are the branching ratio and Clebsch-Gordan (CG) coefficient. These two terms arise because in the derivation from Eq. 3.14 to 3.15, we have canceled the dipole moment d_e from Eq. 3.1 and 3.9 in a two level system. The branching ratio corrects for the spontaneous decay of state $P_{3/2}$ to $S_{1/2}$ and $D_{5/2}$, which can be obtained using the life times in Fig. 3.4.1. The CG coefficient $C_{P_{3/2,m_j=-3/2}\to S_{1/2,m_j=-1/2}} = 1$ corrects for the dipole in the driven transition $P_{3/2,m_j=-3/2} \to S_{1/2,m_j=-1/2}$ vs that for $P_{3/2,m_j=-3/2}$ decaying via all possible channels. The value of $\eta_C = 91$ is obtained with the a cavity finesse $\mathcal{F} = 95000$, and cavity waist of 5.6 μm. The corresponding cavity geometry and coating properties are $R_1 = 200$ mm, $R_2 = 500\mu$m and $L = 200.2$ mm; $\mathcal{T}_1 = 60$ ppm, $\mathcal{T}_2 = \mathcal{L}_1 = \mathcal{L}_2 = 2$ ppm. The

cavity coating is with a 2 ppm mirror coating might be challenging, since it has only been achieved at wavelengths near IR, e.g. 854nm in Ref. [HKY01].

We also recall the condition that the auxiliary state decay is negligible is equivalent to the strong coupling in Eq. 3.32 when $\kappa \sim g\Omega_C/\delta_A$. In the chosen parameters, we have $\kappa = 2\pi \times 8$ kHz, and $g\Omega_C/\delta_A = \tilde{g}_C/\sqrt{2} = 2\pi \times 12.9$ kHz.

2. Decoherence in Control: It is feasible to achieve a sub-kHz linewidth from cavity locking using the Pound-Drever-Hall technique [DZM+96], and even sub-Hz linewidth from the Raman laser by locking it to an ultra-low expansion (ULE) cavity [AMK+08]. In the used parameters, we take $\gamma_{cav} = 2\pi \times 1$ kHz, and $\gamma_\Omega = 2\pi \times 1$ Hz. A typical magnetic field noise B_{rms} of 1 mG can be assumed [HAB+14], and hence $\mu_B B_{rms}/\hbar \simeq 2\pi \times 1$ kHz. Therefore, we have for the total noise contribution

$$\gamma_\Omega + \gamma_{cav} + \mu_B B_{rms}/\hbar = 2\pi \times 2\text{kHz} \ll \kappa, g\Omega_C/\delta_A = 2\pi \times 12.9\text{kHz}. \quad (3.68)$$

3. Cavity loss vs. photon transmission:

With the selected coatings and cavity geometry, we can use mirror 1 as the incoupling mirror. Therefore, the ratio of the transmission loss at the incoupling mirror to the overall cavity loss follows

$$\frac{\mathcal{T}_1}{\mathcal{T}_1 + \mathcal{T}_2 + \mathcal{L}_1 + \mathcal{T}_2} = 0.91. \quad (3.69)$$

4. Photon and phonon decay:

To compare the photon decay rate during the qubit sideband transition process, we have $\kappa = 2\pi \times 8$ kHz $\ll \eta\Omega_L = 2\pi \times 100$ kHz. On the other hand, a typical heating rate of 2 s^{-1} can be achieved, satisfying $d\bar{n}/dt \ll \tilde{g}_C = 18.2$ kHz.

5. Trapping of two ions:

A radial secular frequency $\omega_{sec,r} = 3$ MHz and axial secular frequency $\omega_{sec,a} = 0.5$ MHz are both feasible, and can satisfy the condition in Eq. 3.65.

6. Ground state cooling of two ions:

   Ground state cooling of two ions can be achieved using sideband cooling, in a similar way for single ions, where by illuminating one of the two ions with a red sideband qubit laser, the common mode is cooled sympathetically [MECZ99, RGR+01].

7. Individual addressing for each ion:

   Individual addressing can be accomplished by steering the laser beams with acousto/electro-optic modulators [SKHR+03, YKU+06], or with MEMS-based steering systems [CMBK14].

8. Frequency discrimination for center of mass mode:

   The center of mass frequency is the same as the trap axial secular frequency, according to Ref. [Jam98], which we choose to be $\omega_{sec,a} = 0.5$MHz. For two ions, the other common mode (breathing mode) frequency is at $3\omega_{sec,a}$, which is 1 MHz away from that of the center of mass mode. This is well resolvable for the qubit transition.

9. Phase matching:

   The phase matching fidelity $\left|\langle\tilde{\uparrow}_L|\tilde{\uparrow}_C\rangle\right|^2$ can be obtained from Eq. 3.56 and3.58 as

$$\left|\langle\tilde{\uparrow}_L|\tilde{\uparrow}_C\rangle\right|^2 = \frac{\left(\sum_{i=1}^{2} e^{-z_i^2/w_{ion}^2 - z_i^2\sin^2\theta/w_L^2}\right)^2}{2\sum_{i=1}^{2} e^{-2z_i^2/w_{ion}^2 - 2z_i^2\sin^2\theta/w_L^2}}. \tag{3.70}$$

   The ion position $z_{1,2}$ can be obtained from Ref. [Jam98]. Because $z_1 = -z_2$, the above simplifies to $\left|\langle\tilde{\uparrow}_L|\tilde{\uparrow}_C\rangle\right|^2 = 1$. This is precisely the case we derived fro two ions in Eq. 3.43, where $|\tilde{\uparrow}_C\rangle = |\tilde{\uparrow}_L\rangle$.

From the above analysis, we observe that the two most challenging parts of the implementation are experimental noise control and optical coating. We see that in condition 2, the upper bound for the experiment noise is set by κ, which is itself bounded from above due to strong coupling, and the qubit red sideband Rabi frequency $\eta\Omega_L$ in condition 1 and 4, respectively. The stabilization of cavity and laser

linewidth, as well as the magnetic field noise is thus extremely important to the experiment. Also due to the upper bound of κ in condition 1 and 3 to ensure the high fidelity of photon transfer through the desired transmission, the requirement on cavity scattering loss could thus be challenging.

3.5 Conclusion and discussion

We have established the theoretical framework for ion-photon interaction in this chapter. A quantum network node consisting of single trapped ions in high finesse optical cavities is described. The dynamics of ions and photons is described using cavity QED. We also expand the model of single ions to two-ion and multiple-ion models. The increase of number of ions not only enhances the ion-photon coupling, but can also be used for quantum memory for higher photon number states. We have analyzed the requirements for the implementation of a two-ion photon memory experiment, and have concluded that the experiment is feasible under typical experimental parameters, but could be challenging due to requirements on noise control and cavity mirror optical coatings.

Table 3.1: Experiment parameters for two ion photon memory experiment

Parameter	Value
Cavity field wavelength, λ_C	408 nm
Cavity length, L	200.2 mm
Cavity mirror 1 radius of curvature, R_1	200 mm
Cavity mirror 2 radius of curvature, R_2	0.5 mm
Cavity waist, w_0	5.64 μm
Waist height (distance from mirror 2), h_2	200 μm
Waist at mirror 1, w_1	4.5 mm
Waist at mirror 2, w_2	7.3 μm
Cavity mirror 1 transmission, $\mathcal{T}_1$	60 ppm
Cavity mirror 2 transmission, $\mathcal{T}_2$	2 ppm
Cavity mirror 1 loss, $\mathcal{L}_1$	2 ppm
Cavity mirror 2 loss, $\mathcal{L}_2$	2 ppm
Cavity decay rate, κ	$2\pi\times8$ kHz
Number of ions	2
Trap height, h	150 μm
Trap radial secular frequency, $\omega_{sec,r}$	$2\pi\times3$ MHz
Trap axial secular frequency, $\omega_{sec,r}$	$2\pi\times0.5$ MHz
Center of mass mode frequency, $\omega_{sec,CM} = \omega_{sec,r}$	$2\pi\times3$ MHz
Lamb Dicke parameter, η	0.1
Qubit Rabi frequency, Ω_L	$2\pi\times1$ MHz
Qubit red sideband Rabi frequency, $\eta\Omega_L$	$2\pi\times100$ kHz
Auxiliary state decay rate, $\Gamma_{P_{3/2}}$	$2\pi\times23.4$ MHz
Branching ratio, $\Gamma_{P_{3/2}\rightarrow S_{1/2}}/\Gamma_{P_{3/2}}$	0.95
CG coefficient, $C_{P_{3/2,m_j=-3/2}\rightarrow S_{1/2,m_j=-1/2}}$	1
Raman laser detuning, δ	$2\pi\times1$ GHz
Raman laser Rabi frequency, Ω_C	$2\pi\times2$ MHz
Collective cavity coupling strength $\tilde{g}_C$	18.2 kHz
Cooperativity, η_C	91
Raman laser linewidth γ_Ω	$2\pi\times1$ Hz
Cavity lock linewidth γ_{cav}	$2\pi\times1$ kHz
Magnetic field noise, B_{rms}	1 mG

Chapter 4

Mirror trap and microcavity ion trap system

In Chap. 3, we proposed that an efficient ion-photon interface can be realized using a micro-mirror cavity design with its axis orthogonal to a planar trap. While the cavity mode through the trap aperture interacts with the ion in the strong coupling regime, the electric field noise due to the mirror dielectric surface charging can be minimized due to the trap electrode shielding. In this chapter, we describe a system implemented for such ion-cavity design, which can potentially be used to realize single ion cavity QED.

A prototype of the system was demonstrated in Ref. [HWS+11] and Chapter 9 of [Wan12], where we fabricated the trap with aperture, and demonstrated stable ion trapping in a bath cryogenic vacuum system [ASA+09]. A major challenge to realize an ion-cavity experiment using the system in Ref. [ASA+09] is that a bath cryogenic system requires a cryogen refill, and hence a temperature cycling every 24 hours. The optics alignment shifts due to thermal expansion and contraction induced by this temperature cycling is certainly non-ideal for experiment that involves cavity alignment.

The system presented in this chapter is implemented with a room temperature UHV enclosure, which does not require frequent temperature cycling. The sections

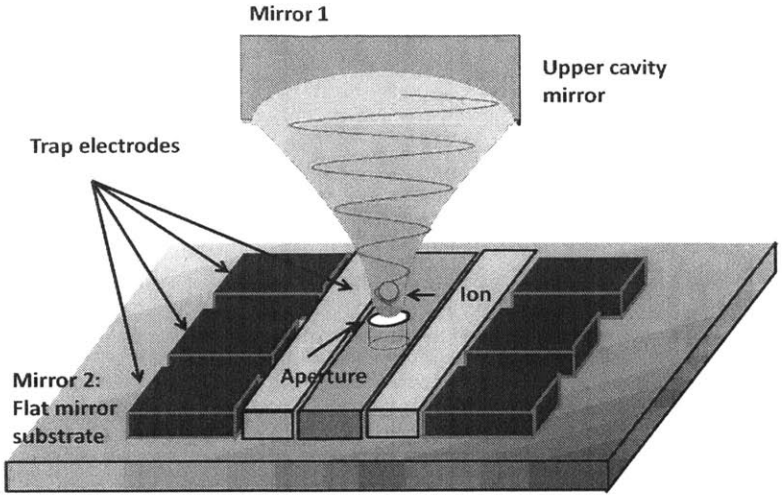

Figure 4-1: Schematic of the cavity trap design with flat bottom mirror. A planar ion trap is fabricated directly on a high-reflectivity mirror substrate, with an aperture left on the central ground electrode. Through the aperture, a cavity field is formed between the mirror substrate and another curved mirror above the trap, for which the waist is on the flat mirror surface. With a low trapping height satisfying $h_{ion} \ll z_0$, the Raleigh range of the cavity mode, the ion is close enough to the cavity waist to realize strong coupling. In such case, the dielectric surface charging noise comes predominantly from mirror 2, and can be minimized by the shielding effect from trap aperture, which can be made as small as close to the scale of the cavity waist (limited by the cavity clipping loss).

are organized as follows. Sec. 4.1 presents the system design. Sec. 4.2 describes the trap fabrication process. Characterizations of the micro-mirrors are shown in Sec. 4.3. Stable ion trapping in the system is demonstrated in Sec. 4.4.

4.1 Design

We present the design of a cavity-trap system in this section, where $^{88}Sr^{+}$ and the Raman scheme proposed in Sec. 3.4.1 for cavity QED is used. To realize strong coupling for single ions, the parameters expected are listed in Table 4.1.

4.1.1 Cavity

The design of the cavity trap system is slightly different from that in Sec. 3.4. Instead of choosing $R_2 \ll R_1$ and L satisfies $R_1 < L < R_1 + R_2$ to bring the ion position close to the trap surface, we choose to follow the design with $R_2 \gg R_1$ and $L < R_1$. To maintain a small cavity waist w_0, R_1 is chosen to be small ($\sim$500 μm). In the limit $R_2 \to \infty$, the bottom mirror reduces to a flat mirror substrate (see Fig. 4.1). In this case, the cavity waist is at the surface of mirror 2. Provided the Rayleigh range $z_0 = \pi\lambda_C^2/w_0$ is not large, the field waist at the ion position $w_{ion} = w_0\sqrt{1 + h_{ion}^2/z_0^2}$ can still be close to the cavity waist size w_0 to realize strong coupling, where λ_C is the cavity wavelength and h_{ion} represents the ion height above the trap surface.

This design has a number of advantages compared to that in Sec. 3.4. First of all, with a flat mirror surface, one can choose to fabricate the trap electrode directly on the mirror surface, which can greatly reduce the fabrication complexity. The design in Sec. 3.4 requires an aperture at the trap center, through both the trap electrode and substrate. The former can be obtained during the lithography step, in the same way the electrode gaps are processed (See, e.g. [Ge15]). The latter however, requires an extra step of etching through the substrate [DLMB12]. Secondly, a typical cavity waist size is on the order of 10 μm, which makes the alignment of the two cavity mirrors challenging with respect to the ion position. With the trap electrode fabricated on the mirror substrate, the bottom mirror can be considered automatically aligned with the ion, which reduces significantly the alignment difficulty.

The drawback of this design is that the fabrication process might result in extra absorption or scattering loss on the high-reflectivity cavity mirror. As we found in Ref. [HWS+11], a typical increase of $\sim$100 ppm absorption and scattering loss can be expected. In addition, the cavity length L is limited by the ROC of mirror 1 in this configuration, which can thus result in a large κ_C. This does not affect the cooperativity η_C, but can result in limited fidelity for processes involving multiple photon state mapping, such as the two photon quantum memory (see Eq. 3.64). As a result, we do not aim to fully implement the two photon quantum memory protocol

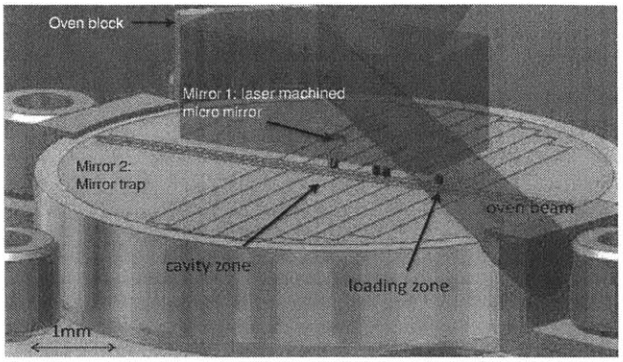

Figure 4-2: Segmented trap design. A mirror trap design is shown to scale (except ions). The segmented trap design can avoid possible contamination from oven flux, by separating the loading cavity zone. Shuttling of the ion can be implemented by varying the DC electrode voltages after the ion is trapped.

in this system, but to design it for demonstration of single ion cavity QED.

The specific parameters used can be found in Table 4.1. The anticipated loss $\mathcal{L}_{1,2}$ of the mirrors are obtained from Ref. [HWS+11] and Sec. 4.3.

4.1.2 Trap

The schematic of trap design is shown in Fig. 4.1.2, with the microcavity shown with the correct scale ratio. One challenge in such short-cavity design is to protect the cavity optical quality from ion loading. In such process, Sr metal is heated in a thermal oven, which produces a directional oven flux grazing across the trap surface. In a two-stage photo-ionization process using lasers with frequency 461 nm, and 405 nm respectively [Lab08], neutral Sr atoms in the trap region can be ionized to produce Sr^+ ions, which are thus confined in the trap potential and Doppler cooled subsequently. However, a typical size of Sr oven flux can be comparable to the distance between the cavity mirrors in our design. During the loading process, Sr atoms can thus contaminate the mirror surface, resulting in a degradation of the finesse. One approach to avoid the oven contamination is shown in Fig. 4.1.2, where a trap is segmented into several trapping zones, and the oven flux is confined with a block before the trap. In particular, ions are trapped in the loading zone (where oven contamination can be significant), and then shuttled to the cavity zone for experiment,

by varying the DC electrode voltages.

The trap electrode design is shown in layout in Fig. 4.1.2, and the relevant parameters are summarized in Table 4.1. We have used the design scheme according to Ref. [Hou08], where w_a, w_b and w_d, the width of the ground, RF, and DC trap electrode follows the ratio

$$w_b = 1.2w_a, \quad w_d = 4w_a. \tag{4.1}$$

The trap height $h_{ion} = 150$ μm is chosen according to Ref. [HWS+11] for optimal field waist and laser accessibility, which results in w_a =162 μm. The central aperture is chosen as r_0 =100 μm to avoid clipping loss, which is feasible for fabrication. The gap size $d_g = 10$ μm satisfies $d_g \ll w_a$, and thus will not affect the analytic results computed using Ref. [Hou08], which include the trap height h_{ion}, secular frequency $\omega_{sec,r}, \omega_{sec,a}$, trap depth Φ_0, and DC control voltage $V_{1,2,3,4,5}$ of the corresponding electrode (see Fig. 4.1.2). In particular, the DC control voltages are computed by minimizing the overall potential with respect to $V_{1,2,3,4,5}$ at the ion, i.e. above the aperture location $(x = 0, y = h_{ion})$

$$\sum_i V_i^2, \tag{4.2}$$

$$\text{subject to constraints} \qquad \sum_i \nabla\phi_{a,i} = 0, \quad \sum_i \frac{\partial^2\phi_{a,i}}{\partial z^2} = \frac{m\Omega_{RF}^2}{4Q}a_z, \tag{4.3}$$

which can be solved using Lagrangian multipliers. The first constraint ensures the DC field potential minimum overlaps with that of the RF field. The second constraint sets the desired axial secular frequency (see Eq. 2.11). The DC potential $\phi_{a,i}$ follows

$$\begin{aligned}\phi_{a,i} &= \frac{V_i}{2\pi}\left[\arctan\left(\frac{w_d}{h_{ion}}\right) - \arctan\left(\frac{(w_b + w_a/2)(z - z_{d,i})}{h_{ion}\sqrt{h_{ion}^2 + (w_b + w_a/2)^2 + (z - z_{d,i})^2}}\right)\right. \\ &+ \left.\arctan\left(\frac{(w_b + w_a/2)(z - z_{u,i})}{h_{ion}\sqrt{h_{ion}^2 + (w_b + w_a/2)^2 + (z - z_{u,i})^2}}\right)\right],\end{aligned} \tag{4.4}$$

where $z_{d,i}, z_{u,i}$ are the z-coordinate of the DC electrode i for the lower and upper

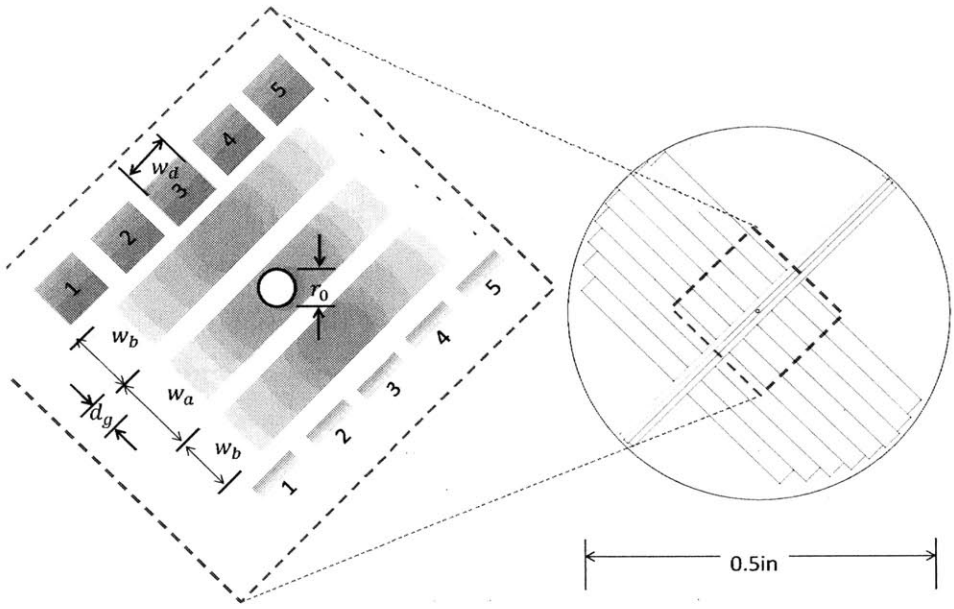

Figure 4-3: Schematic of mirror trap design. The trap electrode configuration is shown on a 0.5 inch high reflectivity mirror as the substrate for fabrication. The electrode widths are optimized such that $w_b = 1.2w_a$ and $w_d = 4w_a$ according to Ref. [Hou08]. The electrode gap size satisfies $d_g \ll w_a$.

corners, and bear the values $z_{u,1} = -5w_d/2$, $z_{d,1} = z_{u,2} = -3w_d/2$, $z_{d,2} = z_{u,3} = -w_d/2$, $z_{d,3} = z_{u,4} = w_d/2$, $z_{d,4} = z_{u,5} = 3w_d/2$, and $z_{d,5} = 5w_d/2$.

4.1.3 Assembly

The assembly design is shown in Fig. 4.1.3-a. The base plate holding the system is shown mounted in a 4.5 inch vacuum chamber via groove grabbers. The mirror trap packaged with an adapter is shown mounted at the center of the base plate. The upper cavity mirror connected to a piezo-electric tube (pzt) is aligned with the mirror trap via a tripod mounted on the base plate. With Pro Engineer, we have analyzed the resonant frequencies of the tripod-base-plate system, and found all modal frequencies lie within the range of 15.1-39.8 kHz. The resonant frequencies of the two modes coupled most strongly to the cavity length (shown in Fig. 4.1.3-b,c) are 23.9 and 36.4 kHz, respectively. To isolate acoustic noise from the system, Vespel SP3 (vacuum compatible plastic) spacers are used between the base plate and groove grabbers, which can isolate vibrations below approx. 50 Hz. To protect the cavity alignment from thermal effects, resistive heating can be used to maintain the system temperature. The heating block for the bottom plate as well as the holes for heating

Table 4.1: Experiment parameters for micro-cavity experiment

Parameter	Value
Cavity field wavelength, λ_C	408 nm
Cavity length, L	0.8 mm
Cavity mirror 1 radius of curvature, R_1	1 mm
Cavity mirror 2 radius of curvature, R_2	∞
Cavity waist, w_0	7.2 μm
Waist at ion, w_{ion}	7.6 μm
Waist at mirror 1, w_1	16 μm
Waist at mirror 2, w_2	7.2 μm
Cavity mirror 1 transmission, $\mathcal{T}_1$	45 ppm
Cavity mirror 2 transmission, $\mathcal{T}_2$	45 ppm
Cavity mirror 1 loss, $\mathcal{L}_1$	150 ppm
Cavity mirror 2 loss, $\mathcal{L}_2$	150 ppm
Cavity decay rate, κ	$2\pi\times12$ MHz
Number of ions	1
Trap ground electrode width, w_a	162 μm
Trap RF electrode width, w_b	194 μm
Trap DC electrode width, w_d	648 μm
Trap RF gap size, d_g	10 μm
Trap height, $h_{ion} = y_0$ (see Eq. 2.14)	150 μm
Trap RF voltage amplitude, V_{RF}	50 V
Trap RF frequency, Ω_{RF}	$2\pi\times13$ MHz
Trap depth, Φ_0	28.6 meV
Trap Mathieu q parameter, q	0.21
Trap axial Mathieu a parameter, a_z	0.01
Trap DC electrode voltage, V_1, V_2, V_3, V_4, V_5	0.0374, 1.66, -3.40, 1.66, 0.0374 V
Trap radial secular frequency, $\omega_{sec,r}$	$2\pi\times1$ MHz
Trap axial secular frequency, $\omega_{sec,r}$	$2\pi\times0.65$ MHz
Lamb Dicke parameter, η	0.1
Qubit Rabi frequency, Ω_L	$2\pi\times1$ MHz
Qubit red sideband Rabi frequency, $\eta\Omega_L$	$2\pi\times100$ kHz
Auxiliary state decay rate, $\Gamma_{P_{3/2}}$	$2\pi\times23.4$ MHz
Branching ratio, $\Gamma_{P_{3/2}\rightarrow S_{1/2}}/\Gamma_{P_{3/2}}$	0.95
CG coefficient, $C_{P_{3/2,m_j=-3/2}\rightarrow S_{1/2,m_j=-1/2}}$	1
Raman laser detuning, δ	$2\pi\times1$ GHz
Raman laser Rabi frequency, Ω_C	$2\pi\times2$ MHz
Cooperativity, η_C	8.4
Raman laser linewidth γ_Ω	$2\pi\times1$ Hz
Cavity lock linewidth γ_{cav}	$2\pi\times1$ kHz
Magnetic field noise, B_{rms}	1 mG

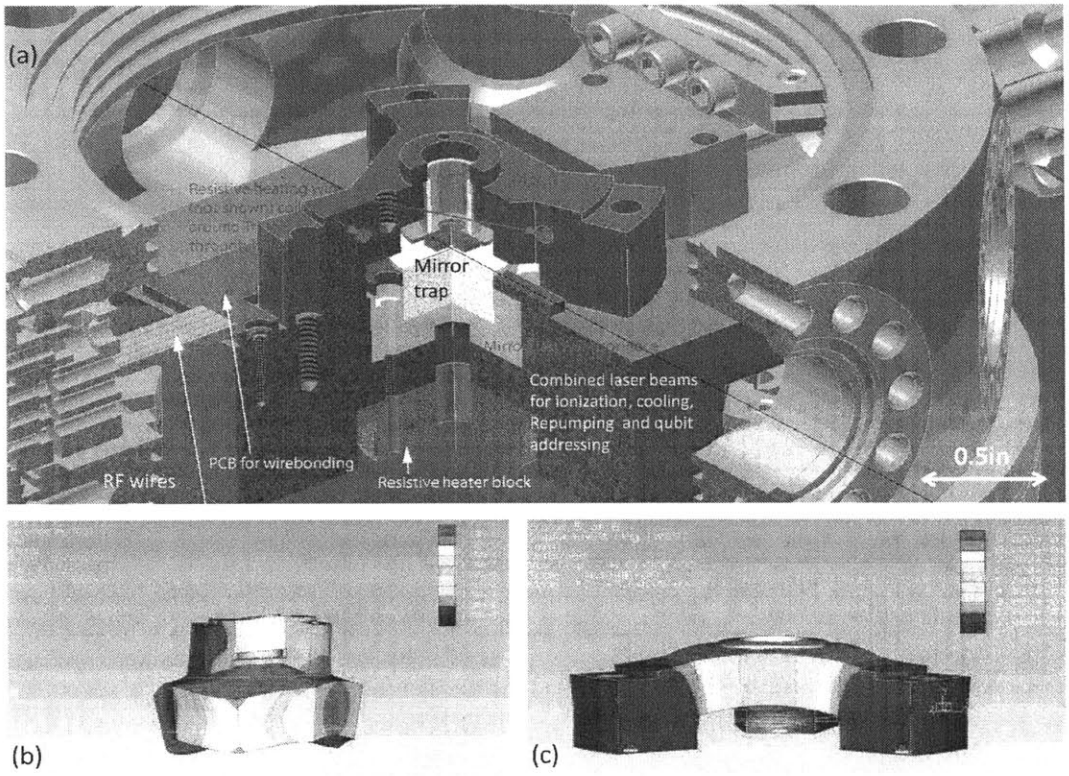

Figure 4-4: Assembly design of the cavity trap system. (a) the assembly design. The base plate holding the system is shown mounted in a 4.5 inch vacuum chamber via groove grabbers, with Vespel SP3 spacers in between. The mirror trap packaged with an adapter is shown mounted at the center of the base plate. The upper cavity mirror connected to a piezo-electric tube (pzt) is aligned with the mirror trap via a tripod mounted on the base plate. (b) and (c), the two normal modes of the base plate and cavity tripod system, which strongly couple to the cavity length. The resonant frequencies are 23.9 kHz and 36.4 kHz, respectively.

coils on the tripod are both shown. Also shown is the combined laser beam for ionization, cooling, repumping, and qubit addressing.

4.2 Trap fabrication

With a mature fabrication process developed in past experiments such as Ref. [WHL+11] for evaporated planar ion traps at cryogenic temperature, we attempted to fabricate traps using e-beam evaporation by re-optimizing the existing recipes in Ref. [Ge15]. During the development of the new recipe, we have realized that these evaporated traps are not suitable for room temperature operation. When high RF voltages (300-400 V_{pp}) are applied across the RF electrodes, the rough metallic edges can result in violent discharging events, and hence undesired noise for trapping fields. This effect is greatly suppressed at cryogenic temperatures, but can be significant for room temperature trapping. A new fabrication process is thus developed as a solution using electroplating. Traps fabricated using both recipes are presented in this section for comparison.

4.2.1 Evaporated trap

The trap fabrication process based on e-beam evaporation is shown in Fig. 4.2.1. Compared with methods involving chemical etching, such as those used in Ref. [LGA+08] and Sec. 4.2.2, this method involves fewer steps in the process, and less chemical processing.

Fabrication process

The fabrication process is developed based the method from Chapter 9.1 of Ref. [Wan12] and Chapter 3.3 of Ref. [Ge15]. The detailed steps are listed below.

1. Sample preparation:

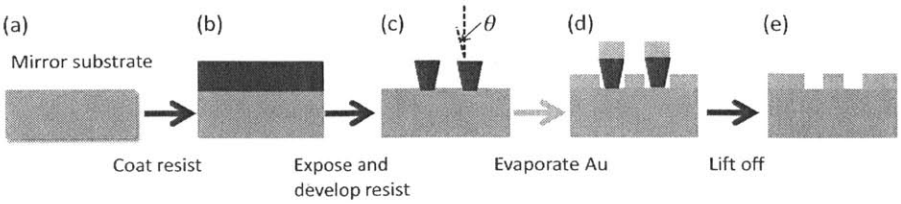

Figure 4-5: Schematic of mirror trap fabrication with e-beam evaporation. (a) a high reflectivity mirror substrate is prepared for fabrication. (b) a layer of photoresist is spin-coated on the mirror surface. (c) using contact exposure followed by resist development, the photoresist is patterned for trap electrode configuration, where resist remains along the trap gaps. The angle θ is an important feature for lift-off resist, which avoids lateral metallic coating, and thus makes the lift-off step easy, as illustrated in (d) and (e). (d) with e-beam evaporation, metal electrodes form on the mirror surface following the resist pattern. (e) after lift-off, the resist in the trap gaps are removed.

(a) Mirror quality testing: the mirror loss, including the transmission $\mathcal{T}$ and scattering/absorption loss $\mathcal{L}$ is measured in a Fabry-Pérot cavity, formed with another pre-characterized curved mirror, using standard cavity ring-down spectroscopy (see Appendix A). After a manual cleaning procedure, this measured loss is compared to the factory standard from Advanced Thin Films (ATF) from Boulder, CO to scrutinize major sample defect. The nominal values are $\mathcal{T} = 45$ ppm and $\mathcal{L} = 25$ ppm at 422 nm. A general loss increase of approx. 100 ppm is expected after fabrication, as characterized in Ref. [HWS+11]. The manual cleaning procedure is listed below:

   i. Put on latex gloves.

   ii. Empty the drop bottles containing acetone and methanol solutions used for cleaning mirrors. Blow dry the drop bottles with dry N_2 gas.

   iii. Fill the drop bottles with ultra-pure acetone and methanol (>99.9%, e.g. Sigma Aldrich 270725, 34860), respectively.

   iv. Fold and hold a piece of optics cleaning tissue 4 times with a clean pair of forceps.

v. Use the drop bottle to apply 2 drops of acetone on the folded tissue and clean the mirror surface once along one direction with moderate force.

vi. With a new piece of optics tissue, repeat cleaning with acetone along the orthogonal direction.

vii. Repeat the above cleaning procedure with acetone replaced by methanol.

(b) Surface cleaning:

i. Rinsing: Hold mirror substrate with tweezers with top surface facing up and tilted by 45°. Use a squeeze bottle to rinse the mirror surface with ACS grade isopropanol alcohol (IPA) for 30 s.

ii. Blowing dry: Place mirror down on a clean cleanroom wipe (e.g. AlphaWipe cleanroom wipers, ITW Texwipe), with top surface facing up. Blow the the surface dry with dry N_2, with flux orthogonal to the mirror surface.

2. Lithography:

(a) substrate baking: Bake the substrate on a hot plate at 150°C for 5 min with mirror top surface up, to remove water vapor. Place the substrate on a cleanroom wipe and wait until it cools down for 1 min, top surface up.

(b) Resist coating:

i. Center the mirror substrate on the spin coater, and adjust the speed to 750 rpm.

ii. Stop the spin coater. With a clean pipette, add 2 drops of NR9-3000PY (make sure no air bubbles) on the mirror surface from the center, and wait till the resist relaxes and covers the full surface (typically 10 s).

iii. Spin the sample at 750 rpm for 10 s, and gradually accelerate the speed to 3000 rpm in 5 s. Keep the sample spinning at 3000 rpm for 50 s.

(c) Pre-baking: Bake the sample at 150°C for 1 min (c.f. step 2-(a)).

(d) Exposure:

i. With a clean mask, align the sample under microscope, and make tight contact between the sample and mask using vacuum suction (make sure no air bubble).

ii. Expose sample for 7 min with UV intensity of 850 $\mu W/cm^2$.

(e) Post-baking: 2 min at 90°C (c.f. step 2-(a)).

(f) Development: Submerge the sample in RD6 solution and rinse for 20 s. Quickly rinse with tap DI water for 30 s, and blow dry (c.f. step 1-(b)-ii).

3. E-beam evaporation: E-beam evaporate 10 nm of Ti followed by 500 nm Au, at a rate of 5 Å/s.

4. Lift-off: Rinse in ASC grate Acetone for 5 min, followed by a 30 s IPA rinse (c.f. step 1-(b)-i), and blow dry (c.f. step 1-(b)-ii).

5. Post processing: to minimize the mirror surface contamination accumulated during the fabrication process, the sample is cleaned with Piranha solution following the procedure below:

(a) Pour 1 volume of 30% hydrogen peroxide solution in the beaker designated for piranha cleaning.

(b) Pour 3 volumes of sulfuric acid in the beaker, and mix with a clean stirring rod.

(c) Measure the solution with a clean thermometer until the temperature stabilizes to 95 deg C.

(d) Hold the sample in a clean Teflon basket, and slowly immerse the basket in the piranha solution.

(e) After 15 min, clean the sample with running tab DI water for 1 min, while in the basket.

(f) Take the sample out of the basket and blow dry with dry N_2 (c.f. step 1-(b)-ii).

RF breakdown

We have discovered that the traps fabricated using the above methods exhibit RF breakdowns on parts of the electrodes, with RF (typically 20 MHz) voltage of approx. 200 V_{pp} applied under vacuum. During the breakdown process, violent discharging events takes place, as shown in Fig. 4.2.1-a. These discharging events can be a significant noise source for the trapping field, as well as the ion internal state level mixing.

With SEM imaging (Fig. 4.2.1-c), we have found that the regions on the electrode exhibiting RF breakdowns have a particular pattern, where clusters of metallic bubbles (500 nm typical width) form along the electrodes. This pattern is not observed for regions with no breakdown points (Fig. 4.2.1-b). When high voltage RF signals are applied on electrodes with bubbles nearby, electrons are emitted and accumulate on these bubbles, which can thus cause discharging when the signal polarity is switched. The electron emission process from electrodes is a thermal process, which is strongly suppressed at cryogenic temperatures. This is confirmed from observations of similar bubble patterns on traps tested in the experiment in Ref. [HWS+11], for which no points of breakdown were found (Fig. 4.2.1-d).

The bubbles found in Fig. 4.2.1-c,d were found correlated to the undercutting feature of the lift-off photo-resist. During evaporation, metal layers are formed between the resists, but due to the undercuts, leaving a ~500 nm region not coated (c.f. Fig. 4.2.1-c,d). Some metallic particles can still accumulate in this region due to random walks, forming the bubbles observed. This is illustrated in Fig. 4.2.1-e.

The undercut geometry is however important for lift off processes. Otherwise evaporated metal layers can coat continuously from lateral to top surfaces of the photo resist, making the lift off process difficult. Figure 4.2.1-g illustrates an extreme example of resist without undercut feature (formed by resist under-exposure). We

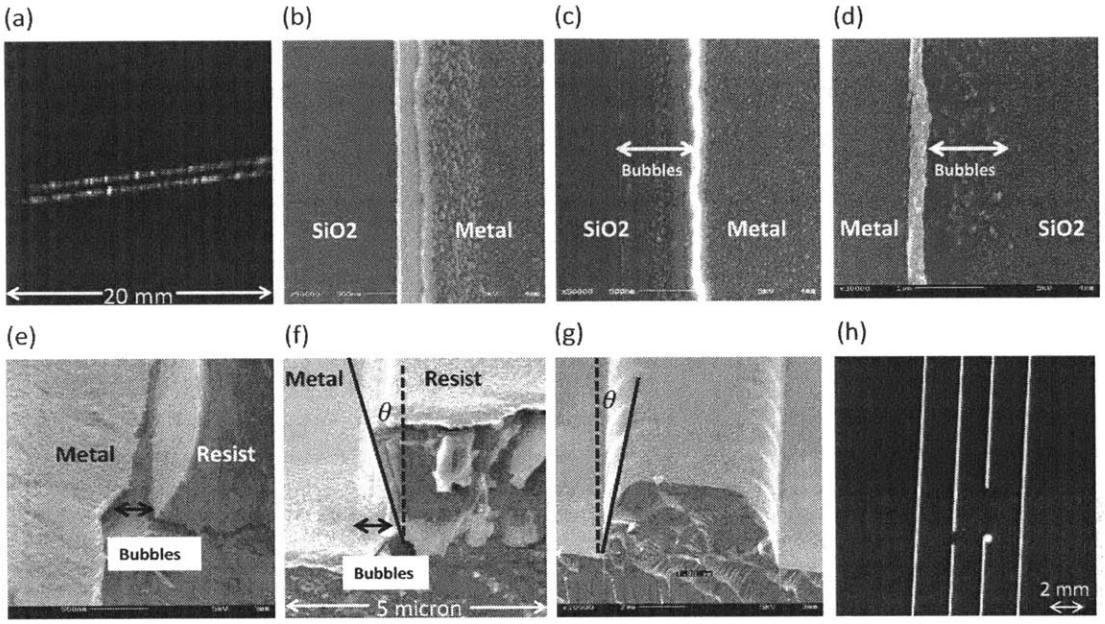

Figure 4-6: Trap RF breakdown and its correlations to bubbled metallic edges.. (a) RF breakdown observed for evaporated mirror traps with an RF signal (approx. 200 V_{pp} and 20 MHz) applied across the electrodes under vacuum, as observed with a CCD camera. (b) SEM picture of a typical electrode edge, which does not exhibit breakdown. (c) SEM picture of a typical electrode edge, which exhibited RF breakdown. Compared with (b), we found a region (500 nm width) with clusters of small metallic bubbles along the electrode edge. (d) SEM picture showing he same patterns in (c) found on samples fabricated for experiment in Ref. [HWS+11], which were tested with no breakdown characteristics. (e) SEM picture showing the metallic bubbles found near the photo-resist. (f) SEM picture showing the lift-off resist undercut and the region of observed bubbles (c.f. Fig. 4.2.1-c,d). (g) SEM picture showing resist coated by a metal layer from the lateral directions, making it difficult to lift off. (h) back side illuminated microscope image, showing a typical failed sample from lift-off with metallic coating resembling that in (g). Lightened lines are the electrode gaps.

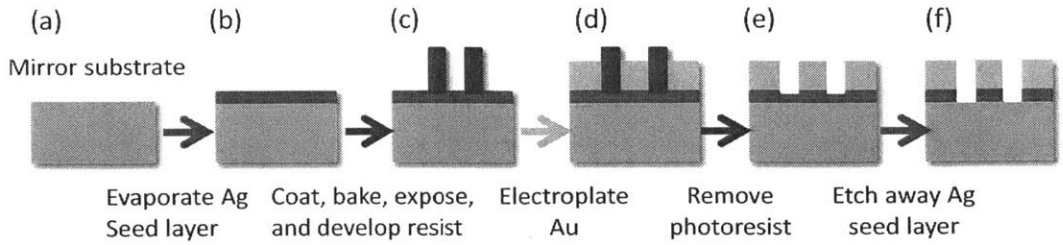

Figure 4-7: Schematic of mirror trap fabrication with electroplating. (a) a high reflectivity mirror substrate is prepared for fabrication. (b) a layer of silver seed layer is coated on the substrate. (c) photo resist is patterned on the seed layer in the lithography step, where resist remains along the trap gaps. (d) with electroplating, gold electrodes form on the seed layer following the resist pattern. (e) the photoresist is removed using solvents. (f) the silver seed layer uncovered from the resist removal is etched away with solution to which gold is inert to.

have attempted to sonicate the samples in Acetone during the lift-off process which can help with removal of the metal coating, but found it an extremely unreliable process. Figure 4.2.1-h is an example of failed samples in the lift off process, with resist patterning resembling that in Fig. 4.2.1-g. This is a backside illuminated microscope image, where the lightened lines are the electrode gaps. Ripped-off electrode edges can already be observed, where there is still metal connection across the trap gaps.

4.2.2 Electroplated trap

An alternative method for trap fabrication is to use electroplating, which is attempted after breakdowns are observed for evaporated traps in Sec. 4.2.1. The process is illustrated as in Fig. 4.2.2.

In general, this is not a preferred method, because compared to evaporation, the additional step of chemical etching adds complication to the overall process. Secondly, the plating rate is highly related to the plating solution ion concentration, which reduces as samples are fabricated, and hence makes the metal thickness hard to control. Finally, the solution purity could also change due to unexpected slow reaction between the sample and solution, via non-electrochemical process. This can

result in amorphous alloy formation and hence rough electrode surfaces, which implies higher electric field noise for trapping. Nonetheless, the major difference between electroplating and evaporation is that because no lift-off process is required, no undercut resist geometry is needed. The plated metal coating grow from the seed layer, and thus filled all gaps between the resist, which avoids the formation of bubbles.

Fabrication process

The fabrication process is developed based the method from Chapter 7 of Ref. [Cet11], and the detailed steps are listed below.

1. Sample preparation: See step 1 from evaporated trap fabrication.
2. Seed layer coating: With e-beam evaporation, coat the sample surface with 10 nm of Ti and 200 nm of Ag as seed layer for Au, both at 5Å/s.
3. Lithography:
   (a) substrate baking: See step 2-(a) from evaporated trap fabrication.
   (b) Resist coating:
      i. Center the mirror substrate on the spin coater, and adjust the speed to 1500 rpm.
      ii. Stop the spin coater. With a clean pipette, add 2 drops of AZ4620 (make sure no air bubbles) on the mirror surface from the center, and wait till the resist relaxes and covers the full surface (typically 10 s).
      iii. Spin the sample at 1500 rpm for 10 s, and gradually accelerate the speed to 3000 rpm in 5 s. Keep the sample spinning at 3500 rpm for 60 s.
   (c) Pre-baking: Bake the sample at 93°C in oven for 35 min.
   (d) Exposure:
      i. Mask alignment: See step 2-(d)-i from evaporated trap fabrication.

ii. Expose for 10 s with UV intensity 10 mW/cm^2, and wait for 30 s with no exposure. Repeat this step for three times.

(c) Development: Submerge the sample in 405MIF solution and rinse for 75 s. Quickly rinse with Tab DI water for 30 s, and blow dry (c.f. step 1-(b)-ii from evaporated trap fabrication).

(f) Sample rehydration: Place sample in air, and wait for at least 6 hours before next step.

4. Electroplating:

(a) Electrode attachment:

i. Cathode: Attach sample with wire bonds to a stainless steel electrode, which can be firmly mounted during the electroplating process, and connect the electrode to a power supply negative output.

ii. Anode: The positive output of the power supply is attached to a mesh electrode, made of Pt plated Ti.

(b) Plating solution preparation:

i. With a beaker designated for gold electroplating, pour enough Transene sulfite gold plating solution (TSG-250) so the entire sample can be submerged in the solution.

ii. Place the beaker on a hot plate compatible with magnetic stirrers, and place a magnetic stirrer in the solution.

iii. With a clean thermometer monitoring the solution temperature, heat and stabilize the solution temperature at 54 °C

iv. Submerge the mesh electrode in the solution.

v. Properly mount and submerge the sample in the solution with mirror surface down, directly above the stirrer, with approx. 1 cm space in between. Wait until the solution relaxes with no air bubbles trapped on the sample surface (typically 10 s). If air bubbles are still present, remove and re-insert sample into solution.

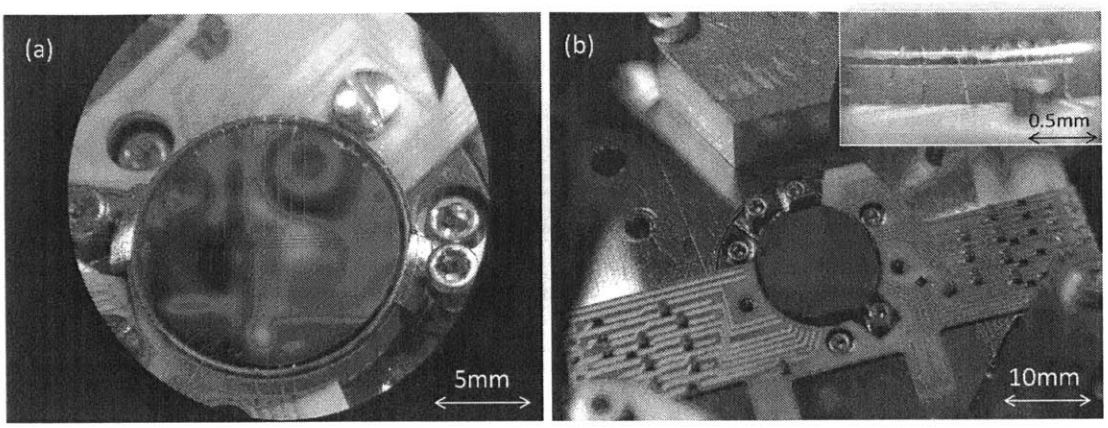

Figure 4-8: Packaged electroplated trap. (a) Microscope image showing a sample of gold electroplated mirror trap. (b) Mirror trap packaged in the mirror adapter mount, with breakout boards shown to which the trap electrodes are wire-bonded to. Inset of (b) Low profile wire bonds for laser access to ion height at 150 μm above trap surface.

(c) Plating:

i. Turn on the stirrer at speed 400 rpm.

ii. Apply a constant current of 1 mA/cm^2 to the setup (e.g. ~5 mA with 5 cm^2 cathode surface area, including both sample and electrodes) for 35 min. The expected plated Au thickness is 1.4 μm.

(d) Rinse: Quickly rinse with tap DI water for 30 s, and blow dry (c.f. step 1-(b)-ii from Evaporated trap fabrication)

5. Resist removal: See step 4 from evaporated trap fabrication.

6. Seed layer etching: Soak in silver etchant (NH_4OH:H_2O_2:DI = 1:1:4) for 20 s.

7. Post processing: See step 5 from evaporated trap fabrication.

RF breakdown tests

The tested breakdown voltage for electroplated samples have typical breakdown voltages of 800V$_{pp}$, and for the one installed, we tested up to 600V$_{pp}$ without observing

a breakdown point.

Packaging

The packaged trap is shown in Fig. 4.2.2-a, mounted in the trap adapter (c.f. Fig. 4.1.3). In Fig. 4.2.2-b, the trap printed circuit board (PCB) is shown, to which the trap electrodes are wire-bonded (Westbond 7476D). Aluminum wire bonds are used, and the parameters used for reliable bonding are power = 300, time = 30 ms.

Because in our design, the trap surface is higher than the breakout boards, wire bonding can be challenging due to the high bond strain on the latter. The temperature cycle over the UHV chamber baking process can thus cause the bond to break. Extending the wire length can relax the bond strain, but at the same time result in higher wire profiles above the trap surface, which can be undesired for laser access (recall the ion height is 150 μm). The low profile wire bonds are shown in the inset of Fig. 4.2.2-b. We have tested the wire bond strength at the machine setting used through 4 temperature cycles (room temperature to 250 °C) with spare traps, and proved the bonds to be reliable.

4.3 Laser-machined micro-mirrors

For mirrors used for high finesse optical cavities, surface polishing prior to coating processes is crucial, as the the scattering loss scales exponentially with surface roughness σ_{rms}, as

$$\mathcal{L} \sim 1 - \exp\left(-\frac{\sigma_{rms}^2}{\lambda^2}\right), \tag{4.5}$$

where λ is the wavelength used. Commercial high reflectivity mirrors rely on chemical polishing processes, which due to the tool size, cannot produce mirrors with ROC less than a few millimeters.

One approach to obtain small-ROC mirrors is to use high-power laser melting [HSC+10]. When melted by a high-power laser pulse, an approximate spherical surface on the fused silica substrate can be formed. We adopt this technique to

fabricate the micro-mirrors used for our experiment. The fabrication process and characterization results are shown below.

4.3.1 Fabrication

The fabrication process is listed below:

1. Substrate cleaning: Fused silica substrate from Edmund optics (Part No. 48201) are used for fabrication. The samples are cleaned with Piranha solution (see step 5 from evaporated trap fabrication in Sec. 4.2.1).

2. Laser machining: A CO_2 laser (Synrad 48-1) in square wave mode is focused on the substrate, with a waist of 2.8 mm and power of 26 W. The laser pulse duration is fixed at 50 μs, and to control the total power and hence the mirror curvature, the pulse frequency is varied. A total number of 5 pulses are used.

3. Post cleaning: Samples are cleaned in Piranha again before shipping to ATF for coating (see step 1).

4.3.2 Characterization

Radius of curvature

The ROC of a curve $y(x)$ whose second derivative exists is defined as

$$ROC = \left[1 + \left(\frac{dy}{dx}\right)^2\right]^{3/2} \left(\frac{d^2y}{dx^2}\right)^{-1}. \tag{4.6}$$

For laser machined mirrors, the cross-section profiles can be fitted with a Guassian profile, as

$$y(x) = A \exp\left[-\frac{(x - x_0)^2}{2w^2}\right] + B, \quad ROC = \frac{w^2}{A} \tag{4.7}$$

We fit a number of mirror profiles obtained using profilometer measurements, and obtain a rough calibration for mirror ROC as a function of pulse frequency in Fig. 4.3.1-b.

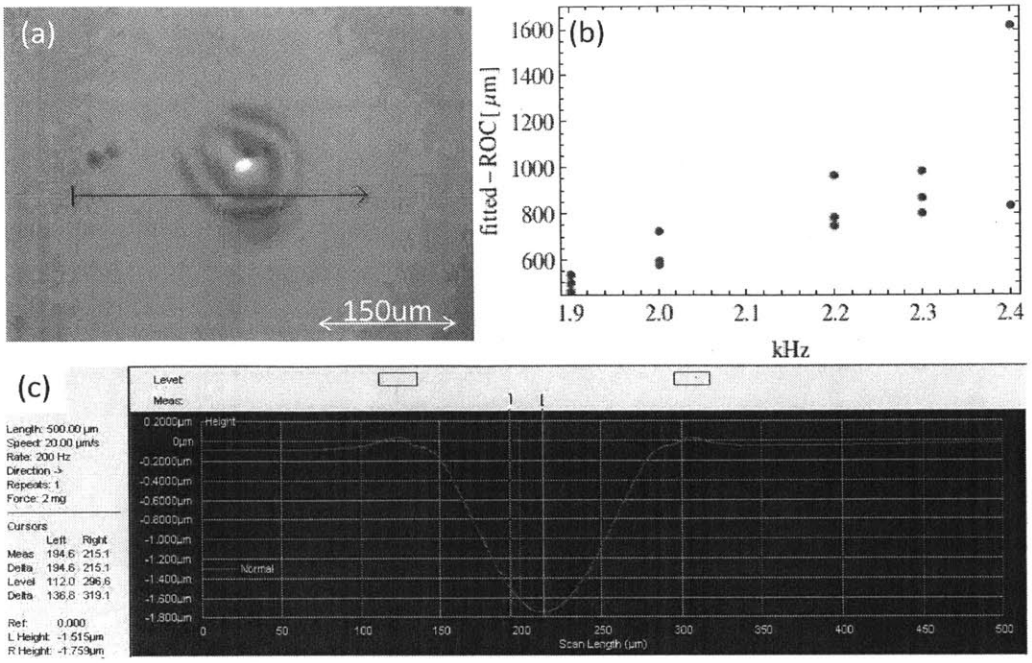

Figure 4-9: Micro-mirror fabricated using laser melting. (a) microscope image of a micro-mirror. The arrow shows the direction along which a profile measurement is taken. Due to the camera and profiometer needle misalignment, the the cross section is off-set to capture the deepest profile of the sample. (b) A calibration curve is given for ROC as a function of pulse frequency (c) A typical priflometer measurement result for mirror ROC characterization.

We can see that although the ROC in general increases with the pulse frequency, the reproducibility can be quite unreliable. Also, there can be quite large an ellipticity for the micro-mirrors. For instance, while the the fitting in Fig. 4.3.1-c results in $ROC = 898$ μm, the measurement in the orthogonal direction gives $ROC = 689$ μm. At this moment, we do not know the exact reason.

Loss

To obtain a good mirror coating on micro-mirrors can be challenging, since the low ROC can cause the coating layer strain to be different from that on the flat surface, and hence different indices of refraction. Therefore the coating design optimized for a certain frequency at large or infinite ROC can be quite different in the case for micro-mirrors.

We characterize the mirrors coated at ATF in a Fabry-Pérot cavity formed with a micro-mirror and a flat, well characterized commercial mirror mounted on a pzt. The

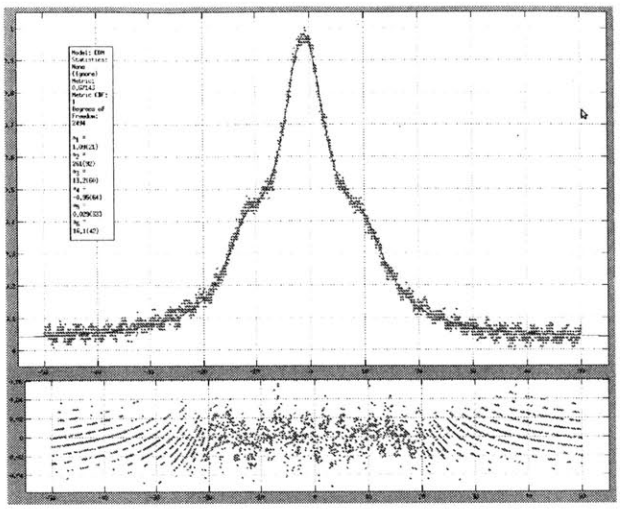

Figure 4-10: A typical transmission through the Fabry-Perot cavity formed with a micro-mirror and a flat, well characterized commercial mirror from ATF. The cavity length is scanned during the measurement, and the incident laser frequency is modulated with an EOM. Cavity loss can be obtained by fitting the obtained transmission curve with Eq. 4.8. Shown also, is the residual plot for this fitting.

direct Lorentzian mapping method is used (See Appendix A, with the cavity length scanned. With the frequency modulated by an electro-optical modulator (EOM), the cavity transmission signal follows [Bla01]

$$\mathcal{T} = A\left[\left|\frac{1}{1-\mathcal{R}_1\exp(2i\phi_0)}\right|^2 + \left|\frac{i\beta V/2}{1-\mathcal{R}_1\exp(2i\phi_+)}\right|^2 + \left|\frac{i\beta V/2}{1-\mathcal{R}_1\exp(2i\phi_-)}\right|^2\right] + B, \tag{4.8}$$

where β is the modulation depth. $\mathcal{R}_1 = 1 - \mathcal{T}_1 - \mathcal{L}/2$ is the single mirror loss, with $\mathcal{T}_1$ the nominal single mirror transmission by design, which we take as $\mathcal{T}_1 = 45$ ppm. The phase factors follow

$$\phi_0 = \frac{2\pi}{\lambda}v(t-t_0), \quad \phi_\pm = \phi_0 \pm \frac{\Omega_{mod}}{c}L, \tag{4.9}$$

where v is the cavity scanning speed. L is the cavity length, and Ω_{mod} is the modulation frequency. A typical transmission curve is shown in Fig., in which the loss is fitted using the above equations with free parameter v, $\mathcal{L}$, A, t_0, B and β. In this particular example, the cavity length is measured at $L = 0.5$ mm, and the modulation

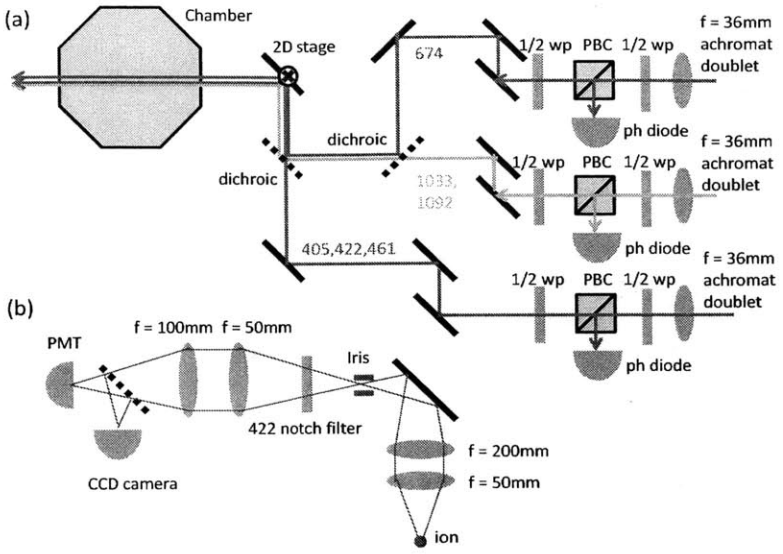

Figure 4-11: Schematic of the laser delivery and imaging optics setup. (a) laser delivery setup for ion trapping (See Fig. 3.4.1 for $^{88}Sr^{+}$ level structure). (b) imaging optics outside the chamber.

voltage and frequency used are $V = 62.5$ V, and $\Omega_{mod} = 17.3$ MHz.

The measured loss varies significantly from sample to sample, but are typically in the range of 100-300 ppm, compared with a nominal 50 ppm absorption/scattering from two commercial flat or large ROC mirrors. In this particular example, the measured loss is 264(10) ppm, where the error comes from measurement statistics with typically 10 measurements for each mirror. We attempted to clean the mirror in piranha solution and compare the loss measurement before and after cleaning. The result show no improvements, but does not lead to a conclusive indication on the loss mechanisms, which can be from either rougher surface or transmission variation from the design.

4.4 System and trapping demonstration

In this section, we present two preliminary results for the experiment. Mirror scattering loss before and after oven loading is characterized in both the loading and cavity region, as a verification of the trap design against oven flux contamination. Stable

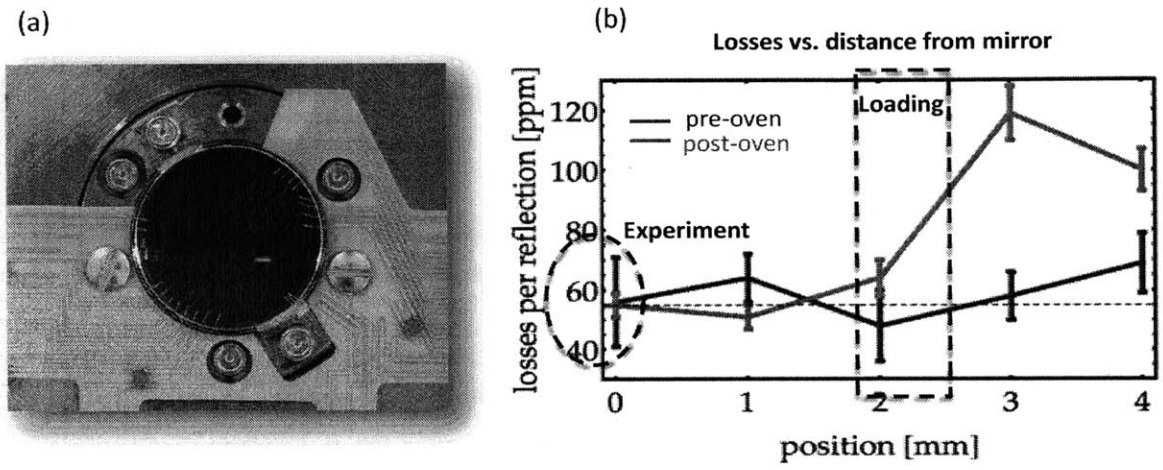

Figure 4-12: Scattering loss increase characterization over oven loading. (a) scattered photons from photo-ionization laser (461 nm) intersecting oven flux. To characterize the scattering loss increase due to oven flux contamination, a high reflectivity mirror is installed in place of the trap shown. Scattering loss before and after oven loading is measured at several spots along the trap axis. (b) mirror scattering loss comparison between cavity and loading zone, before and after running oven flux.

As a first demonstration of the electroplated trap, we install the trap in the vacuum chamber without the upper mirror, and perform a trapping experiment. A schematic of the laser delivery and imaging system setup is shown in Fig. 4.4-a. All lasers are delivered to the experiment using optical fibers, including the ionization (461, 405 nm), cooling (422 nm), repumping (1092, 1033 nm) and qubit addressing (674 nm) beams. The frequency control opto-electronics are set up before fiber delivery, which are not shown. The blue (405, 461, 422 nm) and IR lasers (1033, 1092 nm) are pre-combined, respectively before fiber delivery. The setups for combining the blue and IR lasers are not shown. Using polarization-dependent beam-splitting cubes (PBC), fractions of the delivered laser power is sent to photo-diodes for intensity monitoring, with the ratio adjusted by the half wavelength wave plates. The polarization relative

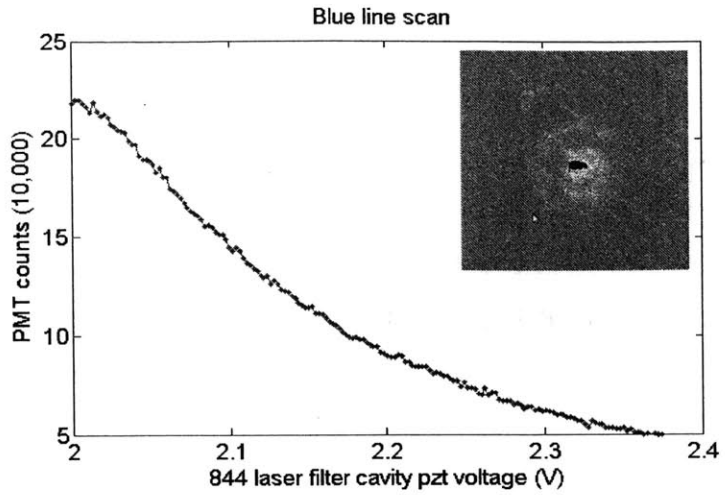

Figure 4-13: Doppler scattering spectrum of a stably trapped ion. The pzt voltage on the filtering cavity of the 844 nm laser (x-axis) is used to control the frequency detuning of the Doppler laser. The scattering intensity is measured by the PMT photon counts shown on the y-axis. A CCD camera image of the trapped ion is shown in the inset.

to the ion quantization axis (defined by the magnetic field) is adjusted by another half-wavelength wave plate after the PBC. All ionization, cooling, repumping and qubit addressing beams are combined using dichroic mirrors. The combined beams are aligned with the ion position with a motor controlled 2D stage (See Fig. 4.1.3-a for beam position relative to trap in chamber). Because the tripod and upper mirrors are not installed for this part of the experiment, we can image the ion from the top window of the vacuum chamber, and the schematic is shown in Fig. 4.4-b.

Prior to trapping, we have installed a high-reflectivity mirror (same batch from which the mirror substrate is used) in place of the mirror trap (see Fig. 4.4-a). This mirror is characterized before installation along the trap axis direction for scattering loss in a Fabry-Pérot cavity using ring-down spectroscopy. After installation, the thermal oven with Sr metal is run at high current (7 A, compared to 3 A for typical loading setting) for approx. 4 hours, after which the scattering loss is characterized again, at the same points as prior to installation. As shown in Fig. 4.4-b while an increase of $\sim$60 ppm of loss is observed near the loading region, no significant loss increase is found at the cavity region.

We have also successfully demonstrated stable trapping in this system. With

Doppler cooling (422 nm and 1092 nm for repumping), we have observed an ion life time for over 12 hours. In Fig. 4.4, a typical single-ion Doppler scattering spectrum is shown. Shown on the x-axis, the frequency detuning is represented by the PZT voltage on the filtering cavity of the 844 nm laser [Lab08], which is then frequency-doubled to the 422 nm Doppler cooling laser via second harmonic generation. In such lasers, the filtering cavity provides optical feed back to the laser diode, and hence controls the laser frequency. The PMT counts, representing the scattered light intensity is plotted on the y-axis. In the inset of the figure, is the image of the single ion captured by the CCD camera. The curve shows only the red-detuned part of the Doppler scattering profile, as the the blue detuned Doppler laser can cause the ion to heat up and escape from the trap.

4.5 Conclusions and discussion

In this chapter, we have presented a novel design of an integrated cavity trap system, in which demonstration of single ion cavity QED can be feasible. The system uses a short stable cavity, with low ROC cavity mirrors obtained from laser machined micro-mirrors. The ion-cavity-mode alignment complexity is greatly reduced if the trap electrodes are directly fabricated on a flat, high reflectivity mirror, with a central aperture through which a cavity mode forms.

To avoid alignment shifts due to thermal cycling, a room temperature vacuum enclosure is designed for the cavity ion system. In addition, the trap fabrication techniques optimized for cryogenic systems, using e-beam evaporation is found incompatible with the room temperature setup. Discharging events are found when high voltage RF signals are applied across trap electrodes, implying low breakdown voltages. We discovered that the breakdown events are highly correlated with the directionality of the metal deposition during the evaporation process. New fabrication processes are thus developed using electroplating, which exhibit high breakdown voltages.

To avoid oven flux contamination to the cavity mirrors, a segmented trap design is adopted, which allows the ion to be trapped in the flux region, and shuttled to the flux-free cavity region for experiment.

Furthermore, we have fabricated the low ROC mirrors using laser machining, and characterized both the geometric and loss profile. Unfortunately, although the additional loss of some mirrors can still result in high finesse cavity for strong coupling experiment, the low geometric profile reproducibility and large loss variation is found for the mirror laser machining process. Nonetheless, mirrors desired for experiments can still be found via post-selection.

As a demonstration of the system design, we have characterized the optical quality of the trap aperture region vs the flux region for loading, before and after running the oven. The result shows a strong signature of scattering loss increase due to the oven flux. Stable trapping of a single ion is also shown, as a demonstration of trap fabrication reliability.

Chapter 5

Cavity finesse degradation and recovery in HV systems

High finesse cavities have been an integral part of experimental AMO physics. Their narrow linewidth provides stable frequency references for photon sources [KHG+12], and the intra-cavity field enhancement is essential for strong coupling between photons and quantum systems [CBK+13, SLM+12]. For instance in Chapter 4, we have discussed the key role of maintaining the high mirror reflectivity during the fabrication processes for mirror-integrated traps, in order to achieve strong ion-photon coupling in a high finesse cavity. To achieve the reflectivities needed for high finesse cavity applications, the mirrors used are predominantly fabricated as dielectric stack structures of tantalum (V) oxide (Ta_2O_5) and silicon (II) oxide (SiO_2) [Sit83, RTKL92], where the vacuum-facing layer is typically Ta_2O_5 which has a higher index of refraction. However, it has been observed that for this type of mirror, absorption losses increase dramatically over time under vacuum [Cet11, CBK+13, SLM+12], causing the finesse of these cavities to decay to unacceptable levels. When the temperature is raised to conditions necessary for mirror annealing under vacuum [BMS+13], it was observed at infrared wavelengths that this loss increase is accompanied by a oxygen concentration reduction on the Ta_2O_5 surface layer of the mirror. This observed oxygen depletion then suggests a degradation model based on material transformation in the surface

layer.

In this section, we present a systematic study on the degradation of high finesse cavities in high vacuum systems. We hypothesize that the vacuum induced optical loss increase is due to oxygen vacancy formation on the mirror surface, and thus can be reversed by re-oxidation. In Section 5.1, we describe a model for the time dependence of mirror optical loss. In Section 5.2, we outline the experiment design, where the dependence of loss increase rate on temperature, wavelength, and surface layer configuration are investigated. The results are shown in Section 5.3. In Section 5.4, we investigate methods to prevent Ta_2O_5 surface degradation by passivating it with SiO_2. The chapter is concluded with a summary in Section 5.5

5.1 Model

Although optical loss increase in high finesse cavities has been observed in several experiments [Cet11, CBK+13, SLM+12], it is not until recently that the correlation between the loss increase and oxygen depletion on the mirror surface was investigated[1] [BMS+13], At the surface, the oxygen bound as an oxide can form free radicals, or water via a redox reaction mediated by hydrogen ions, and is then quickly diffused out in vacuum making the reverse process highly improbable. During the oxygen depletion processes, oxygen vacancies form, creating color centers in the surface layer dielectric, which are optically absorptive [DSG85]. To model the time dependence of cavity optical loss, we consider a typical high reflectivity mirror, composed of alternating Ta_2O_5 and SiO_2 dielectrics, and a Ta_2O_5 surface layer. We denote the unitless surface color center density $\theta \equiv \theta(t)$, as the mole ratio between color centers and free oxygen radicals. Because the absorptive mechanism is incoherent, the total optical loss induced the color centers should be proportional in θ, resulting in

$$\mathcal{L} = \mathcal{L}(0) + \Delta\mathcal{L}\theta, \tag{5.1}$$

[1] Although the temperature range studied in Ref. [BMS+13] is higher than those used in most applications, optical losses resulting from oxygen depletion in Ta_2O_5 have been reported to be far more severe at shorter wavelengths [DSG85], for which our experiment is designed (See Section 3.4).

where the proportionality constant $\Delta\mathcal{L}$ has the same unit as $\mathcal{L}$. We use a first order model for the redox reaction, such that the formation rate of the oxygen vacancies, hence the color is proportional to the amount of surface oxygen radicals. That is

$$d\theta/dt = (1-\theta)/\tau_{th}, \tag{5.2}$$

where the thermal activation time constant $\tau_{th} \equiv \tau_{th}(T)$ is a function of the mirror surface temperature T. The solution of Equation 5.2 has the form

$$\theta(t) \propto 1 - \mathrm{e}^{-t/\tau_{th}}, \tag{5.3}$$

which suggests the optical loss to increase in time as

$$\mathcal{L} = \tilde{\mathcal{L}}(0) + \Delta\tilde{\mathcal{L}}\left(1 - \mathrm{e}^{-t/\tau_{th}}\right), \tag{5.4}$$

with new constants absorbed in $\Delta\tilde{\mathcal{L}}$.

According to Arrhenius equation, at different temperatures, the thermally activated reaction rate is expected to follow

$$1/\tau_{th} = \exp(-E_a/k_B T), \tag{5.5}$$

where the constant E_a is called the activation energy, and k_B is the Boltzmann constant. For different materials, the activation energies E_a can be drastically different, resulting in different redox or re-oxidation rate during the oxygen reduction o recovery processes, respectively. Therefore, the behavior of vacuum induced loss increase can be specific to certain surface-layer coatings at temperatures of interest. Furthermore, in presence of external EM fields, the change in Gibbs free energy difference ΔG of the chemical reaction, and hence E_a required for thermal activation may be reduced. This may result in a photo-catalyzed behavior in the oxygen depletion and/or re-oxidation process.

For completeness, suboxides of Ta, and hence oxygen vacancies can also form in

redox reactions transforming suboxides of Si to SiO_2 [MSW+99], which is expected to happen between the internal layers of the mirror stack. This mechanism is highly distinct from our hypothesis in terms of the process reversibility. For the surface oxygen depletion model, a reverse process of the optical loss increase is expected when a large oxygen partial pressure is present, reoxidizing the Ta suboxides at the mirror surface. On the other hand, suboxides formed between the internal layers cannot be reoxidized because the penetration depth of oxygen is on the order of several Angstrom[Kha13]. Whereas for a typical mirror coating, each dielectric layer is expected to be several nanometers thick. Another model to account for the optical loss increase is based on spurious impurity deposition on the mirror surface, accelerated by higher temperatures, and reversed by the binding of impurities to ambient oxygen during the recovery process. Unlike our oxygen depletion hypothesis, this mechanism predicts no variation of the loss increase rate for different surface dielectric thickness. In the following sections, we show how our experiment is designed to test our hypothesis, and how other possible mechanisms are ruled out in our results.

5.2 Experiment

In this section, we describe our experiment design. The goal is to study how the cavity optical loss increase depends on temperature, wavelength and surface layer configuration. We aim to support the oxygen depletion model described in Sec. 5.1, and to find methods to reliably reverse the optical loss incurred in vacuum in-situ, which is essential in many atomic physics experiment applications involving strong coupling [CBK+13, SLM+12].

5.2.1 Experiment setups

Four different mirror coatings are tested in three separate setups. Table 5.2.1 summarizes the experiment setups and main results.

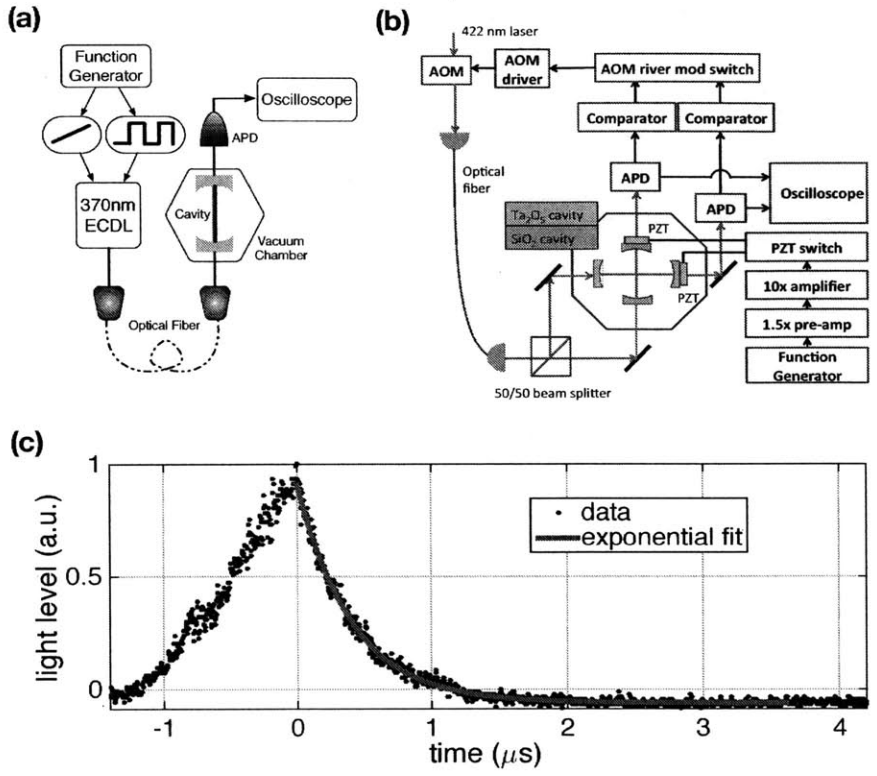

Figure 5-1: (a) Schematic of the experimental setup for chamber I. A pair of mirrors forming a high finesse cavity with either Ta_2O_5 (coating I-1) or SiO_2 (coating I-2) as their surface layer, are placed in high vacuum. Light from a single mode laser at 370 nm is used to probe the cavities as the laser frequency is slowly scanned linearly by a function generator. The transmitted light from the cavity is incident on an avalanche photodiode (APD). The laser frequency is also modulated by a fast square-wave signal, which results in an intensity free-decay of the cavity's transmitted light each time the slow scan brings the laser to resonance with the cavity (time = 0 μs). (b) Schematic of the experimental setup for chamber III. Two pairs of mirrors forming high finesse cavities with SiO_2 (coating III-2) and Ta_2O_5 (coating III-1) as their surface layer, respectively, are placed in high vacuum. Light from a single mode laser at 422 nm is used to probe the cavities as they are scanned by piezo-electric transducers (PZT). The transmitted light from each cavity is incident on an avalanche photodiode (APD). When the cavity becomes resonant with the laser, and the signal intensity reaches a defined threshold in a comparator, the laser light is switched to be off-resonant with an accousto-optic modulator (AOM) (time = 0 μs), resulting in an intensity free-decay of the cavity's transmitted light. (c) A typical intensity free-decay curve measured for 370 nm (coating I-1), fitted with an exponential model with a time constant of $\tau_c = 411$ ns.

Wavelength	370 nm			422 nm	
Coating	I-1	I-2	I-1	III-1	III-2
Top Layer	Ta_2O_5	SiO_2	Ta_2O_5	Ta_2O_5	SiO_2
Top Layer Thickness (nm)	28.3	1	28.3	48.6	110
Transmission $\mathcal{T}$ (ppm)	180	180	180	40	45
Chamber	I		II	III	
Pressure (Pa)	7×10^{-6}		10^{-8}	7×10^{-5}	
Cavity Length $\mathcal{L}$ (cm)	5	5	2.2	4.1	2.2
Temperature (°C)	21,50,75,100,150	100	33	57	57
Mirror Loss Increase	Yes	Yes (slow)	Yes	Yes	No
Fig. Reference	5.2.2, 5.3.1, 5.3.1	5.4	5.2.2, 5.3.1	5.3.2,5.4	5.4

Table 5.1: Summary of experimental parameters and results.

Mirror coatings

Four sets of mirror coatings are tested in the experiment, which we denote I-1, I-2, III-1 and III-2. The index I and III denote the test chambers used, which are described later in this section. All four coatings are SiO_2:Ta_2O_5 dielectric stack structures (deposited by Advanced Thin Films (ATF) in Boulder, CO), with factory nominal scattering loss of 25 ppm per mirror due to surface roughness imperfection. coating I-1 (ATF coating run V4-764) has a Ta_2O_5 surface layer, and its reflectance spectrum is centered at around 370 nm with a transmittance of 180 ppm. To evaluate whether the rapid loss increase is specific to mirrors with Ta_2O_5 surface layers, a thin layer of SiO_2 (1 nm) is sputtered on two mirrors with coating I-1, which we index as coating I-2. The sputtering process was completed at MIT EML, with the Orion 5 confocal sputtering system from AJA International Inc.. The relevant setting is summarized in Table 5.2.1. Although not re-calibrated after deposition, we expect the transmittance to be unchanged due to the addition of the SiO_2 layer. To investigate the sensitivity of loss increase rate to wavelength variations, coating III-1 (ATF coating run V4-1248) and III-2 (ATF coating run V2-1260) are tested, which have the reflectance spectrum centered at around 422 nm, with transmittance of 40 ppm and 45 ppm, respectively. The surface layers of III-1 and III-2 are Ta_2O_5 and SiO_2, respectively. Unlike I-2, the SiO_2 surface layer for III-2 is thicker (10 nm), and was coated during the same fabrication process at ATF, which underwent an annealing process for crystallization.

Comparing the behavior of I-2 and III-2, we should gain insights into how sensitive the reduced/prevented oxygen depletion is to the thickness of the added SiO_2 phase and thickness.

Parameter	Setting
Chamber pressure	10^{-4} torr
Growth rate	0.38 nm/min
Argon flow	3 mtorr
Substrate temperature	125 C

Table 5.2: Summary of experiment settings for sputtering process.

HV systems and cavity configuration

Three separate experiment setups were used to test the different mirror coatings. In each chamber, high finesse Fabry-Perot cavities formed by the mirrors were installed and tested, at a specific temperature setting. The chambers labeled I, II, and III are described below:

- I: dedicated for cavity loss measurement for coatings I-1 and I-2 at 370 nm at different temperature settings (See Fig. 5.2-a). The pressure is maintained at 7×10^{-6} Pa with a Turbo pump, and the temperature is varied by heating the chamber and monitored using an external probe.

- II: atomic physics chamber with a cavity formed with mirrors of coating I-1 [Cet11]. The pressure is maintained at 10^{-8} Pa, and the temperature is actively stabilized at to 33 °C by measuring the temperature close to the mirror mount. Mirror loss increase was first observed in this chamber, which inspired this systematic investigation performed in Chamber I and III. One time dependence trace of mirror at 33 °C is obtained in this setup.

- III: dedicated to test coating III-1 and III-3 simultaneously at 422 nm. Two cavities can be installed in this chamber with separated optical paths, which

enables comparison of two coatings under the same vacuum setting (See Fig. 5.2-b). The chamber is heated and actively stabilized to 57 °C by measuring the temperature close to the mirror mount, and the pressure is maintained at approximately 7×10^{-5} Pa with a turbo-molecular pump.

For each test of mirror coating in all chambers, the mirrors are cleaned following the standard cleaning procedure outlined in Sec. 4.2.1[2]. After the cavity is installed at room temperature, the chamber is heated up to a specified temperature, and let thermalize thoroughly before the time dependence of mirror loss measurements begin. This way, systematic errors due to thermal cavity alignment change and non-uniform mirror surface scattering loss can be minimized during the experiment.

To investigate the reversal of oxygen depletion process, Chamber I and III both incorporate a needle leak valve to let in oxygen flux.

Lasers

Two ECDL lasers at 422 nm and 370 nm are used in the experiment to probe the cavities, which are used for Sr^+ and Yb^+ ion Doppler transitions (See Chapter 4, and Appendix B in Ref. [Cet11] for reference, respectively).

5.2.2 Method of finesse decay measurement

In all our experiments, we characterize the scattering loss $\mathcal{L}$ of the mirror coatings using the cavity free decay spectroscopy. A detailed discussion of this approach is presented in Appendix A. In a stable cavity configuration, the transmission signal $I(t)$ through the cavity follows an exponential decay in time, after the incident laser is switched off:

$$I(t) = I_0 e^{-t/\tau_c}, \tag{5.6}$$

[2] The two mirrors with III-2 coating were treated differently. Because they were used in a separate experiment before, showing a noticeable finesse drop, we suspected that the mirror surfaces were contaminated, due to possible degassing out of the ion pump during baking, These mirror surfaces were found not cleanable with methods from Sec. 4.2.1, and were thus cleaned in Piranha solution (See Sec. 4.2.1 for procedure), which fully recovered original optical quality according to the factory specs

where I_0 is the field intensity measured at the incidence of switching, and the time constant τ_c is related to the cavity scattering loss via

$$\tau_c = \frac{L}{c\pi}\mathcal{F} = \frac{2L/c}{\mathcal{T}_1 + \mathcal{T}_2 + \mathcal{L}_1 + \mathcal{L}_2}. \tag{5.7}$$

In our experiments, since two mirrors with identical coatings are used to form the testing cavities, we obtain the average single mirror scattering loss from Eq. 5.7 as

$$\mathcal{L} = \frac{\mathcal{L}_1 + \mathcal{L}_2}{2} = \frac{L}{c\tau_c} - \bar{\mathcal{T}}, \tag{5.8}$$

where $\bar{\mathcal{T}} \equiv (\mathcal{T}_1 + \mathcal{T}_2)/2$, which we take as the ATF nominal single mirror transmission coefficient in the calculations. Although this is an approximation which assumes uniformity of manufacturing, this assumption does not affect the time-dependence and temperature-dependence of the measured loss increase which we probe.

The transmission intensity is measured with avalanche photodiodes (Thorlabs APD120A2) whose bandwidths of ~50 MHz are sufficient to capture signals changing much faster than τ_c. The input light switching is done in two different ways for cavities in chambers I and II, and chamber III. For cavities in chambers I (see Fig. 5.2a) and II, the frequency of the ECDL is scanned across the modes of the cavity. Simultaneously, a square-wave current modulation is applied to the laser diode causing it to switch frequency at a rate larger than the scan rate but less than the cavity linewidth, and by an amount much larger than the linewidth of the cavity. When the laser is scanned over the cavity resonance, the rise in intracavity intensity is interrupted by the laser's frequency switching, resulting in a free-decay curve. This can be detected by triggering an oscilloscope on the down slope of the cavity's transmission intensity signal. For chamber III (see Fig. 5.2b), the cavity length and hence the cavity resonant frequency is scanned with a piezo electric transducer (PZT) mounted at the back of a cavity mirror. Laser light input into the cavity is shut off with an accousto-optic modulator after one cavity mode is on resonance with the frequency of the incident laser light; this occurs when the transmitted light intensity is detected to

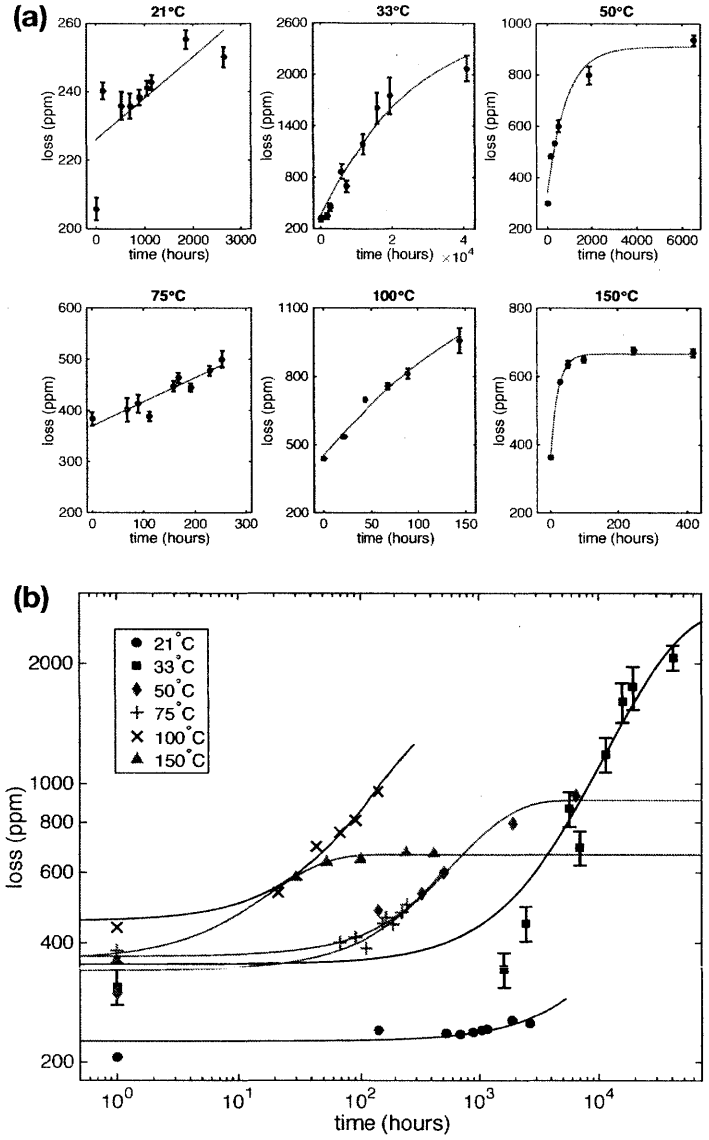

Figure 5-2: (Coating I-1) Loss increase over time at various temperatures, as separate panels on a linear scale (a) and combined on a log-log scale (b): 21°C, 50°C, 75°C, 100°C, 150°C (chamber I); and 33°C (chamber II) The observation time range is different for each temperature data set, ranging from a few days (100°C) to a few years (33°C). Each data set is fitted with an exponential model shown as a solid line (a, b), weighted by the inverse variances of the data points. The exponential time scale is very sensitive to temperature. Error bars are statistical and correspond to one standard deviation (smaller than the size of the data symbol when not shown).

reach a predefined threshold. Because spurrious triggering events can occur, only decay curves which have their maximum intensity value coincide with an edge from the pulse drive are post-selected, and fitted with an exponential model with a decay time τ_c. An example of the free-decay curves is shown in Fig. 5.2b.

5.3 Results

5.3.1 Loss increase

In this section, we present our results on the time-dependence of the vacuum-induced losses, and we also investigate the rate of the increase in losses as a function of temperature and light wavelength.

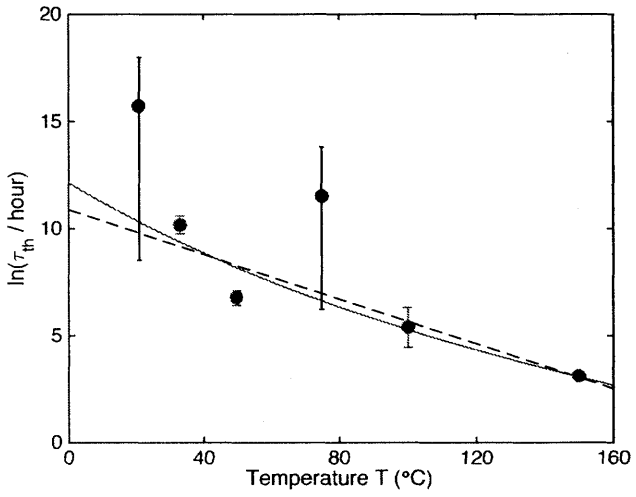

Figure 5-3: (Coating I-1) Logarithm of loss increase time scale, from an exponential fit (Fig. 5.2.2), against temperature. We fit $\ln(\tau_{th})$ with a model of the form $a/(273+T)+b$ to all data points (red solid line); the fitted values are $a = 7000(1500)$K and $b = -13(4)$. We also fit $\ln(\tau_{th})$ with a linear model (black dashed line) and obtain a negative slope of $1/e$ per 19(5)°C. The fits are weighted by the inverse variances of the data points. Brackets and error bars indicate a 68% confidence interval on the fitted values.

Temperature dependence

Fig. 5.2.2a shows the mirror losses as a function of time for different temperatures. Each data point is obtained by fitting the the free decay curve of the cavity transmission signal[3]. (See Sec. 5.2.2) The temperature of the chamber is varied from 21°C to 150°C in chamber I, and kept at 33°C for chamber II. In all experiments, we observe an increase in loss over time. The loss initially increases linearly in time, and for data sets taken over sufficiently long times we observe that the loss saturates. We find that the typical time scale for the loss to increase, and to reach saturation, sharply decreases with temperature. At 21°C, the loss increases by only 20% after 12 weeks, while at 150°C, the loss saturates at about twice its initial value after just 3 days. The data is fitted using Eq. 5.4, from which the time scale of the loss increase τ_{th} is obtained.

Fig 5.3.1b shows the logarithm of this time scale, $\ln(\tau_{th})$, against temperature T, and a fit to a model inversely proportional to T. This relationship is highly suggestive of an Arrhenius-type thermal activation predicted in Eq. 5.5. We find the activation energy $U/k_B = 7000(1500)$K (68% confidence interval). We also show a second fit, linear in T, with a fitted slope of e higher degradation rate for every 19(5)°C increase in mirror temperature.

We note that the loss saturation level $\mathcal{L}(0) + \Delta\mathcal{L}$ also appears to depend inversely on temperature. The data sets for which a saturation is observed (see Fig. 5.2.2: 33°C, 50°C, and 150°C in) suggest that higher temperatures lead to lower loss saturation levels. This may be a result of a temperature-induced shift in the light absorption spectrum of the color centers responsible for the loss increase.

Wavelength dependence

In Fig. 5.3.1, we investigate the loss increase on mirrors using coating III-1 with light at 422 nm (chamber III). The measured time scale of the loss increase at 57°C is much

[3] The last four loss values measured for coating I-1 at 33°C are obtained by measuring the cavity $FWHM$ via direct spectrum scanning (See Appendix A). The $FWHM > 1$ MHz is measured using a frequency-doubled titanium-sapphire laser whose linewidth is less than 100 kHz.

shorter than that using 370 nm light on coating I-1 at comparable temperatures. This indicates a dependence of the loss on wavelength as well as temperature.

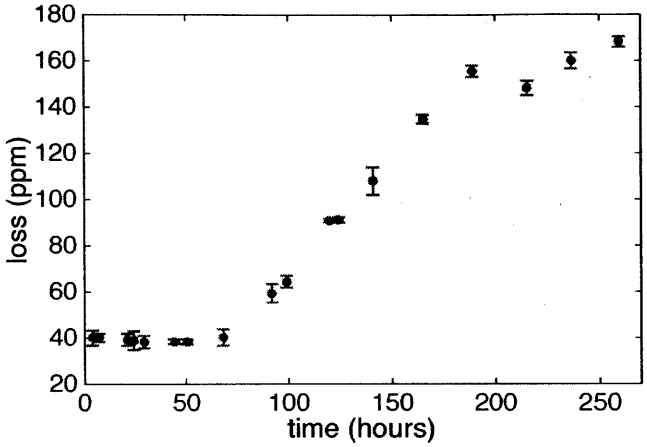

Figure 5-4: Optical loss increase observed in chamber III for an optical cavity composed of mirrors with coating III-1 (422 nm, Ta_2O_5 surface layer) at 57°C. With the current data, we do not have a good explanation for the initial slow loss increase, which is observed only in this data set. It could be attributed to the thermal relaxation time of the mirror, whose temperature was monitored on the mirror mount, which is connected to the mirror via a ceramic piezo tube. Error bars are statistical and correspond to one standard deviation.

5.3.2 Recovery with Oxygen

In this section, we demonstrate that the presence of oxygen gas at the mirror surface can reverse the losses measured in Chamber I in the previous section.

Reversal of the vacuum-induced loss is achieved by leaking high purity oxygen (Airgas Ultrahigh Purity Grade 4.4) into the Chamber I and III via the needle valve, and monitoring loss for various partial pressures of oxygen and temperatures. In all cases tested, we observe partial or full recovery from the vacuum-induced loss. This is further evidence that oxygen concentration at the mirror surface is a determining component of the degradation process.

After taking the data set at 21°C from Fig. 5.2.2, we leaked oxygen into the chamber. At the partial pressure of oxygen of 10^{-2} Pa we observed a slight recovery

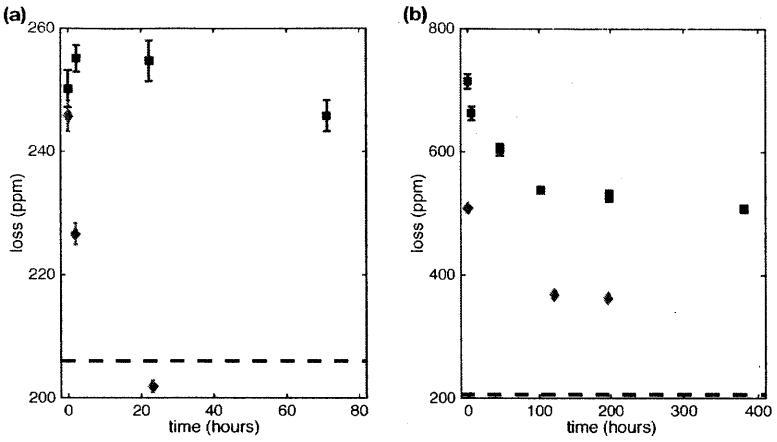

Figure 5-5: (Coating I-1) (a) Recovery with oxygen at 21°C, following the data set at 21°C (Fig. 5.2.2). Oxygen at a partial pressure of 10^{-2} Pa gives a barely statistically significant recovery (blue squares), while the atmospheric pressure of oxygen (red diamonds) gives full recovery to initial loss level (dashed line). (b) Recovery with atmospheric pressure of oxygen at 21°C (blue squares) and 150°C (red diamonds), following a loss increase at a much higher temperature of 150°C (data not shown). The recovery is slower and does not reach the initial loss level (dashed line). Error bars are statistical and correspond to one standard deviation.

from the vacuum-induced loss (Fig. 5.3.1a). Upon filling the chamber with oxygen at the atmospheric pressure, the loss fully recovers its value measured before vacuum. This recovery took approximately 10 hours, as shown in Fig. 5.3.1a. Following a separate experimental run, for which the data was taken at a much higher temperature of approximately 150°C, we observe only a partial recovery under atmosphere pressure of oxygen at 21°C, as shown in Fig. 5.3.1b. This recovery took a much longer time (several days), compared to the recovery shown in Fig. 5.3.1a following the data set at 21°C. Increasing the chamber temperature to 150°C yields a further, but still partial, recovery. It is unclear from this data set whether the high temperature loss increase is activated by additional processes, such as surface contaminants, which prevent the full recovery with ambient oxygen gas, or whether the deeper oxygen depletion at high temperatures (such as in Fig. 5.2.2, 150°C) creates an additional energy barrier to oxygen re-entering the top layer of the coating (i.e. the oxygen binding process could be hysteretic).

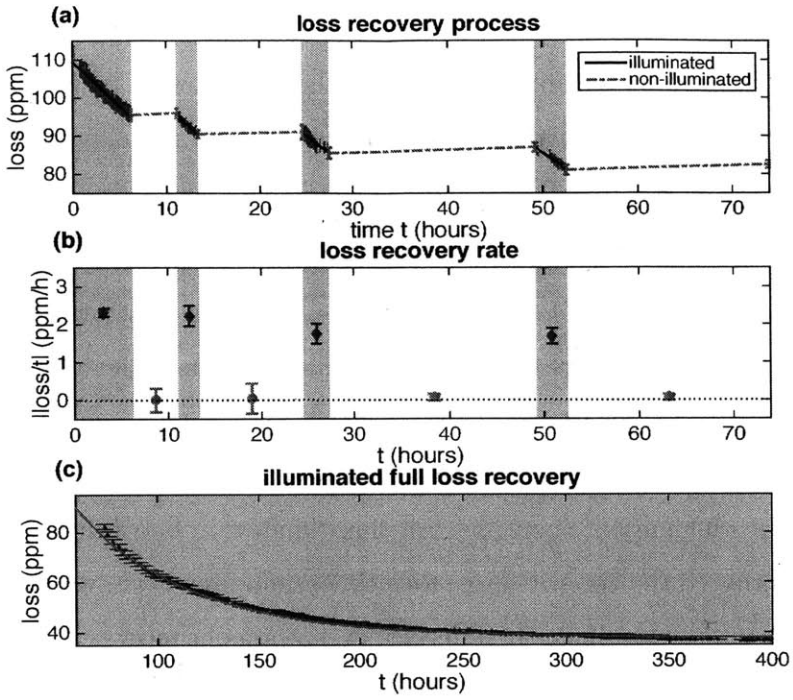

Figure 5-6: (Coating III-1) Laser-assisted loss recovery processes observed in chamber III. (a) loss recovery process examined during both illuminated and non-illuminated periods. (b) recovery rate obtained by fitting data in (a) using a linear model, and compared for both the illuminated and non-illuminated periods. (c) optical loss fully reversed in a continuous illumination process. We fit an exponential model and find the time constant to be 56.5 hrs. Error bars are statistical and correspond to one standard deviation.

5.3.3 Photocatalyzed recovery process

In this section, we show that continuous illumination of the mirrors with near-UV light can dramatically accelerate the recovery rate under oxygen.

The reversal of vacuum-induced losses by the presence of oxygen in Sec. 5.3.2 suggests that a re-oxidation process of the mirror surface oxide might be involved. Studies of the dielectric thin film growth process indicate that the oxidation rate can be significantly affected by the presence of UV light illumination [ZBDB98, BZ01], especially for Ta_2O_5, for which improvement of the optical properties was found during a UV annealing stage. It was observed that under 172 nm radiation, oxygen can be easily dissociated to form stronger oxidizers, such as ozone or single O atoms, which

can further oxidize defects, e.g. suboxides of Ta, to increase the material transparency. In light of this, we examined in our setup whether recovery from vacuum-induced losses can be affected by illuminating the cavity with the resonant probe laser at 422 nm (the near UV range).

In chamber III, after the mirror loss measured for coating III-1 increased to 320 ppm, we investigated the loss reversal process in oxygen at atmospheric pressure for two controlled processes: 1) an illuminated process, where the cavity was continuously illuminated by the probe laser at 422 nm with about 10 kW/cm^2 of intra-cavity intensity; and 2) a non-illuminated process, where the same cavity was probed only twice for measurement, with a time window in between without illumination. We alternated the two processes four times, and found the two corresponding loss reversal rates to be significantly different. A 4-5 ppm/hr recovery rate during the illuminated periods was observed, whereas the rate during the non-illuminated periods was found to be negligible (See Fig. 5.3.2b). After the comparison, we continued the loss reversal process under illumination, and achieved a full recovery of the initial cavity loss level (See Fig. 5.3.2c).

The negligible rate of recovery observed here in the absence of laser light is consistent with the slow rate of recovery observed following the 150°C loss increase at 370 nm (Fig. 5.3.1b). In both cases, the more than two-fold increase in the loss factor when under vacuum could be accompanied by a higher activation energy to re-oxidation. As suggested by Eq. 5.5, this is a possible explanation for why UV light at 422 nm dramatically enhanced the rate of recovery, while a higher temperature enhanced the recovery level at 370 nm.

5.4 Surface Material Dependence and Passivation with SiO_2

In this section, we show that the loss increase is specific to a Ta_2O_5 surface layer, and that passivation with SiO_2 can strongly reduce the loss increase observed in Sec. 5.3.1.

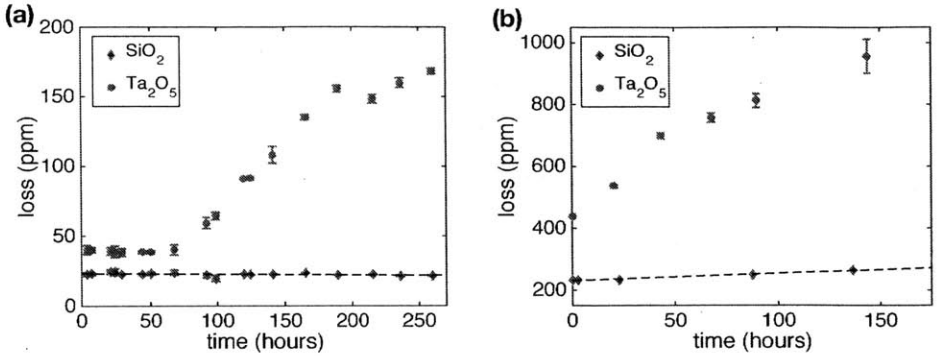

Figure 5-7: Loss vs time for different mirror top layer coating: (a) Loss increase at 57°C measured at 422 nm for top layers: Ta_2O_5, coating III-1 (red circles, data also shown in Fig. 5.3.1), and for 110 nm SiO_2, coating III-2 (blue diamonds). The dashed line is a linear fit with a slope of $-0.005(2)$ ppm/h. (b) Loss at 100°C measured at 370 nm for top layers: Ta_2O_5, coating I-1 (red circles), and for 1 nm SiO_2, coating I-2 (blue diamonds). The dashed line is a linear fit with a slope of 0.23(3) ppm/h. Error bars are statistical and correspond to one standard deviation.

Figure 5.4a shows that the mirror coating degradation processes obtained from chamber III for coatings III-1 (top layer: Ta_2O_5) and III-2 (top layer: SiO_2 110 nm) are strongly dependent on surface layer materials. At the same pressure and temperature, coating III-1 shows a significant loss increase, whereas coating III-2 shows a negligible loss increase. Since SiO_2 has a higher activation energy for oxygen vacancy formation [mis15, KAE67], this is a further indication that surface oxygen has a key role in the loss increase process.

This observed dependence of the loss increase on surface material also implies that compared to coating I-1, the 1 nm passivation layer on coating I-2 (See Sec. 5.2.1) can result in a much smaller or even negligible loss increase. Indeed, by repeating the set of loss measurements performed in chamber I at a temperature of 100°C, we observe a reduction of the degradation rate by at least an order of magnitude, as shown in Fig. 5.4b. The reduction in loss rate for a 1 nm-thick SiO_2 layer can be furthered to complete by using a 110 nm-thick SiO_2 layer as in Fig. 5.4a.

We observe that the likelihood of the oxygen reduction process strongly depends on the oxide making up the vacuum-facing surface layer. Indeed, the Gibbs free energy difference ΔG, and hence the Activation energy E_a (See Eq. 5.5) for the formation

of SiO_2 is larger than for Ta_2O_5 [mis15, KAE67]: at a temperature of 300K the oxidation Si $\rightarrow$ SiO_2 has $\Delta G \sim -850$ kJ/mol with a single intermediate oxide, while the oxidation Ta $\rightarrow$ Ta_2O_5 has $\Delta G \sim -750$ kJ/mol with four times the number of intermediate oxides. Eq. 5.5 thus predicts a faster reaction rate of oxygen reduction for the latter than the former. This dependence of the loss increase rate on surface layer thickness confirms that the loss process is due to a material transformation in the Ta_2O_5 surface layer, rather than a spurious deposition process. This observation is the strongest evidence we have for oxygen-depletion causing additional losses in the Ta_2O_5 surface layer.

5.5 Conclusions and discussion

A summary of our experimental parameters and results can be found in Table 5.2.1.

We conclude that the additional losses observed in mirror coatings placed under high vacuum are a result of a thermally-activated depletion of oxygen from the mirror's surface Ta_2O_5 layer, thereby increasing the concentration of absorbing Ta_2O_x-suboxides, leading to a time-evolution of the loss factor that likely follows an Arrhenius process. As shown in this paper, this degradation process is strongly accelerated by temperature, with a rate that likely follows an exponential dependence on $1/T$. The loss can be reversed, in full or in part depending on operating temperature, by filling the vacuum chamber with an atmosphere pressure of oxygen; and this recovery can be strongly accelerated and enhanced by the presence of UV light. Most important to future systems, the loss process can be altogether prevented by passivating the Ta_2O_5 surface layer with a thin layer of SiO_2, likely on the order of 10 nm, or by ensuring that the surface layer of the dielectric stack is SiO_2.

Part III

Molecular ion and cavity assisted microwave QLS

Chapter 6

Quantum logic spectroscopy

Trapped-ion systems are ideal platforms for the studies of high resolution spectroscopy, for the long storage time and their near-perfect isolation from environment can in principle allow experimenters to perform continuous measurements for data resolution improvement. Recent advancement in this field resulted in many applications such as the development of trapped-ion based atomic clocks [ODD+06] and techniques for real-time chemical dynamics monitoring for molecular ions [HOB+08]. For quantum information processing in particular, continued progress in high resolution qubit spectroscopy lead to the demonstration of high fidelity single and multi-qubit gates needed for fault-tolerant quantum computing [BHLL14, HAB+14]. Among all these state-of-art experiments, four key elements are required to achieve the level of performances:

1. A spectrally narrow transition in the quantum system, which is insensitive to field noise fluctuations.

2. An efficient detection method decoupled from the spectroscopy transition.

3. A method to reliably prepare the system in its spectroscopic initial state.

4. The ability to cool the motional degree of freedom to minimize velocity-induced frequency shifts.

In a traditional spectroscopy experiment, a quantum system is usually composed of a single trapped atomic or molecular ion, which is chosen to have its internal levels simultaneously accommodating all four requirements above. Many atoms or molecules with potentially narrow transitions have not yet been implemented for quantum metrology [Deh82, YDN92] or quantum computing [DeM02, ADD+06, RDD+06, SBC+11] because of the challenge in performing detection, initialization, or efficient cooling. In this chapter, we consider a scheme for spectroscopy experiments using quantum logics [SRL+05], with two cotrapped single ions, so that one ion only needs to possess a narrow transition, and through entanglement between the two, requirement (2-4) can be facilitated with the second ion. For completeness, Sec. 6.1 reviews the mathematical formulation considered in [SRL+05], incorporated with a new generalized state re-initialization scheme. An original work on spectroscopic ground state preparation is given in Sec. 6.2.

6.1 Spectroscopy protocol

Here we consider a general challenge of doing spectroscopy between two internal states of a trapped ion, which has a narrow transition, but lacking an efficient detection or initialization method. In trapped-ion systems, this implies no simple cyclic dipole coupling to a third states can be established, so we denote this two level system in the spectroscopy ion with $|\downarrow\rangle_S$ and $|\uparrow\rangle_S$ as its ground and excited state, respectively. For instance, such two level system could be that between two rotational levels of a molecule, or the ${}^1S_0$-${}^3P_0$ transition in Group IIIA elements, which is appealing for high resolution spectroscopy applications. Traditional state detection and cooling methods through fluorescence scattering are usually not accessible in such two level systems, and thus making spectroscopy difficult. An indirect approach for spectroscopy, known as Quantum Logic Spectroscopy (QLS) [SRL+05] was proposed for such systems using entanglement between two ions through Coulomb interactions. In such setting, the spectroscopy ion can be entangled a cotrapped detection ion through a phonon excitation in their common motion. The latter then facilitates efficient state read-out.

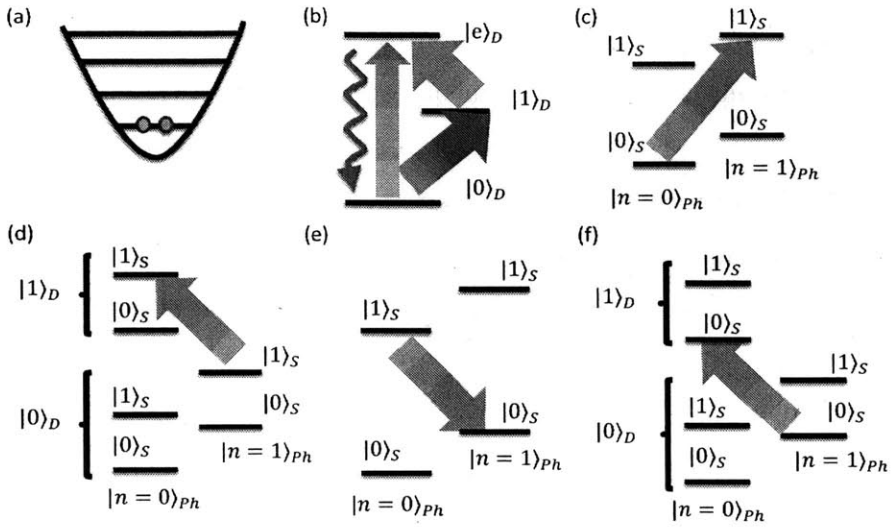

Figure 6-1: Scheme for QLS quantum logic spectroscopy. (a) Single spectroscopy ion and single detection ion co-trapped in a harmonic oscillator with levels $|n\rangle_{Ph}$. (b) Quantum logic state of the detection ion. The short-lived excited state $|e\rangle_D$ couples to the lower energy level $|\downarrow\rangle_D$ and is used for state detection. State $|\uparrow\rangle_D$ can be pumped to $|e\rangle_D$ via optical fields for initialization. (c) Blue sideband spectroscopy: a π-pulse on the BSB is used to map the $|\downarrow\rangle_S|0\rangle_{Ph}$ state to $|\uparrow\rangle_S|1\rangle_{Ph}$. (d) Phonon to detection ion state mapping. $|1\rangle_{Ph}|\downarrow\rangle_D$ is mapped to $|0\rangle_{Ph}|\uparrow\rangle_D$ with a RSB π-pulse. (e) Red sideband spectroscopy ion state to phonon state mapping: a π-pulse on the RSB is used to map the $|\uparrow\rangle_S|0\rangle_{Ph}$ state to $|\downarrow\rangle_S|1\rangle_{Ph}$. (f) Phonon to detection ion state mapping. Similar to (c), where $|1\rangle_{Ph}|\downarrow\rangle_D$ is mapped to $|0\rangle_{Ph}|\uparrow\rangle_D$ with a RSB π-pulse.

The specific experimental protocol is detailed in the remainder of this section in four steps, as shown schematically in Fig. 6-1 (c)-(f). We start from the assumption that the spectroscopy ion can be prepared in its ground state $|\downarrow\rangle_S$. Ground state cooling can be achieved via heralded state projection, the details of which are presented in Sec. 6.2.

The protocol consists of the following four parts:

(i) *State preparation:* A spectroscopy ion and a detection ion are confined in the harmonic potential of an ion trap. A schematic is shown in Figure 6-1 (a). The spectroscopy transition consists of a ground state $|\downarrow\rangle_S$ and an excited state $|\uparrow\rangle_S$. The detection ion is treated as a qubit with states $|\downarrow\rangle_D$ and $|\uparrow\rangle_D$, and with a short-lived excited state $|e\rangle_D$, which forms a cycling transition together with the $|\downarrow\rangle_D$ state

and thereby allows for efficient discrimination between the qubit states as shown in Figure 6-1 (b). To initialize the experiment, we cool the spectroscopy ion to the ground state by heralded projection (Section 6.2). Here, we assume that we are in the $|\downarrow\rangle_S$ state. We furthermore assume that the detection ion has been cooled to near its motional ground state and the translational energies of the detection and spectroscopy ions have thermalized. After this initial cooling, additional sideband cooling of a common vibrational mode of the two-ion system has brought this mode to the ground state. The initial state is thus:

$$|\downarrow\downarrow 0\rangle \equiv |\downarrow\rangle_D|\downarrow\rangle_S|0\rangle_{Ph}, \tag{6.1}$$

where the first, second, and third state represents that of the detection ion, spectroscopy ion, and phonon mode shared by the two ions, respectively.

(ii) *Blue sideband spectroscopy:* The process is illustrated in Figure 6-1 (c). After the system is prepared in the state given by Eq. 6.1, a coherent excitation is applied on or near the blue sideband (BSB) of the $|\downarrow\rangle_S \rightarrow |\uparrow\rangle_S$ transition of the spectroscopy ion. Since neither the exact frequency nor the strength of the transition is known initially, this will not be a perfect π-pulse but will transfer the $|\downarrow\rangle_S$ population to the $|\uparrow\rangle_S$ state, with some probability α. The net result of this BSB pulse is to effectively entangle the spectroscopy state with the phonon state, resulting in:

$$\sqrt{\alpha}e^{i\theta}|\downarrow\uparrow 1\rangle + \sqrt{1-\alpha}|\downarrow\downarrow 0\rangle, \tag{6.2}$$

where θ is the relative phase between the two states. We assume here that the motional sidebands are well-resolved on the $|\downarrow\rangle_S \rightarrow |\uparrow\rangle_S$ transition and that we are significantly detuned from the carrier transition. The trap frequency is well-known as this can be measured using the detection ion.

(iii) *Quantum state mapping to detection ion:* To allow for efficient state detection, we map the phonon state onto the detection ion by applying a red sideband (RSB) π-pulse on the detection ion qubit transition. The detuning and Rabi frequency for

this transition are known with high precision and we assume for simplicity that this is done with unit fidelity. This is shown in Figure 6-1 (d). The resulting state reads:

$$\sqrt{\alpha}e^{i\theta}|\uparrow\uparrow 0\rangle + \sqrt{1-\alpha}|\downarrow\downarrow 0\rangle. \tag{6.3}$$

(iv) *Detection and state re-initialization:* At this point, all the spectroscopic information contained in the transition probability α can be revealed by measuring the detection ion. This is facilitated by applying a repump field between $|\downarrow\rangle_D$ and $|e\rangle_D$, and collecting the scattered photons corresponding to the $|e\rangle_D \rightarrow |\downarrow\rangle_D$ relaxation (see e.g. $^{88}Sr^+$ ion in Sec. 3.4.1). Depending on whether the detection ion is in $|\downarrow\rangle_D$ or $|\uparrow\rangle_D$, it will either scatter photons or remain dark. By repeating the measurement on the detection ion state for different spectroscopy excitation frequencies, we can fully characterize the line shape of the spectroscopy state transition.

In order to determine α with high precision for each probe frequency, the state in Eq. 6.3 needs to be regenerated many times to build sufficient detection statistics. An efficient method for re-initializing the wave function after the collapse of Eq. 6.3 upon each detection event is therefore necessary. In our protocol, this is carried out using heralded projection. We detail the process in the following.

Depending on the measurement outcome, two different procedures are taken: In the simplest case, the measurement outcome is $|\downarrow\rangle_D$ and the system has been projected onto the $|\downarrow\downarrow 0\rangle$ state. In this scenario, the system has been reinitialized and the spectroscopy protocol can start again. If, on the other hand, $|\uparrow\rangle_D$ is detected, the system is projected onto the $|\uparrow\uparrow 0\rangle$ state. Reinitialization to the $|\downarrow\downarrow 0\rangle$ state can proceed by first removing the detection ion excitation via a repump field from state $|\uparrow\rangle_D$ to $|e\rangle_D$, which will relax to $|\downarrow\rangle_D$, leaving the overall wave function in the spectroscopy state excitation $|\downarrow\uparrow 0\rangle$. Possible excitation of the phonon state during this process can be removed through a brief sequence of sideband cooling on the detection ion. To remove the spectroscopy state excitation, similar to step (ii) and (iii), one can transfer it to the detection ion via the phonon bus. More specifically, one can apply a RSB π-pulse on the spectroscopy transition as illustrated in Figure 6-1

(e), resulting in

$$\sqrt{\alpha}e^{i\theta}|\downarrow\downarrow 1\rangle + \sqrt{1-\alpha}|\downarrow\uparrow 0\rangle. \tag{6.4}$$

Note that the RSB Rabi frequency is lower than that of the BSB (c.f. Eq. 6.2) by a factor of $\sqrt{2}$. We therefore adjust the excitation pulse length accordingly to maintain the same probability α for the π-pulse transition. Now, similar to Eq. 6.3, making a RSB transition on the detection ion state (see Figure 6-1 (f)) changes the wave function into

$$\sqrt{\alpha}e^{i\theta}|\uparrow\downarrow 0\rangle + \sqrt{1-\alpha}|\downarrow\uparrow 0\rangle. \tag{6.5}$$

Upon measuring the detection ion state of Eq. 6.5, the system is either projected to $|\uparrow\downarrow 0\rangle$, which can be brought down to $|\downarrow\downarrow 0\rangle$ by optical pumping, or $|\downarrow\uparrow 0\rangle$, which can be cooled again by repeating the pulse sequences in Eq. 6.4 and Eq. 6.5.

6.2 Ground state preparation

We recall that in Sec. 6.1, we have begun in our QLS protocol with an initial state $|0\rangle_D|\downarrow\rangle_S|0\rangle_{Ph}$ (c.f. Eq. 6.1), assuming that the spectroscopy ion can be prepared in its pure ground state $|\downarrow\rangle_S$. However, unlike the detection ion internal state or the phonon state, direct laser cooling is non-trivial for the spectroscopy ion since the transition considered in our case is not coupled to a cyclic transition. In this section, we outline an approach for which ground state preparation for spectroscopy transitions without cyclic coupling can be achieved through a heralded projection cooling scheme in the QLS setting. The techniques follow similarly to the state initialization process introduced in Sec. 6.1. For completeness, in several specific cases where e.g. rotational state spectroscopy is considered for large molecular ensembles, ground state preparation schemes have been implemented through direct laser cooling [SHS+10, SRD+10] and by state selective loading of the ion trap [TWW10]. In [SRL+05], a deterministic cooling scheme is implemented for the clock transition of a single Al^+ ion as well.

We first consider a larger Hilbert space $\mathcal{S}$ with N states, the eigenstates of which we denote $|n\rangle_S$, containing the ground state of the spectroscopy ion $|\downarrow\rangle_S$. In gen-

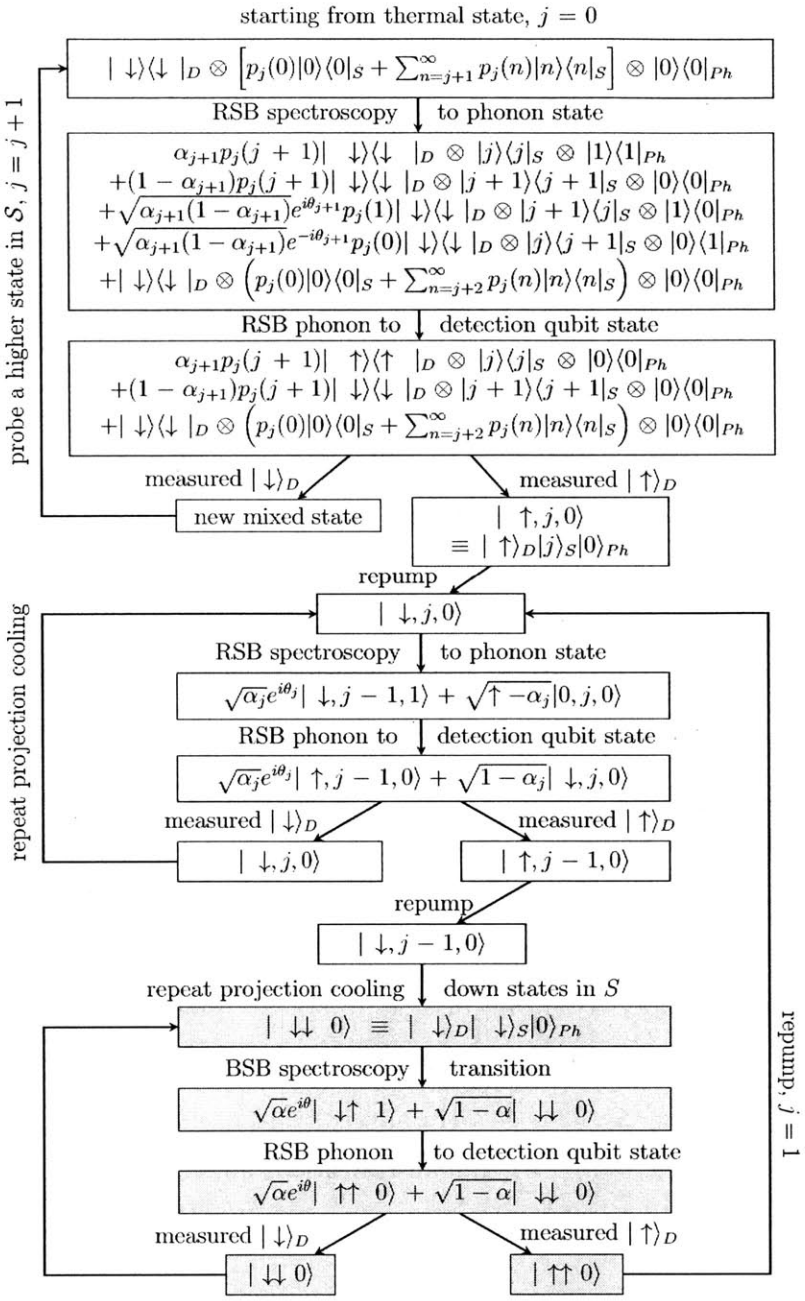

Figure 6-2: Summary of the quantum logic spectroscopy protocol. Green: initial ground state preparation via projection measurement for a single spectroscopy ion and detection ion pair. Purple: spectroscopy procedure starting with system initialized to spectroscopy ground state. State re-initialization is achieved using projection measurement. The index j refers to the j^{th} cooling cycle after failing in projecting the mixed rotational state onto a pure state $|j-1\rangle_S$

eral, due to thermal excitation, each state $|n\rangle_S$ in $\mathcal{S}$ is populated with some initial probability $p_0(n)$, resulting in a mixed state

$$|\downarrow\rangle\langle\downarrow|_D \otimes \left[\sum_{n=0}^{N} p_0(n)|n\rangle\langle n|_S\right] \otimes |0\rangle\langle 0|_{Ph}, \tag{6.6}$$

where n denotes the quantum number in $\mathcal{S}$. For simplicity in wave function indexing, we rename $|\downarrow\rangle_S$ as $|0\rangle_S$. We also assume without loss of generality that we can address the transitions between two adjacent levels with a coherent excitation, which we refer as the cooling excitation in the following. For instance, in the case of spectroscopy in molecular ion rotational states, due to the small energy (in GHz range) spacing, all rotational levels may be occupied at temperatures a typical ion-trap experiment operates. Thus $\mathcal{S}$ refers to the whole set of rotational levels, with $|n\rangle_S$ indexing the rotational state wave function $|J\rangle_S$, and the system dimension N is infinite. The cooling excitation connecting adjacent levels are the same as the spectroscopy excitation, which e.g. can be a direct coherent microwave pulse. Whereas in some other cases, such as for an atomic clock transition, because the $|\downarrow\rangle_S \rightarrow |\uparrow\rangle_S$ transition is in the optical range, thermal excitation typically does not populate the spectroscopy excited state. $\mathcal{S}$ thus does not contain $|\uparrow\rangle_S$. $|n\rangle_S \equiv |m_F\rangle_S$ indexes the hyperfine magnetic sub-level number, resulting in a finite system dimension of $N = 2F + 1$, where F is the hyperfine total angular momentum quantum number. The cooling excitation among $|n\rangle_S$ is therefore not the spectroscopy transitions, but in this case refers to e.g. a direct microwave, or Raman transitions among the hyperfine levels.

Similar to the techniques presented in the QLS protocol, ground state preparation can be done by entangling the spectroscopy ion with the detection qubit ion, and projecting the former down to its ground state upon state detection of the latter. We perform the state mapping between the two via the phonon bus using a RSB π-pulse on the $n \rightarrow n-1$ cooling transition followed by a RSB π-pulse on the detection ion

qubit, as outlined in Section 6.1 (iv). The density matrix in Eq. 6.6 then turns into:

$$\begin{aligned}
&\beta_1 p_0(1)|\uparrow\rangle\langle\uparrow|_D \otimes |0\rangle\langle 0|_S \otimes |0\rangle\langle 0|_{Ph} \\
&+(1-\beta_1)p_0(1)|\downarrow\rangle\langle\downarrow|_D \otimes |1\rangle\langle 1|_S \otimes |0\rangle\langle 0|_{Ph} \\
&+|\downarrow\rangle\langle\downarrow|_D \otimes \left[\sum_{n\neq 1}^{N} p_0(n)|n\rangle\langle n|_S\right] \otimes |0\rangle\langle 0|_{Ph}
\end{aligned} \tag{6.7}$$

where, β_1, similar to α in Eq. 6.2 s the probability of transitioning between $|0\rangle_S$ and $|1\rangle_S$ at the frequency of the cooling source, which converges to unity on resonance.

Upon measuring the detection ion in $|\uparrow\rangle_D$, the wave function in $\mathcal{S}$ is thus projected to its ground state $|0\rangle_S$. Such detection has been demonstrated with infidelities below 10^{-4} [MSW+08], which makes this a very robust scheme for ground state preparation. The probability of detecting $|\uparrow\rangle_D$, and thus projecting $\mathcal{S}$ to $|0\rangle_S$ is

$$\mathcal{P}_1^{cool} = \beta_1 p_0(1), \tag{6.8}$$

which converges to the population of $|0\rangle_S$, $p_0(1)$ when β_1 is close to unity, i.e. for a perfect π-pulse on the RSB cooling transition. If on the other hand, the measurement outcome of the protocol is $|\downarrow\rangle_D$, $\mathcal{S}$ is projected to yet another mixed state

$$|\downarrow\rangle\langle\downarrow|_D \otimes \left[\sum_{n=0}^{\infty} p_1(n)|n\rangle\langle n|_S\right] \otimes |0\rangle\langle 0|_{Ph}. \tag{6.9}$$

However, for the new mixed state, $p_1(1) \propto (1-\beta_1)p_0(1)$, which converges to 0 when the RSB transition $|1\rangle_S \rightarrow |0\rangle_S$ is close to resonance. That is to say, the system renormalizes so that the first excited state $|1\rangle_S$ is emptied and the ground state $|0\rangle_S$ is populated with a higher probability $p_1(0) \sim p_0(0)/(1-p_0(1))$.

Following the same pulse sequence, one can proceed to probe the next most populated state, namely $|2\rangle_S$, with the addressing cooling frequency tuned close to the $|2\rangle_S \rightarrow |1\rangle_S$ resonance. Similarly, the new mixed state purifies the system further,

yielding

$$\begin{aligned}
&\beta_2 p_1(2)|\uparrow\rangle\langle\uparrow|_D|1\rangle\langle 1|_S|0\rangle\langle 0|_{Ph} \\
&+(1-\beta_2)p_1(2)|\downarrow\rangle\langle\downarrow|_D|2\rangle\langle 2|_S|0\rangle\langle 0|_{Ph} \\
&+|\downarrow\rangle\langle\downarrow|_D\left[\sum_{n\neq 1,2}^{N} p_1(n)|n\rangle\langle n|_S\right]|0\rangle\langle 0|_{Ph},
\end{aligned} \tag{6.10}$$

where β_2 is the transition probability between $|1\rangle_S$ and $|2\rangle_S$. Due to the state renomalization after removing the population in $|1\rangle_S$, the probability of detecting $|1\rangle_D$ at this second cooling attempt follows

$$\mathcal{P}_2^{cool} = \beta_2 p_1(2) \rightarrow p_1(2) > p_0(2), \tag{6.11}$$

where the convergence $\beta_2 p_1(2) \rightarrow p_1(2)$ takes place when the transition is addressed on resonance.

Detection of $|\uparrow\rangle_D$ from the new mixed state in Eq. 6.10 will then project the state to $|\uparrow\rangle_D|1\rangle_S|0\rangle_{Ph}$. Because this is a pure state, it can be brought down to the ground state by repeating the projection cooling between $|1\rangle_S$ and $|0\rangle_S$ (see part (iv) of the spectroscopy protocol in Sec. 6.1 for the case $|\downarrow\rangle_D|1\rangle_S|0\rangle_{Ph} \equiv |\downarrow\rangle_D|\uparrow\rangle_S|0\rangle_{Ph}$).

In the case $|\downarrow\rangle_D$ is detected, a new mixed state is obtained with the first and second excited state emptied, and the ground state populated with higher probability due to re-normalization. Therefore, to cool the thermal state in Eq. 6.6, one can probe the rotational transition of $|1\rangle_S \rightarrow |0\rangle_S$, $|2\rangle_S \rightarrow |1\rangle_S$, etc., until the system is projected to a pure state $|\downarrow\rangle_D|j\rangle_S|0\rangle_{Ph}$, which can then be projected down to the ground state following the ladder downwards.

6.3 Conclusions and discussion

In this chapter, we have set up the theoretical frame work of quantum logic spectroscopy. The spectroscopy protocol is summarized in Fig. 6-2. This approach can be

applied in general for spectroscopy on narrow transitions, which are not connected to other states via cyclic double coupling. For instance, in QIS using rotational states of molecular ions, this method is particularly useful for single molecule rotational state spectroscopy. In Chap. 7, we will apply this formalism on the rotational states of $SrCl^+$ ion.

Chapter 7

Molecular ion qubits and microwave QLS

Precise measurement and control of ultracold molecules are essential to the advancement of a wide range of scientific fields. The development of cooling and control techniques for neutral molecules has, e.g., led to the study of novel quantum phases in the ultra-low temperature regime [CY09]; the extreme isolation of molecules from environment at milliKelvin temperatures offers an ideal setup for the studies of chemical reaction [WBGS08], astrophysical processes [CCS93], time-variation of physical constants [SK05, BKB+11], as well as the search for the electron electric dipole moment [SC04, MBD06]; moreover, the rich internal structure of molecules make them promising candidates for quantum information processing [DeM02], especially trapped polar molecular ions, due to their long storage time and large permanent dipole moment. In a quantum processor, where rotational states of a polar molecular ion is used as a qubit [SBC+11], the long coherence time and relatively large permanent dipole moment results in a favorable ratio between the rate at which information can be manipulated and the rate at which information is lost. Furthermore, because these rotational state qubit transitions lie in the microwave range, they can be addressed with fields integrated to a planer trap design, with reliable and stable sources that are readily available. Not only can this significantly reduces the experimental overhead

compared with atomic-ion implementations with highly-stable laser sources in the visible and uv-range [BW08], it also opens a channel for hybridizing trapped-ion and super-conducting qubits, incorporating their long-coherence (memory) and fast-gate (processing) features, respectively [ADD+06].

Despite the appealing features polar molecular ions offered for QIS, there have been four significant challenges opposing the implementation of a quantum processor based on polar molecules and coherent microwave fields: (i) The absence of closed transitions between the rovibrational states implies conventional spectroscopy techniques through fluorescence photon scattering fails in state detection. (ii) Cooling and state initialization are similarly complicated by the lack of a cycling transition. (iii) The long wavelengths of the microwave transitions implies that there is negligible coupling to the motion of the molecular ion and, hence, any conditional multi-qubit gate relying a motional bus, such as Ref. [CZ95, MS99], will be very slow. (iv) Finally, individual addressing of molecular ions is also complicated by the use of long ($\sim$cm) wavelengths due the typical ion spacings in ion traps being on the order of 10 μm. In this chapter, we show that the protocol of QLS we developed in Chapter 6 can be incorporated for molecular ion qubits to address the above concerns. We show that by entangling a molecular ion qubit with an atomic ion with well characterized spectroscopic transitions, the rotational state spectroscopy can be achieved via state detection on the atomic ion; cooling and state initialization can be realized via atomic ion manipulation and molecular ion heralded projection. A scheme for efficient microwave photons coupling to the molecular motional states is shown in a laser or cavity-induced AC Stark field, the manipulation on which also allows for individual addressing on molecular ion qubits.

Sec. 7.1 formulates the rotational state qubit levels of a polar molecular ion. Sec. 7.2 examines the detailed experimental feasibility for microwave QLS for molecular ions, addressing spectroscopy, cooling, state initialization, efficient phonon coupling, and individual addressing. The chapter is concluded with a section of discussion.

7.1 Rotational state qubit in polar molecular ions

We consider the quantum dynamics of a diatomic molecule with one shell electron. Due to the complex Coulomb interactions among electrons and nuclei, the full Hamiltonian describing the molecular dynamics cannot be solved exactly. Nonetheless, due to the vanishing ratio of mass and hence time scale, the electronic and nuclear dynamics in many cases can be separated using Born-Oppenheimer approximation. Furthermore, the nuclear motions can be decomposed into center of mass and relative motions. The rotational motion, as part of the nuclear relative motion can be further separated under a rigid rotor approximation, where the relative distance between the two nuclei is considered constant due to again, the vanishing energy scale ratio between rotational and vibrational motions. We detail the derivation of Born-Oppenheimer approximation in Appendix B, and quote the resultant Hamiltonian for molecular rotation motions directly:

$$\mathcal{H}_{\text{rot}}(\theta,\phi) = \frac{1}{2}\frac{\mathbf{L}^2}{\mu R_0^2} = \frac{\mathbf{L}^2}{2I_0}, \tag{7.1}$$

where $I_0 = \mu R_0^2$ is the moment of inertia of the rotor at a fixed inter-nuclear distance R_0. The eigenstates of Eq. 7.1 are the spherical harmonics $Y_{J,m_J}(\theta,\phi)$, where J and m_J are the angular momentum and magnetic quantum numbers of the rotational motion, respectively, and the energy levels follow

$$\mathcal{H}_{\text{rot}} Y_{J,m_J}(\theta,\phi) = E_J^{\text{rot}} Y_{J,m_J}(\theta,\phi), \tag{7.2}$$

where $E_J^{\text{rot}} \equiv \hbar C \equiv \hbar \cdot \frac{\hbar}{2I_0} J(J+1)$. The constant C is usually referred as the rotational constant of molecules.

The relative error due to the rigid rotor approximation for the rotational levels is considered with more details in Ref. [Ant11]. Treating the inter-nuclei interaction as a perturbation in the centrifugal force of rotation, the rotational Hamiltonian with a

first order correction follows

$$\tilde{\mathcal{H}}_{\rm rot}(\theta,\phi) = \frac{\mathbf{L}^2}{2I_0}\left(1 - \frac{\mathbf{L}^2/2I_0}{kR_0^2/2}\right), \tag{7.3}$$

where k is the vibrational energy constant. The correction due to vibration, not surprisingly, is the rotational to vibrational energy spacing ratio of the molecule, which is typically on the order of 0.1%.

At the electronic ground state, the $J = 0$ and 1 rotational levels of molecule are promising candidates for qubits in trapped-ion quantum computing, for (i), the energy spacing rises non-linearly, making qubit addressing not mixed with the other levels; (ii) the magnetic dipole moment due to nuclear rotation is negligibly small in comparison to that of atomic ions, resulting in a robust qubit system to magnetic field noise; (iii), the line width $\Gamma_{J=1}$ of the qubit transition follows

$$\Gamma_{J=1} = \frac{\omega_{01}^3 |\boldsymbol{\mu}_{01}\cdot\hat{\mathbf{z}}|^2}{3\pi\epsilon_0\hbar c^3}, \tag{7.4}$$

where $\omega_{01} = (E_1^{\rm rot} - E_0^{\rm rot})/\hbar$ is the transition frequency. $\boldsymbol{\mu}_{01} = e\langle 1|\mathbf{r}|2\rangle$ is the electric dipole moment, with e denoting the electron charge. ϵ_0 and c are the electric permittivity and speed of light in vacuum. Because of the low energy spacing between rotational levels (GHz), the coherence time can be 10^{15} longer than that of an atomic electric dipole transition (100THz). However, also due to the dense rotational energy spacing as well, there can be hardly cyclic transitions, based on which traditional direct laser cooling, fluorescent detection or ground state initialization are implemented. Qubit spectroscopy is thus challenging. Nonetheless, in the next section, we aim to set up a new experimental proposal for molecular ion rotational state spectroscopy using the formalism developed in Chapter 6.

7.2 Microwave QLS for molecular ions

The construction of a quantum computer based on microwave-addressed trapped polar molecular ion qubit is challenging. Qubit spectroscopy and ground state initialization is hard to implement for the lack of cyclic coupling in qubit transitions. Entanglement through phonon coupling and individual qubit addressing is difficult to access due to the long wavelength of microwaves for qubit control. For spectroscopy, most current methods used for single or clouds of molecules are destructive [BJD06, HHS+09, RKDS06, CSK+11, SHS+10, SRD+10, TWW10], against the concept of long qubit storage time in ion traps. For state initialization, most implementations require dedicated laser systems for qubit manipulation [VMD06b, VMD06a, SRK+06, Lei12, SHS+10, SRD+10, TWW10]. Although in these cases replacing microwaves with optical fields can remove the difficulties in phonon coupling and individual qubit addressing, it opposes the simplicity and hybridizability of on-chip microwave integration for molecular ion qubits. One method to incorporate direct microwave qubit control, while still able to perform rotational spectroscopy is the QLS protocol we developed in Chapter 6. In this section, we aim to examine the experimental feasibility for applying QLS to rotational states of polar molecular ions, with direct microwave addressing. In particular, an experiment design with $SrCl^+$ cotrapped with Sr^+ is described as a detailed demonstration in Sec. 7.2.1. In Sec. 7.2.2, and 7.2.3, we examine and address the additional requirements for the use of microwave.

7.2.1 Experiment design with $SrCl^+$

In this section, we describe how microwave qubit control and spectroscopy can be realized in the QLS framework for $SrCl^+$ molecule rotational levels. To examine the overall experimental feasibility, we analyze the processing time for each step and compare them with the various characteristic decoherence time scales for internal and external states. Before each incoherent operation takes place (namely a detection or

Table 7.1: Experiment parameters for microwave QLS spectroscopy on molecular rotations

System	Experiment parameters	Symbol	Value	Units
$SrCl^+$	π-pulse	π/Ω_S	5	ns
	LDP	η_S	0.1	a.u.
	Decoherence time	$\tau_S^{1\to 0}$	100	ms
Sr^+	π-pulse	π/Ω_D	2	μs
	LDP	η_D	0.02	a.u.
	Decoherence time	$\tau_D^{\uparrow\to\downarrow}$	390	ms
Phonon	Decoherence time	τ_{Ph}	0.5	s^{-1}

cooling process in our case), the processing time t should follow

$$t \ll \min\{\tau_S^{1\to 0}, \tau_D^{\uparrow\to\downarrow}, \tau_{Ph}\}, \tag{7.5}$$

where $\tau_S^{1\to 0}$ and $\tau_D^{\uparrow\to\downarrow}$ are the life times of $|1\rangle_S$, and $|\uparrow\rangle_D$, respectively. τ_{Ph} is the time scale corresponding to the phononic anomalous heating. These time constants are summarized in Table. 7.1.

We consider a single $SrCl^+$ and a single Sr^+ ion confined in the harmonic potential from a planer ion trap. We described a general protocol of QLS in Chapter 6. In this particular case, the spectroscopy transition of interest is between the ground and first rotational levels of $SrCl^+$, following

$$|\downarrow\rangle_S \equiv |J=0\rangle_{SrCl^+,{}^1\Sigma}, \quad |\uparrow\rangle_S \equiv |J=1\rangle_{SrCl^+,{}^1\Sigma}, \tag{7.6}$$

the electronic configuration of which is in the $^1\Sigma$ ground state. For the detection ion Sr^+, transition $5S_{1/2}(m=-1/2) \to 4D_{5/2}(m=-5/2)$, and $4D_{5/2}(m=-5/2) \to 5P_{3/2}$ are used respectively as a the qubit and repump transitions, as for single Sr^+ ion qubit operations in Sec. 3.4.1, following

$$|\downarrow\rangle_D \equiv |S_{1/2}, m_{-1/2}\rangle_{Sr^+}, \quad |\uparrow\rangle_D \equiv |D_{5/2}, m_{-5/2}\rangle_{Sr^+}, \quad |e\rangle_D \equiv |P_{3/2}\rangle_{Sr^+}. \tag{7.7}$$

Extensive work on the trapping of $SrCl^+$ and Sr^+ ions has been accomplished in P. An-

tohi's thesis work [Ant11], in which the techniques used can be faithfully transferred to set up preliminary steps for QLS. In particular, loading of Sr^+ ions can be achieved through ionizing a Sr metal oven flux, whereas $SrCl^+$ can be obtained through laser ablation on a $SrClO_3$ crystal. To reduce the cooling overhead for internal and external motion degrees of freedoms, vacuum systems with a bath or closed-cycle cryostat enclosure can also be used. Sympathetic cooling of the $SrCl^+$ motion can be achieved through Doppler cooling on the Sr^+ ion (see e.g. Ref. [EMSKB03]). Cooling to common motion ground state by further phonon excitation removal can be achieved via sideband cooling [DBIW89].

The first step of QLS as outlined in Chapter 6.1 is to cool $SrCl^+$ ion to its spectroscopy ground state $|\downarrow\rangle_S$. According to our formalism in Sec. 6.2, the larger thermally populated Hilbert space $\mathcal{S}$ containing $|\downarrow\rangle_S$ is spanned by all the rotational levels, so the its eigen levels $|n\rangle_S$ follow

$$|n\rangle_S \equiv |J = n\rangle_{SrCl^+,{}^1\Sigma}. \tag{7.8}$$

The thermal population $p_0(n)$ of each state $|n\rangle_S$ follows Boltzmann distribution,

$$p_0(n) = \frac{\hbar C}{k_B T} \exp\left[-\hbar C n(n+1)/k_B T\right], \tag{7.9}$$

where the rotational constant $C = 6.5$ GHz (c.f. Eq. 7.2). At temperature $T = 5$ K in a cryogenic environment for instance, $p_0(n)$ for the first few states is shown in Fig. 7.2.1 (a). Following the protocol of state preparation, the mixed state can be purified with heralded projection, with probability $\mathcal{P}_1^{cool} \to 0.17$ and $\mathcal{P}_2^{cool} \to 0.22$, etc., where the arrows indicate the probability convergence at the resonance transition frequency. The renormalized distribution after each attempt of cooling (if not yet purified) is shown in Fig. 7.2.1 (b-j). The total failure rate after 9 attempts of cooling projection is $p_0(n > 9)/[p_0(n > 9) + p_0(0)] = 0.03$. The microwave frequency needed at this $|9\rangle_S \to |8\rangle_S$ transition is 117 GHz, which can be easily obtained from a commercial supplier, e.g. Agilent E8257D PSG with a frequency doubler. We leave

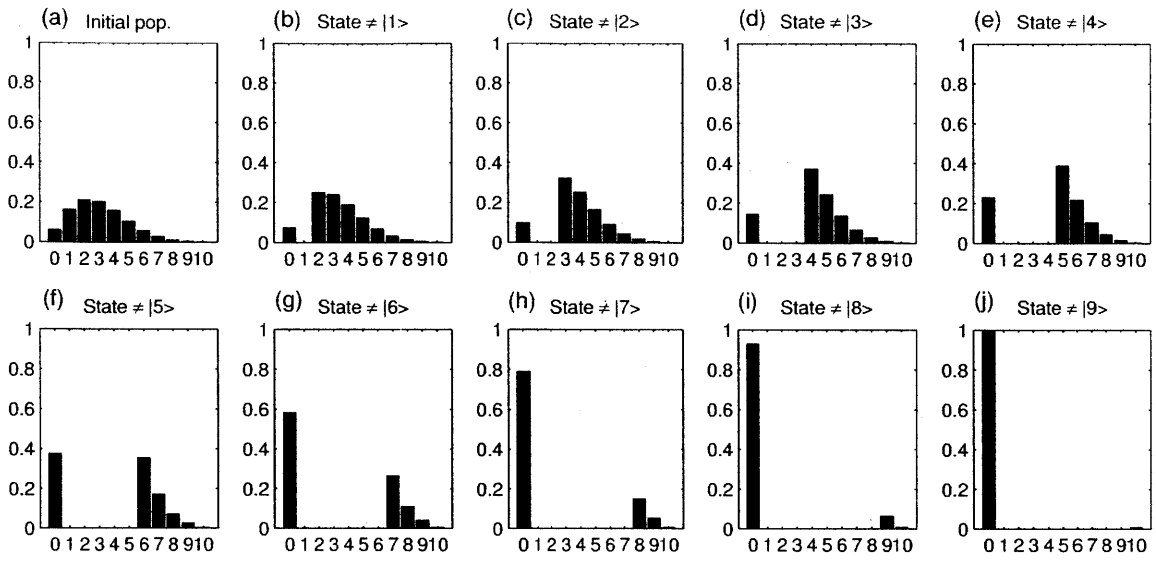

Figure 7-1: Evolution of the renormalized molecular rotational state population distribution after projecting the system to a new mixed state via heralded projection cooling, assuming $\alpha = 1.0$

the feasibility analysis for cooling process to the end this section, since this process involves all the techniques used in the rest of steps.

Once ground state cooling is completed, the protocol calls for a microwave-addressed blue sideband π-pulse on the $SrCl^+$ rotational state transition (See Eq. 6.2). In a typical planer trap design involving a microwave cavity or coplaner waveguide, the microwave electric field strength at the ion can reach ~500kV/m at a 1V microwave signal applied (See, e.g. Chapter 5 of Ref. [Ant11]). With a ~10 Debye dipole moment, a 200 MHz Rabi frequency can be obtained for the microwave addressed rotational state transition. It is however, non-trivial to operate a sideband transition, since the Lamb-Dicke parameter (LDP) η_S associated with the long wavelength of microwave signals is typically too small (See Eq. 2.18). Nonetheless, it is possible to engineer an effective, sufficiently large Lamb-Dicke parameter using an electric field gradient. We save the detailed discussion until Sec. 7.2.2, and here use the result directly. With $\eta_S = 0.01$, the total time t_2 needed for this step is approx. 0.5 μs.

The third step involves the quantum state transfer to the Sr^+ ion. In a typical

experiment setting, a Rabi frequency if 200 kHz[1] and a Lamb-Dicke parameter of 0.02 for Sr^{+2} can be obtained for the $|\downarrow\rangle_D \rightarrow |\uparrow\rangle_D$ transition. Therefore the time t_3 need for this step is roughly 0.1 ms.

The first incoherent operation takes place during the last last step of our protocol, where the quantum state transferred to the Sr^+ qubit is detected. $t_3 = 0.1$ ms contributes predominately to the total processing time in all previous steps, which well satisfies Eq. 7.5. The re-initialization part consists of a blue sideband transition $SrCl^+$, and a quantum state transfer to Sr^+. Therefore, the processing time involved in this stage is roughly the same as the sum of t_2 and t_3, satisfying Eq. 7.5 as well.

We now return to the first cooling stage of our protocol. Although most times several cooling cycles may be needed before the system reaches a rotational ground state, a projection measurement takes place at the end of each cycle. Therefore, we only need to analyze the processing time for each cooling cycle, which similarly to the re-initialization process, consists of a rotational sideband transition and a quantum state transfer, resulting in a required time of $t_2 + t_3 = 0.1$ ms, within our limit set in Eq. 7.5.

7.2.2 Effective Lamb-Dicke parameter

In Sec. 7.2.1, we have left out a key element in the discussion of processing time for $SrCl^+$ rotational states. The time scale associated with the sideband transitions depends critically on the the Lamb-Dicke parameter, which for long-wavelength microwave transitions, is vanishingly small. Nonetheless, a large, effective Lamb-Dicke parameter can be engineered by creating a state-dependent ion-field interaction with an assisting field gradient. This is because the ion coupling to the field gradient experiences a state-dependent force and hence a different equilibrium position in the trap. An internal transition can thus result in a slight displacement of the ion motion, giving rise to a more efficient phonon coupling. In this section, we outline a scheme to

[1]See for example, Chapter 4 of Ref. [Lab08]

[2]characterized performance of Nb surface trap, Chapter 5 of Ref. [Ant11], obtained from measured secular frequency of 180 kHz

implement this idea using a far-off resonance laser field, to which rotational states of the molecule are coupled via differential AC Stark shift. For completeness, the idea of achieving an effective, non-negligible Lamb-Dicke parameter was first proposed and implemented for atomic ion hyperfine transitions, using magnetic field gradient [MW01, OLA+08, OWC+11, TBJ+11]. This method however, does not extend straightforwardly in our case for molecules, whose magnetic dipole moments are vanishingly small. This is because for a typical diatomic such as $SrCl^+$, the electronic ground state is in the $^1\Sigma$ configuration with vanishing angular momentum. Angular momenta from nuclear rotational motions are negligibly small compared to those from electrons, because the former is three orders of magnitude more massive.

Formalism

We consider again the spectroscopy transition $|\downarrow\rangle_S \rightarrow |\uparrow\rangle_S$ between the lowest two rotational states of $SrCl^+$, which has mass m and is confined in a harmonic potential. One eigenmode resulted from this harmonic motion has frequency ω_t, and we define its direction as the z-axis. The Hamiltonian for this system is

$$H = \frac{1}{2}\hbar\omega(z)\sigma_z + \hbar\omega_t a^\dagger a, \tag{7.10}$$

where $\sigma_z = |\uparrow\rangle_S\langle\uparrow| - |\downarrow\rangle_S\langle\downarrow|$, and a and $a^\dagger$ are the annihilation and creation operators of the motional states, respectively. The energy difference between the two rotational states has a spatial dependence acquired through the interaction with some spatially varying external potential:

$$\omega(z) = \frac{1}{\hbar}\left[\epsilon_1(z) - \epsilon_0(z)\right]. \tag{7.11}$$

Inserting into the Hamiltonian, we get

$$H = \frac{1}{2}\left[\epsilon_1(z) - \epsilon_0(z)\right]\sigma_z + \hbar\omega_t a^\dagger a. \tag{7.12}$$

At this point we make the assumption that the ion makes only small excursions around the trap location $z = 0$ and that the energy of the two states is linear in their interaction with the external potential. This justifies only keeping terms to first order in an expansion of the energies of the two states ($j = 0, 1$):

$$\epsilon_j = \epsilon_j(0) + \frac{\partial \epsilon_j(z)}{\partial z}\Big|_{z=0} \times z = \epsilon_j(0) + \partial_z \epsilon_j(z) \times \sigma_0(a + a^\dagger), \tag{7.13}$$

where we have expressed the position operator through the annihilation and creation operators and where we have defined $\sigma_0 = \sqrt{\frac{\hbar}{2m\omega_t}}$ as the ground state wave packet size. Inserting into the expression for the Hamiltonian we get

$$H = \frac{1}{2}\hbar\omega_0\sigma_z + \hbar\omega_t a^\dagger a + \frac{1}{2}\hbar\omega_t\epsilon_c(a + a^\dagger)\sigma_z, \tag{7.14}$$

where

$$\omega_0 = \frac{1}{\hbar}\left[\epsilon_1(0) - \epsilon_0(0)\right] \tag{7.15}$$

and

$$\epsilon_c = \frac{\sigma_0}{\hbar\omega_t}\partial_z\left[\epsilon_1 - \epsilon_0\right]_{z=0}. \tag{7.16}$$

The last term describes a coupling between the rotational states and the motion of the molecular ion, which corresponds to the energy levels shifting as the ion is moving. This is of course what one expects from a potential gradient that couples to the energy levels; nevertheless, it is useful for our treatment here to transform into a frame in which the energy levels, in the presence of the external potential, are constant. This is achieved through the unitary transformation $\tilde{H} = e^{iS}He^{-iS}$, where $S = \frac{1}{2i}\epsilon_c(a^\dagger - a)\sigma_z$. Invoking this, the transformed Hamiltonian reads

$$\tilde{H} = \frac{1}{2}\hbar\omega_0\sigma_z + \hbar\omega_t a^\dagger a - \frac{1}{4}\hbar\omega_t\epsilon_c^2. \tag{7.17}$$

The last constant term does not affect the dynamics and will therefore be ignored in the following.

We now introduce an electromagnetic field that interacts with the molecular ion

on, or near, the $|0\rangle_S \leftrightarrow |1\rangle_S$ transition. The corresponding Hamiltonian reads:

$$H_E = \frac{1}{2}\hbar\Omega(\sigma_+ + \sigma_-)(e^{i[k_z z - \omega_E t]} + \text{H.c.}), \tag{7.18}$$

where $\Omega = \frac{\boldsymbol{\mu}\cdot\mathbf{E}}{\hbar}$ is the Rabi frequency, with μ being the relevant transition dipole moment and E the electromagnetic field strength. ω_E is the frequency of the field and $k_z = \frac{\omega_E}{c}\cos\Theta$ is the wave vector, with Θ accounting for the angle between the incident beam and the z-axis. Note that we are using the subscript E to signify that the transition of interest is an electric dipole transition, specifically, the $|0\rangle_S \leftrightarrow |1\rangle_S$ rotational transition.

We replace the position coordinate by its quantum mechanical operator, $z = \sigma_0(a^\dagger + a)$, and rewrite Eq. 7.18 in terms of the LDP $\eta = \sigma_0 k_z$:

$$H_E = \frac{1}{2}\hbar\Omega(\sigma_+ + \sigma_-)(e^{i[\eta(a^\dagger + a) - \omega_E t]} + \text{H.c.}). \tag{7.19}$$

The interaction Hamiltonian is transformed as above according to $\tilde{H}_E = e^{iS} H_E e^{-iS}$, which gives

$$\begin{aligned} \tilde{H}_E &= \frac{1}{2}\hbar\Omega(\sigma_+ e^{\epsilon_c(a^\dagger - a)} + \sigma_- e^{-\epsilon_c(a^\dagger - a)}) \\ &\times \ (e^{i[\eta(a^\dagger + a - \epsilon_c\sigma_z) - \omega_E t]} + \text{H.c.}) \end{aligned} \tag{7.20}$$

It is useful to transform $\tilde{H}_E$ into the interaction picture with respect to $\tilde{H}$, i.e., performing the transformation $\tilde{H}_E^{\text{int}} = e^{i\tilde{H}t/\hbar}\tilde{H}_E e^{-i\tilde{H}t/\hbar}$, where $\tilde{H} = \frac{1}{2}\hbar\omega_0\sigma_z + \hbar\omega_t a^\dagger a$ as found above. Invoking the rotating wave approximation, omitting terms oscillating at $2\omega_0$, the final result for the interaction Hamiltonian reads:

$$\begin{aligned} \tilde{H}_E^{\text{int}} &= \frac{1}{2}\hbar\Omega\Big(\sigma_+ e^{-i(\Delta t - \eta\epsilon_c)} \times e^{i[(\eta + i\epsilon_c)a + (\eta - i\epsilon_c)a^\dagger]} \\ &+ \ \sigma_- e^{i(\Delta t + \eta\epsilon_c)} \times e^{-i[(\eta + i\epsilon_c)a + (\eta - i\epsilon_c)a^\dagger]}\Big), \end{aligned} \tag{7.21}$$

where $\Delta = \omega_E - \omega_0$ is the frequency detuning.

From the above expression for the interaction Hamiltonian, we can define an

effective, complex LDP: $\eta_{\text{eff}} = \eta + i\epsilon_c$. Rewriting this complex parameter in terms of its magnitude and phase, we get $\eta_{\text{eff}} = \sqrt{\eta^2 + \epsilon_c^2} e^{i\phi}$, where the phase $\phi = \arctan(\epsilon_c/\eta)$ for $\eta > 0$. The interaction Hamiltonian can now be written as:

$$\tilde{H}_E^{\text{int}} = \frac{1}{2}\hbar\Omega \left(\sigma_+ e^{-i\Delta t} \times e^{i\sqrt{\eta^2+\epsilon_c^2}[a e^{i\phi} + a^\dagger e^{-i\phi}]} + H.c. \right), \tag{7.22}$$

where we have absorbed the $e^{i\eta\epsilon_c}$ phase into σ_+, which is only defined up to an arbitrary phase. Similarly, we may absorb the $e^{\pm i\phi}$ phases into a and $a^\dagger$, in which case the interaction Hamiltonian is expressed simply as

$$\tilde{H}_E^{\text{int}} = \frac{1}{2}\hbar\Omega \left(\sigma_+ e^{-i\Delta t} \times e^{i|\eta_{\text{eff}}|[a + a^\dagger]} + H.c. \right). \tag{7.23}$$

The key result of this derivation, as was first pointed out by Mintert and Wunderlich [MW01], is that an effective LDP, $|\eta_{\text{eff}}| = \sqrt{\eta^2 + \epsilon_c^2}$, has emerged, and that this is tunable through ϵ_c. This means that even when $\eta \simeq 0$, as is typically the case on a microwave transition owing to the long wavelength, we have $|\eta_{\text{eff}}| \approx \epsilon_c$. Sideband transitions are still feasible when ϵ_c takes on non-negligible values. In the following, we shall consider a method for achieving non-zero values of ϵ_c.

Optical AC Stark shift gradient

For the rotational levels of molecular ions, a large effective LDP can be achieved using a spatially varying laser field according to Eq. 7.16, provided the dynamic polarizabilities at the laser frequency of the two rotational states are sufficiently different. Calculations as well as data for the dynamic polarizability of molecular ions are scarce in the literature. Neutral molecules, however, have been studied in much greater detail and in particular the alkali dimers such as KRb and RbCs [KT06, KD10]. Experiments with these molecules typically seek to achieve confinement in optical dipole traps using far off-resonant lasers, which may induce significant AC Stark shifts, also on the rotational states. For this reason, there have been strong efforts to find so-called *magic* wavelengths of the trapping laser, where the differential Stark shift

between the $|\downarrow\rangle_S$ and the $|\uparrow\rangle_S$ states is zero. While our goal here is precisely the opposite, we may still rely on the quantitative analysis from these works in evaluating the feasibility of our technique.

For the purpose of providing an order of magnitude estimate of the electric field gradient needed to achieve our proposed scheme, we approximate the dynamic polarizability of $SrCl^+$ by that of KRb. We further justify this simplification in our estimate by noting that, despite the difference in atomic species, the values obtained for KRb and RbCs are of the same order of magnitude [KT06, KD10]. By the same reasoning, we would expect similar behavior for the $SrCl^+$ molecular ion.

Based on the value for the difference in polarizability of the $|0\rangle_S$ and $|1\rangle_S$ states, $\Delta\alpha_{01}$, for KRb reported in, e.g., Ref. [KD10], we give an estimate for $SrCl^+$ of $\Delta\alpha_{01} \sim 1000$ a.u., where 1 a.u. $\sim 4.7 \times 10^{-8}$ MHz/(W/cm^2). We note that the calculations of Ref. [KD10] were performed for a wide spectrum of wavelengths from the visible and into the IR and that $\Delta\alpha_{01}$ is expected to be fairly constant across this range apart from regions around electronic resonances. This suggests that one can rely on wavelengths around 1 μm or 1.5 μm where high-power, stable sources are commercially available.

The change in energy due to the AC Stark shift is given by $\Delta E(z) = \hbar\Delta\alpha_{01} I(z)$, where $I(z)$ denotes the intensity of the laser used to create this spatially varying AC Stark shift. We consider both a standing wave laser field along the z-axis as well as a traveling wave laser field propagating perpendicular to the z-axis and focused to a tight waist, w_0. In the former case $I(z) = I_0 \sin^2(k_{ac} z + \phi_{ac})$, where k_{ac} and ϕ_{ac} denote the wave number and phase constant, respectively. In the latter $I(z) = I_0 e^{-(z-z_0)^2/w_0^2}$. In both cases the peak intensity is $I_0 = \frac{2P}{\pi w_0^2}$, with the P being the total power in the beam, and w_0 being the beam waist. In both cases we assume that the molecular ion is positioned at the point of steepest optical gradient, corresponding to $\phi = \frac{\pi}{4}$ and $z_0 = w_0$ in the standing and traveling wave cases, respectively. We furthermore assume that the wavepacket size is small compared to the optical wavelength (Lamb-Dicke regime), which motivates an expansion around $z = 0$ to get:

$$\Delta E(z) = \begin{cases} \hbar\Delta\alpha_{01} I_0 \left(\frac{1}{2} + kz\right), & \text{standing wave,} \\ \hbar\Delta\alpha_{01} I_0 e^{-1} \left(1 - \frac{2z}{w_0}\right), & \text{traveling wave.} \end{cases} \tag{7.24}$$

Using $z = \sigma_0(a + a^\dagger)$, the expression for the effective LDP can be found to be

$$|\eta_{\text{eff}}| \approx \epsilon_c = \begin{cases} \frac{\Delta\alpha_{01}}{\omega_t} k\sigma_0 \times I_0, & \text{standing wave,} \\ \frac{\Delta\alpha_{01}}{\omega_t} e^{-1} \frac{2\sigma_0}{w_0} \times I_0, & \text{traveling wave.} \end{cases} \tag{7.25}$$

The standing wave configuration can be realized either by retro-reflecting the laser beam off a single mirror or by using an optical cavity. Figure 7.2.2 (a) plots the effective LDP for three different experimental scenarios, namely, a tightly focused laser beam, a retro-reflected, moderately tight focused laser beam, and a loosely focused cavity beam, all with wavelength $\lambda = 1$ μm. For each scenario, the focusing is chosen to allow for an effective LDP in the $10^{-2} - 10^{-1}$ range with reasonable power level and the figure thus represents the compromise between complexity of the experiment and the available power. The example is based on $SrCl^+$ confined in a trap with a trap frequency, $\omega_t/2\pi = 1$ MHz and $\Delta\alpha_{01} \sim 1000$ a.u.. The value used for the difference in polarizability was estimated from that of the neutral alkali dimer KRb [KD10]. While we don't believe it to be significantly different from that of $SrCl^+$, even if it was lower by an order of magnitude, the linear scaling with this parameter, means that an effective LDP at the percent-level is still feasible with the parameters used in the above example.

It is clear that an appreciable LDP can be achieved. Even larger values of ϵ_c could be achieved without going to higher power levels by lowering the trap frequency [PD12], which would increase σ_0 accordingly. Ultimately, the trap frequency is expected to be constrained by the requirement of the atomic ion remaining in the Lamb-Dicke regime in order to obtain efficient sideband operations. Recently, however, sideband cooling to the ground state was demonstrated at trap frequencies lower than 300 kHz [PMD12].

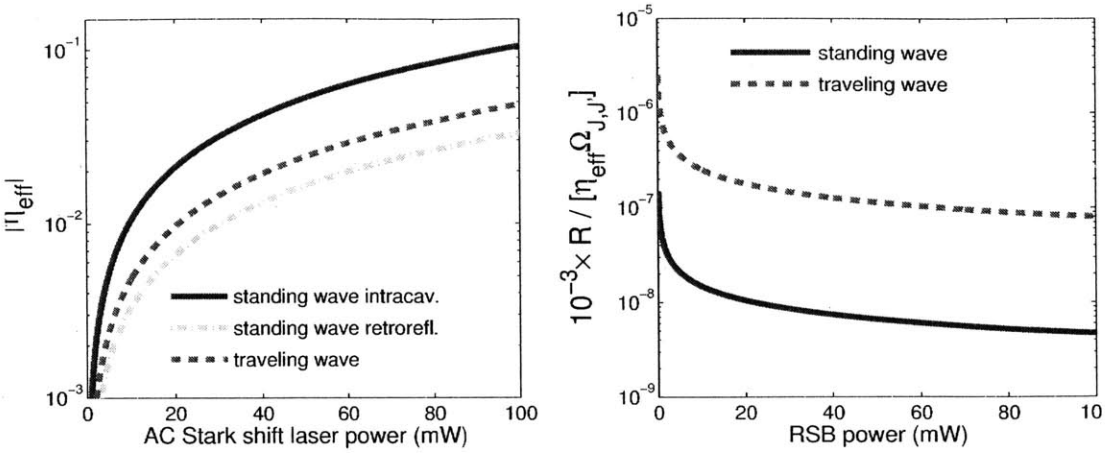

Figure 7-2: (a) Effective LDP produced by spatially varying laser field for three different scenarios, all at wavelength $\lambda = 1$ μm. Red: focused laser beam, $w_0 = 2$ μm. Green: retro-reflected laser beam, $w_0 = 20$ μm. Blue: Cavity laser beam, $w_0 = 100$ μm, cavity finesse, $F = 1000$. (b) Estimate of spontaneous-Raman-rate-to-Rabi-frequency ratio. Raman scattering rate is estimated using $10^{-3}\times$ Rayleigh rate, for travelling and standing waves, both at wavelength $\lambda = 1$ μm.

7.2.3 Decoherence induced by off-resonance laser field

We have shown that an effective LDP can be achieved by coupling the trapped molecule with an off-resonant laser field. However, the increase in effective LDP with the laser intensity, as captured by Figure 7.2.2 (a), is accompanied by an increase in the scattering rate of the molecule. In this respect, the spontaneous Raman scattering rate is of particular relevance as it leads to a new decoherence mechanism, which might affect our experiment feasibility. As the Raman scattering results from effective LDP generation, which can be switched off during other steps of the experiment, we only needs to compare its time scale with that of the sideband transition. That is, the following inequality needs to be fulfilled (c.f. Eq. 7.5):

$$\frac{\pi}{\eta_{\text{eff}}\Omega_S} \ll \frac{1}{R \times 10^{-3}}, \tag{7.26}$$

where on the right side of Eq.7.26, we gauged the Raman scattering via the Rayleigh scattering rate R, which is typically three orders of magnitude higher than the for-

mer [Lon77], and can be estimated simply from knowledge of the polarizability, α, alone [CTDRG92]:

$$R = \frac{2\pi\hbar\omega_{ac}^3\alpha^2}{3c^2} \times I_0, \tag{7.27}$$

where ω_{ac} is the frequency of the laser used to create the spatially varying AC Stark shift, and α is the rotational state polarizability of the molecular ion, which is measured, for consistency in atomic unit [KD10], with 1 a.u. $\sim 4.7\times10^{-8}$ MHz/(W/cm^2). The linear dependence on intensity, I_0, similarly to the expression for ϵ_c in 7.25, suggests that the optimal intensity is determined by the microwave Rabi frequency Ω_S. The ratio $\frac{R\times10^{-3}}{\eta_{\text{eff}}\Omega_S}$ is plotted in Figure 7.2.2 (b), where again, due to the lack of knowledge of α's of all states of $SrCl^+$, we give an order-of-magnitude estimate based on the ground-state polarizability $\alpha = 1000$ a.u. of KRb in Ref. [KD10]. Based on this estimate, it is clear that, even at conservative microwave power, the ratio of Raman decoherence rate to the Rabi frequency can be made as low as 10^{-5}. This suggests that Raman scattering should not present a major obstacle to our experimental protocol.

7.3 Conclusions and discussion

In summary, we show that in the framework of quantum logic spectroscopy, rotational spectroscopy can be implemented for trapped polar molecular ions. Direct microwave addressing can be achieved via an effective Lamb-Dicke parameter on the order of $\sim$0.1, induced by a spatially varying AC Stark shift. Although the ground state cooling and state detection scheme we propose naturally leads to the QIP architecture with qubits encoded in the molecular rotational states, the same techniques can be generalized to those encoded in the hyperfine structure (HFS) sublevels of a single rotational state. These HFS-encoded states are much more robust to stray electric field fluctuations, and hence can have a much longer coherence time (typically on the order of 10 s) [SBC+11]. The cotrapped atomic-molecular-ion system can be used as a hybrid quantum information processor, where fast gate operations with atomic ions and long-lived quantum memories with molecular ions can both be exploited.

Chapter 8

Conclusion and future work

In this thesis, we have studied trapped atomic and molecular ions, for their applications in quantum information science. One one hand, while precise laser control and manipulation allows for high fidelity gate implementation for atomic ions, it can be quite challenging to implement cavity QED for single ions in the optical regime for quantum network construction. On the other hand, although microwave cavity QED systems can be envisioned for polar molecular ions for a compact and scalable quantum network model, the lack of suitable closed transition makes it difficult to perform reliable spectroscopy and detection with molecules. This thesis thus aimed to investigate along this line of thought, new experimental approaches for single ion cavity QED, and rotational state spectroscopy for atomic and molecular ions, respectively.

For single ion cavity QED, because high finesse cavities with close distance between ions and cavity mirrors are required to reach strong coupling in a stable cavity mode, two major challenges are considered and addressed, respectively in this thesis.

In Chapter 3 and Chapter 4, cavity designs with axis oriented orthogonal to a planar trap is presented. While a central aperture on the trap allows the ion to interact with the cavity mode, the stray electric field noise can be shielded by the trap electrode from the ion. Chapter 3 explores further experiment capabilities of the system such as quantum memory for photon number states with multiple ions in the cavity. Chapter 4 focused on the detailed system design and implementation.

In Chapter 5, a study on the cavity finesse change over time is studied. The mechanism of cavity finesse decay is explored, and methods of preventing finesse decay as well as recovering decay in-situ are presented.

For molecular ion rotational spectroscopy, quantum logic spectroscopy is proposed in Chapter 6 and Chapter 7. By entangling cotrapped single molecular and atomic ions, cooling, spectroscopy, and readout for the molecular ion states can all be facilitated via the atomic ion. While Chapter 6 considers a general experimental protocol for quantum system lacking proper transitions like molecular rotations, Chapter 7 studies the challenges of experimental implementation. In particular, in the microwave regime, the challenges to realize entanglement with inefficient coupling between molecule and phonon bus is addressed with the assistance of photon resonator.

The investigations into these two directions allow us to discover new areas where the proposed experimental techniques can apply, and new questions we can investigate with the implemented experimental apparatus.

The methods proposed in Chapter 7 to efficiently couple microwave transitions to a phonon bus can be applied not only to rotational states of molecule, but all qubits involving microwave transitions, such as the magnetic sublevels of atomic ions. This allows for trap-integrated microwave to facilitate both qubit transitions and resolved sideband cooling, and hence simply the dedicated laser system.

In Chapter 5, the fact that the cavity finesse can recover with 422 nm illumination in oxygen implies that electric field field can alter the relative potential depth for oxygen in O_2 and Ta_2O_5. This also suggest that with continuous laser illumination, the the finesse decay can be suppressed in vacuum. Furthermore, the dependence of frequency and illumination power can be investigated for a detailed study of color center spectrum.

Appendix A

Characterization of Fabry-Pérot cavities

In this section we describe in detail the three techniques used in this thesis to characterize Fabry-Pérot cavities: Lorentzian mapping (Chapter4), free decay (Chapter 5) and ring down spectroscopy. In all approaches, the cavity transmission signal of an incident laser beam is measured, the frequency of which is close to the cavity resonance. For a cavity composed of two mirrors with field transmission, reflection, and scattering loss coefficient $t_{1,2}$, $r_{1,2}$ and $l_{1,2}$, the cavity field transmittance $\mathcal{T}$ follows:

$$\mathcal{T} = \left| \frac{t_1 t_2 e^{i\phi}}{1 - e^{2i\phi} r_1 r_2} \right|^2, \tag{A.1}$$

where $\phi \equiv \omega L/c$ is the field phase accumulated over the cavity length L. c is the speed of light in vacuum. The single mirror field coefficients $t_{1,2}$, $r_{1,2}$, $l_{1,2}$ and intensity coefficients $\mathcal{T}_{1,2}$, $\mathcal{R}_{1,2}$, $\mathcal{L}_{1,2}$ are related by their modulo squares:

$$\mathcal{T}_{1,2} = |t_{1,2}|^2, \quad \mathcal{R}_{1,2} = |r_{1,2}|^2, \quad \mathcal{L}_{1,2} = |l_{1,2}|^2, \tag{A.2}$$

which follow

$$\mathcal{T}_{1,2} + \mathcal{R}_{1,2} + \mathcal{L}_{1,2} = |t_{1,2}|^2 + |r_{1,2}|^2 + |l_{1,2}|^2 = 1. \tag{A.3}$$

Equation A.1 can be simplified to

$$\mathcal{T} = \frac{|t_1^2||t_2^2|}{(1 - r_1 r_2)^2 + 4 r_1 r_2 \sin^2 \phi} \tag{A.4}$$

Eq. A.4 manifests the periodic property of the transmittance spectrum, with a periodicity $f = FSR \equiv 2L/c$, which is referred as the free spectrum range of the cavity. For high reflectivity mirrors, $t_{1,2}^2/r_{1,2}^2$ and $l_{1,2}^2/r_{1,2}^2$ are both close zero. Therefore Eq. A.4 vanishes except at around the resonances where $\sin\phi = 0$. We thus expand $\sin\phi \sim \phi$, which gives a Lorentzian form of the transmittance spectrum near the resonances:

$$\mathcal{T} = \frac{|t_1^2||t_2^2|}{(1 - r_1 r_2)^2 + 4 r_1 r_2 \phi^2} = \frac{|t_1^2||t_2^2|}{(1 - r_1 r_2)^2 + 4 r_1 r_2 (L/c)^2 \omega^2}, \tag{A.5}$$

for which the FWHM, in the lowest order of $t_{1,2}$ and $l_{1,2}$, follows

$$2\pi \times FWHM = 2\pi \frac{c}{2L} \frac{|t_1|^2 + |t_1|^2 + |l_1|^2 + |l_1|^2}{2\pi} = 2\pi \frac{c}{2L} \frac{\mathcal{T}_1 + \mathcal{T}_2 + \mathcal{L}_1 + \mathcal{L}_2}{2\pi} \tag{A.6}$$

A unit free parameter that measures the resonator quality of a Fabry-Pérot cavity is the finesse $\mathcal{F}$, defined as

$$\mathcal{F} = \frac{FSR}{FWHM}, \tag{A.7}$$

which following our derivation above can also be written in the form

$$\mathcal{F} = \frac{2\pi}{\mathcal{T}_1 + \mathcal{T}_2 + \mathcal{L}_1 + \mathcal{L}_2}. \tag{A.8}$$

Eq. A.1 (and all the derived relations above) is the solution of Maxwell Equations in the frequency domain. In the time domain, the intracavity and transmission fields respond to the incident drive in an exponential form with a time constant

$$\tau_c = \kappa^{-1} = [2\pi \times FWHM]^{-1} = L/c\pi \cdot \mathcal{F}, \tag{A.9}$$

following the inverse Fourier transform of the Eq. A.5.

To obtain the finesse or equivalently, the loss of a cavity, several techniques can

be used.

A.1 Lorentzian mapping

One can scan either the laser frequency ω or the cavity length L at a linear rate around the resonances, and map out the Lorentizan profile of Eq. A.5. To calibrate the scan rate[1], a frequency modulation via an EOM is typically applied to the laser frequency to provide sidebands around the transmittance peaks[2]. This technique requires the scanning rate τ_{sc}^{-1} to be slow enough to allow the fields to relax to equilibrium, and fast enough so the cavity is mechanically stable during the scan. That is,

$$\tau_{mch}^{-1} \ll \tau_{sc}^{-1} \ll \tau_{c}^{-1}, \tag{A.10}$$

where $\tau_{mch}^{-1} = \omega_{mch}/2\pi$ is the highest mechanical normal mode frequency of the cavity assembly, which can sometimes be close to 100 kHz. This technique is therefore used for cavities with $\tau_c^{-1} > 10$ MHz. For cavities with longer cavity relaxation time, finding a desired scanning rate can be difficult. Furthermore, this method requires the incident laser to have a negligible linewidth. Otherwise the resultant spectrum is a convolution between the two Lorentzian profiles. Unless the laser linewidth is well-calibrated, systematic errors are added to the measurement.

A.2 Free decay spectroscopy

Unlike direct Lorentzian spectrum mapping, the free decay and ring down spectroscopy measures the cavity transient response, which we describe in this and next section, respectively.

[1] The FWHM's of high finesse cavities are typically on the order of a few MHz, which hit the resolution limit (10MHz) of most wave meters for laboratory use. A wider frequency scan typically result in less sampling within the resonance peaks, giving undesirable SNR's

[2] The mathematical details can be found in Ref. [Bla01]

The free decay spectroscopy measures the cavity transmission when the incident laser is switched off adiabatically, i.e. at a rate much faster than τ_c^{-1}. The transmitted intensity thus follows

$$I(t) = I_0 e^{-t/\tau_c}, \tag{A.11}$$

where I_0 is the field intensity measured at the incidence the laser is switched off. The cavity relaxation constant τ_c can thus be obtained by fitting the exponential decay. Compared to direct spectrum mapping, the cavity free decay measurement does not require a frequency scanning rate satisfying Eq. A.10, so long as $\tau_{mch}^{-1} \ll \tau_c^{-1}$. Because no scan is involved in the measurement, the laser line width does not add complexity to the experiment. Nonetheless, detectors (e.g. APD's) and laser-switching (via AOM or direct laser current switching) must be faster than the cavity decay rate τ_c.

A.3 Ring down spectroscopy

The cavity ring down spectroscopy measures the cavity transmission signal when the laser frequency or cavity length is scanned at a comparable rate with τ_c^{-1}. According to Ref. [PBVL97], in the case of scanning cavity length, the spectrum of decay follows

$$\mathcal{T} = A\frac{\mathcal{T}_1\mathcal{T}_2}{4\mathcal{R}_1\mathcal{R}_2}\frac{\pi FSR^2}{a}e^{-\kappa(t-t_0)}\left|1 - \mathrm{erfz}\left[\frac{1-i}{2\sqrt{2}}\left(\frac{\pi FSR}{\mathcal{F}\sqrt{a}} - 2\sqrt{a}(t-t_0)\right)\right]\right|^2 + B, \tag{A.12}$$

where A, B and t_0 are scaling factors. a is the frequency scanning speed, which has unit s^{-2}. the function erfz is the generalized error function for complex numbers. In contrast to slow scans where the cavity transmission is always in equilibrium, or fast laser laser switching so the cavity responds adiabatically, in the intermediate regime, the transmission signal has two unique features: (i) a decay tail $e^{-\kappa(t-t_0)}$ that captures the drive field cut-off since the incident laser has moved out of resonance, and (ii) interference fringes captured by the error function, since the circulating fields exit the cavity with different phases.

Appendix B

Separation of molecular rotational dynamics from full Hamiltonian

We consider the dynamics of a diatomic molecule, and under reasonable approximations, aim to reduce its rotational motion from the full nuclear motion Hamiltonian, which as a whole will be separated from that of the electrons.

B.1 Born-Oppenheimer approximation

The treatment of nuclear dynamics in separation with the electrons comes from the Born-Oppenheimer approximation, which is formulated in three steps to solve the full molecular dynamics, described by the Hamiltonian $\mathcal{H}(\mathbf{r}_i, \mathbf{R}_\alpha)$ for wave function $\psi_E(\mathbf{r}_i, \mathbf{R}_\alpha)$ with eigen energy E:

$$\mathcal{H}(\mathbf{r}_i, \mathbf{R}_\alpha)\psi_E(\mathbf{r}_i, \mathbf{R}_\alpha) = E\psi_E(\mathbf{r}_i, \mathbf{R}_\alpha), \tag{B.1}$$

where $\mathbf{r}_i$ and $\mathbf{R}_\alpha$ index the coordinates of the i^{th} electron and α^{th} nucleus of the molecule, respectively.

The first step is to consider the nuclei as infinitely massive as compared to the electrons, and hence fixed in position $\mathbf{R}_\alpha$. Then the electron dynamics follows that of

the nuclei, and evolves adiabatically. The $\mathcal{H}(\mathbf{r}_i, \mathbf{R}_\alpha)$ reduces to the so-called electronic Hamiltonian:

$$\mathcal{H}^e(\mathbf{r}_i, \mathbf{R}_\alpha) \equiv T_e(\mathbf{r}_i) + V_{ee}(\mathbf{r}_i) + V_{en}(\mathbf{r}_i, \mathbf{R}_\alpha), \tag{B.2}$$

with $T_e(\mathbf{r}_i)$, $V_{ee}(\mathbf{r}_i)$, and $V_{en}(\mathbf{r}_i, \mathbf{R}_\alpha)$ describing the energies due to electronic kinetic motion, electron-electron interaction, and electron nuclear interaction, respectively. The corresponding electronic Schrödinger Equation is then solved for the energy levels $E^e_\xi(\mathbf{R}_\alpha)$ and eigen states $\psi^e_\xi(\mathbf{r}_i, \mathbf{R}_\alpha)$ following

$$\mathcal{H}^e(\mathbf{r}_i, \mathbf{R}_\alpha)\psi^e_\xi(\mathbf{r}_i, \mathbf{R}_\alpha) = E^e_\xi \psi^e_\xi(\mathbf{r}_i, \mathbf{R}_\alpha), \tag{B.3}$$

where ξ is used to index the set of quantum numbers for the eigen states.

Step two in the formalism then involves the solution of the nuclear motions. For each electronic eigen states solved in the previous step, the nulcear Schrödinger equation follows

$$\mathcal{H}^n(\mathbf{R}_\alpha)\psi^n_{\xi\nu}(\mathbf{R}_\alpha) = E_{\xi\nu}\psi^n_{\xi\nu}(\mathbf{R}_\alpha), \tag{B.4}$$

where

$$\mathcal{H}^n(\mathbf{R}_\alpha) \equiv T_n(\mathbf{R}_\alpha) + V_{nn}(\mathbf{R}_\alpha) + E^e_\xi(\mathbf{R}_\alpha). \tag{B.5}$$

$T_n(\mathbf{R}_\alpha)$ and $V_{nn}(\mathbf{R}_\alpha)$ denote the nuclear kinetic and interaction energies, respectively. $E_{\xi\nu}$ denotes the eigen energy in Eq. B.1, with ξ and ν indexing the quantum numbers for electron and nuclear motion, respectively.

Finally in last step of Born-Oppenheimer approximation, the total wave function for the full molecular dynamics is combined, resulting in

$$\psi_{\xi\nu}(\mathbf{r}_i, \mathbf{R}_\alpha) = \psi^e_\xi(\mathbf{r}_i, \mathbf{R}_\alpha)\psi^n_{\xi\nu}(\mathbf{R}_\alpha). \tag{B.6}$$

Since we are interested in the nuclear motion, we focus on further decomposing Eq. B.4 in the next section. In particular, we focus our derivation for the electronic ground state, which for most diatomic molecules is in a $^1\Sigma$ configuration [BC03, GC84, MAML76]. Electronic angular momentum in such case vanishes, meaning no

magnetic dipole interactions in V_{en} needs to be considered in Eq. B.2.

B.2 Nuclear motion

The kinetic part of nuclear Hamiltonian $T_n(\mathbf{R}_\alpha)$ in Eq. B.4 can be decomposed to that of the center of motion $T_{n_c}(\mathbf{R}_c)$ and that of the molecular relative motion $T_{n_r}(\mathbf{R}_r)$, resulting in

$$\mathcal{H}^n(\mathbf{R}_\alpha) = T_{n_c}(\mathbf{R}_c) + T_{n_r}(\mathbf{R}_r) + V_{nn}(\mathbf{R}_r) + E^e_\xi(\mathbf{R}_r) = T_{n_c}(\mathbf{R}_c) + \mathcal{H}^n_r(\mathbf{R}_r), \quad \text{(B.7)}$$

with the relative motion Hamiltonian $\mathcal{H}^n_r(\mathbf{R}_r)$ defined as

$$\mathcal{H}^n_r(\mathbf{R}_r) \equiv T_{n_r}(\mathbf{R}_r) + V_{nn}(\mathbf{R}_r) + E^e_\xi(\mathbf{R}_r) \quad \text{(B.8)}$$

where with two explicit indices in the nuclear coordinates $\mathbf{R}_\alpha \equiv \mathbf{R}_a, \mathbf{R}_b$, we defined the center of mass and relative coordinate $\mathbf{R}_c$ and $\mathbf{R}_r$ respectively as

$$\mathbf{R}_c = (\mathbf{R}_a + \mathbf{R}_b)/2, \quad \text{(B.9)}$$

$$\mathbf{R}_r = \mathbf{R}_b - \mathbf{R}_a. \quad \text{(B.10)}$$

This separation then manifests a wave function $\psi^n_{\xi\nu}(\mathbf{R}_\alpha)$ of the from

$$\psi^n_{\xi\nu}(\mathbf{R}_\alpha) = \psi^{n_c}_{\xi\nu}(\mathbf{R}_c)\psi^{n_r}_{\xi\nu}(\mathbf{R}_\alpha) \quad \text{(B.11)}$$

The kinetic part of the relative motion Hamiltonian $T_{n_r}(\mathbf{R}_r)$ can be expressed explicitly in spherical coordinates:

$$T_{n_r}(\mathbf{R}_r) = -\frac{\hbar^2}{2\mu}\nabla^2_{R_r} + \frac{1}{2}\frac{\mathbf{L}^2}{\mu R_r^2}, \quad \text{(B.12)}$$

where in the first term, $R_r = |\mathbf{R}_r|$, and μ is the reduced mass of the diatomic molecule,

with $\mu = \mu_a\mu_b/(\mu_a + \mu_b)$. The rotational kinetics is described by the second term. $\mathbf{L}^2$ is the total angular momentum operator (see, e.g. Eq. 2.18 in [MAML76]).

B.3 Rotational states

A so-called rigid rotor approximation is usually made in order to further separate the rotational motion from Eq. B.12. Assuming the inter-nuclei distance R_r is fixed (take its equilibrium distance as R_0), the rotational motion described in Eq. B.12 can thus be decoupled from the radial (vibrational) motion, and reduces to

$$\mathcal{H}_{\rm rot}(\theta,\phi) = \frac{1}{2}\frac{\mathbf{L}^2}{\mu R_0^2} = \frac{\mathbf{L}^2}{2I_0}, \tag{B.13}$$

where $I_0 = \mu R_0^2$ is the moment of inertia of the rotor. The eigen states of Eq. B.13 are the spherical harmonics $Y_{J,m_J}(\theta,\phi)$, where J and m_J are the angular momentum and magnetic quantum numbers of the rotational motion, respectively, and the energy levels follow

$$\mathcal{H}_{\rm rot}Y_{J,m_J}(\theta,\phi) = E_J^{\rm rot}Y_{J,m_J}(\theta,\phi), \tag{B.14}$$

where $E_J^{\rm rot} \equiv \hbar C \equiv \hbar\cdot\frac{\hbar}{2I_0}J(J+1)$. The constant C is usually referred as the rotational constant of molecules.

Bibliography

[ADD+06] A. André, D. DeMille, J. M. Doyle, M. D. Lukin, S. E. Maxwell, P. Rabl, R. J. Schoelkopf, and P. Zoller. A coherent all-electrical interface between polar molecules and mesoscopic superconducting resonators. *Nature Physics*, 2(9):636–642, August 2006.

[ALB+07] Marco Anderlini, Patricia J Lee, Benjamin L Brown, Jennifer Sebby-Strabley, William D Phillips, and J V Porto. Controlled exchange interaction between pairs of neutral atoms in an optical lattice. *Nature*, 448(7152):452–6, July 2007.

[AMK+08] J. Alnis, A. Matveev, N. Kolachevsky, Th. Udem, and T. W. Hänsch. Subhertz linewidth diode lasers by stabilization to vibrationally and thermally compensated ultralow-expansion glass Fabry-Pérot cavities. *Physical Review A*, 77(5):053809, May 2008.

[Ant11] Paul B. Antohi. *Cryogenic Surface Electrode Ion Traps with Integrated Superconducting Microwave Resonators for Polar Molecular Ion Spectroscopy.* PhD thesis, MIT, Department of Physics, 2011.

[ASA+09] P B Antohi, D Schuster, G M Akselrod, J Labaziewicz, Y Ge, Z Lin, W S Bakr, and I L Chuang. Cryogenic ion trapping systems with surface-electrode traps. *The Review of scientific instruments*, 80(1):013103, January 2009.

[Bar03] Vladimir I Baranov. Analytical approach for description of ion motion in quadrupole mass spectrometer. *Journal of the American Society for Mass Spectrometry*, 14(8):818–24, August 2003.

[BB14] Charles H. Bennett and Gilles Brassard. Quantum cryptography: Public key distribution and coin tossing. *Theoretical Computer Science*, 560:7–11, December 2014.

[BBC+93] Charles H. Bennett, Gilles Brassard, Claude Crépeau, Richard Jozsa, Asher Peres, and William K. Wootters. Teleporting an unknown quantum state via dual classical and Einstein-Podolsky-Rosen channels. *Physical Review Letters*, 70(13):1895–1899, March 1993.

[BC03] John M. Brown and Alan Carrington. *Rotational Spectroscopy of Diatomic Molecules*. Cambridge University Press, 2003.

[BCJD99] Gavin K. Brennen, Carlton M. Caves, Poul S. Jessen, and Ivan H. Deutsch. Quantum Logic Gates in Optical Lattices. *Physical Review Letters*, 82(5):1060–1063, February 1999.

[BHLL14] C. J. Ballance, T. P. Harty, N. M. Linke, and D. M. Lucas. High-fidelity two-qubit quantum logic gates using trapped calcium-43 ions. *arXiv:1406.5473*, June 2014.

[BJD06] Anders Bertelsen, Solvejg Jørgensen, and Michael Drewsen. The rotational temperature of polar molecular ions in Coulomb crystals. *J. Phys. B: At. Mol. Opt. Phys.*, 39(5):L83–L89, March 2006.

[BKB+11] K Beloy, M G Kozlov, A Borschevsky, A W Hauser, V V Flambaum, and P Schwerdtfeger. Rotational spectrum of the molecular ion NH^+ as a probe for α and m_e/m_p variation. *Phys. Rev. A*, 83(6):062514, June 2011.

[Bla01] E D Black. An introduction to Pound-Drever-Hall laser frequency stabilization. *American Journal Of Physics*, 69(1):79–87, January 2001.

[BLS+10] D. Bozyigit, C. Lang, L. Steffen, J. M. Fink, C. Eichler, M. Baur, R. Bianchetti, P. J. Leek, S. Filipp, M. P. da Silva, A. Blais, and A. Wallraff. Antibunching of microwave-frequency photons observed in correlation measurements using linear detectors. *Nature Physics*, 7(2):154–158, December 2010.

[BMS+13] B Brandstätter, A McClung, K Schüppert, B Casabone, K Friebe, A Stute, P O Schmidt, C Deutsch, J Reichel, R Blatt, and T E Northup. Integrated fiber-mirror ion trap for strong ion-cavity coupling. *The Review of scientific instruments*, 84(12):123104, December 2013.

[BW08] R Blatt and D Wineland. Entangled states of trapped atomic ions. *Nature*, 453(7198):1008–1015, June 2008.

[BZ01] Ian W. Boyd and Jun-Ying Zhang. Photo-induced growth of dielectrics with excimer lamps. *Solid-State Electronics*, 45(8):1413–1431, August 2001.

[CBB+05] J Chiaverini, R B Blakestad, J Britton, J D Jost, C Langer, D Leibfried, R Ozeri, and D J Wineland. Surface-electrode architecture for ion-trap quantum information processing. *Quantum Inf. Comput.*, 5(6):419–439, September 2005.

[CBK+13] Marko Cetina, Alexei Bylinskii, Leon Karpa, Dorian Gangloff, Kristin M Beck, Yufei Ge, Matthias Scholz, Andrew T Grier, Isaac Chuang, and Vladan Vuletić. One-dimensional array of ion chains coupled to an optical cavity. *New Journal of Physics*, 15(5):053001, May 2013.

[CCS93] Sylvio Canuto, Marcos A Castro, and K Sinha. Theoretical determination of the spectroscopic constants of CaH^+. *Phys. Rev. A*, 48(3):2461–2463, September 1993.

[CEHM99] J. I. Cirac, A. K. Ekert, S. F. Huelga, and C. Macchiavello. Distributed quantum computation over noisy channels. *Physical Review A*, 59(6):4249–4254, June 1999.

[Cet11] Marko Cetina. *Hybrid Approaches to Quantum Information Using Ions, Atom and Photons.* PhD thesis, MIT, Department of Physics, 2011.

[CGD+10] Craig R. Clark, James E. Goeders, Yatis K. Dodia, C. Ricardo Viteri, and Kenneth R. Brown. Detection of single-ion spectra by Coulomb-crystal heating. *Phys. Rev. A*, 81(4):043428, April 2010.

[Chu36] A. Church. An unsolvable problem of elementary number theory. *Am. J. Math*, 58:345, 1936.

[CMBK14] S. Crain, E. Mount, S. Baek, and J. Kim. Individual addressing of trapped $^{171}Yb^{+}$ ion qubits using a microelectromechanical systems-based beam steering system. *Applied Physics Letters*, 105(18):181115, November 2014.

[CSF+13] B. Casabone, A. Stute, K. Friebe, B. Brandstätter, K. Schüppert, R. Blatt, and T. E. Northup. Heralded Entanglement of Two Ions in an Optical Cavity. *Physical Review Letters*, 111(10):100505, September 2013.

[CSK+11] Kuang Chen, Steven J Schowalter, Svetlana Kotochigova, Alexander Petrov, Wade G Rellergert, Scott T Sullivan, and Eric R Hudson. Molecular-ion trap-depletion spectroscopy of $BaCl^{+}$. *Phys. Rev. A*, 83(3):030501, March 2011.

[CT92] C Cohen-Tannoudji. *Atomic motion in laser light.* Elsevier Science Publishers B.V., North-Holland, 1992.

[CTDRG92] C Cohen-Tannoudji, J Dupont-Roc, and G Grynbergt. *Atom-photon interactions.* John Wiley & Sons, Inc., New York, 1992.

[CY95] Isaac L. Chuang and Yoshihisa Yamamoto. Simple quantum computer. *Physical Review A*, 52(5):3489–3496, November 1995.

[CY09] Lincoln D Carr and Jun Ye. Focus on cold and ultracold molecules. *New J. Phys.*, 11(5):055009, 2009.

[CZ95] J I Cirac and P Zoller. Quantum Computations With Cold Trapped Ions. *Phys. Rev. Lett.*, 74(20):4091–4094, May 1995.

[CZKM97] J. I. Cirac, P. Zoller, H. J. Kimble, and H. Mabuchi. Quantum State Transfer and Entanglement Distribution among Distant Nodes in a Quantum Network. *Physical Review Letters*, 78(16):3221–3224, April 1997.

[DBIW89] F Diedrich, J C Bergquist, W M Itano, and D J Wineland. Laser Cooling To The Zero-Point Energy Of Motion. *Phys. Rev. Lett.*, 62(4):403–406, January 1989.

[Deh82] Hans G. Dehmelt. Monoion oscillator as potential ultimate laser frequency standard. *IEEE Transactions on Instrumentation and Measurement*, IM-31(2):83–87, June 1982.

[DeM02] D DeMille. Quantum Computation with Trapped Polar Molecules. *Phys. Rev. Lett.*, 88(6):067901, January 2002.

[DiV00] D P DiVincenzo. The physical implementation of quantum computation. *Fortschritte Der Physik-Progress Of Physics*, 48(9-11):771–783, 2000.

[DLCZ01] L M Duan, M D Lukin, J I Cirac, and P Zoller. Long-distance quantum communication with atomic ensembles and linear optics. *Nature*, 414(6862):413–8, November 2001.

[DLMB12] Francisco Benito David L. Moehring, Jonathan D. Sterk and Matthew G. Blain. Ion-photon quantum interface: Entanglement engineering. Unlimited Release SAND2012-6138, Sandia National Laboratories, San-

dia National Laboratories Albuquerque, New Mexico 87185, September 2012.

[DM12] S Ding and D N Matsukevich. Quantum logic for the control and manipulation of molecular ions using a frequency comb. *New J. Phys.*, 14(2):023028, February 2012.

[DP04] A. Dantan and M. Pinard. Quantum-state transfer between fields and atoms in electromagnetically induced transparency. *Physical Review A*, 69(4):043810, April 2004.

[DSG85] H. Demiryont, James R. Sites, and Kent Geib. Effects of oxygen content on the optical properties of tantalum oxide films deposited by ion-beam sputtering. *Applied Optics*, 24(4):490, February 1985.

[DZM+96] A. M. De Riva, G. Zavattini, S. Marigo, C. Rizzo, G. Ruoso, G. Carugno, R. Onofrio, S. Carusotto, M. Papa, F. Perrone, E. Polacco, G. Cantatore, F. Della Valle, P. Micossi, E. Milotti, P. Pace, and E. Zavattini. Very high Q frequency-locked Fabry-Pérot cavity. *Review of Scientific Instruments*, 67(8):2680, August 1996.

[EMSKB03] Jürgen Eschner, Giovanna Morigi, Ferdinand Schmidt-Kaler, and Rainer Blatt. Laser cooling of trapped ions. *Journal of the Optical Society of America B*, 20(5):1003, May 2003.

[Fey48] R. P. Feynman. Simulating physics with computers. *Intl. J. Theor. Phys.*, 21:467, 1948.

[GALS07] Alexey V. Gorshkov, Axel André, Mikhail D. Lukin, and Anders S. Sørensen. Photon storage in Λ-type optically dense atomic media. III. Effects of inhomogeneous broadening. *Physical Review A*, 76(3):033806, September 2007.

[GC84] Walter Gordy and Robert L. Cook. *Microwave Molecular Spectra.* Wiley-Interscience, 1984.

[GC97] N. A. Gershenfeld and I. L. Chuang. Bulk Spin-Resonance Quantum Computation. *Science*, 275(5298):350–356, January 1997.

[GDS09] S M Girvin, M H Devoret, and R J Schoelkopf. Circuit QED and engineering charge-based superconducting qubits. *Physica Scripta*, T137(T137):014012, December 2009.

[Ge15] Yufei Ge. Microfabrication of surface electrode ion traps for quantum manipulation. Master's thesis, MIT, Department of Physics, 2015.

[Gro97] L K Grover. Quantum mechanics helps in searching for a needle in a haystack. *Phys. Rev. Lett.*, 79(2):325–328, July 1997.

[GZ04] C. W. Gardiner and P. Zoller. *Quantum noise.* Springer-Verlag, Berlin, 3rd ed. edition, 2004.

[HAB+14] T. P. Harty, D. T. C. Allcock, C. J. Ballance, L. Guidoni, H. A. Janacek, N. M. Linke, D. N. Stacey, and D. M. Lucas. High-Fidelity Preparation, Gates, Memory, and Readout of a Trapped-Ion Quantum Bit. *Physical Review Letters*, 113(22):220501, November 2014.

[Har13] Serge Haroche. Nobel Lecture: Controlling photons in a box and exploring the quantum to classical boundary. *Reviews of Modern Physics*, 85(3):1083–1102, July 2013.

[HDM+09] Peter F. Herskind, Aurélien Dantan, Joan P. Marler, Magnus Albert, and Michael Drewsen. Realization of collective strong coupling with ion Coulomb crystals in an optical cavity. *Nature Physics*, 5(7):494–498, June 2009.

[HHL09] Aram W. Harrow, Avinatan Hassidim, and Seth Lloyd. Quantum Algorithm for Linear Systems of Equations. *Physical Review Letters*, 103(15):150502, October 2009.

[HHR+05] H Häffner, W Hänsel, C F Roos, J Benhelm, D Chek-al kar, M Chwalla, T Körber, U D Raipol, M Riebe, P O Schmidt, C Becher, O Gühne, W Dür, and R Blatt. Scalable multiparticle entanglement of trapped ions. *Nature*, 438:643–646, 2005.

[HHS+09] K Højbjerre, A K Hansen, P S Skyt, P F Staanum, and M Drewsen. Rotational state resolved photodissociation spectroscopy of translationally and vibrationally cold MgH^+ ions: toward rotational cooling of molecular ions. *New J. Phys.*, 11(5):055026, 2009.

[HKY01] Christina J. Hood, H. J. Kimble, and Jun Ye. Characterization of high-finesse mirrors: Loss, phase shifts, and mode structure in an optical cavity. *Physical Review A*, 64(3):033804, August 2001.

[HOB+08] K Højbjerre, D Offenberg, C Z Bisgaard, H Stapelfeldt, P F Staanum, A Mortensen, and M Drewsen. Consecutive photodissociation of a single complex molecular ion. *Phys. Rev. A*, 77(3):030702, March 2008.

[Hom06] Jonathan Home. *Entanglement of Two Trapped-Ion Spin Qubits.* PhD thesis, Oxford University, Department of Physics, 2006.

[Hou08] M G House. Analytic model for electrostatic fields in surface-electrode ion traps. *Phys. Rev. A*, 78(3):33402, September 2008.

[HSC+10] D Hunger, T Steinmetz, Y Colombe, C Deutsch, T W Haench, and J Reichel. A fiber Fabry-Perot cavity with high finesse. *New J. Phys.*, 12(6):65038, 2010.

[HSG+07] A A Houck, D I Schuster, J M Gambetta, J A Schreier, B R Johnson, J M Chow, L Frunzio, J Majer, M H Devoret, S M Girvin, and R J Schoelkopf. Generating single microwave photons in a circuit. *Nature*, 449(7160):328–31, September 2007.

[HWS+11] Peter F Herskind, Shannon X Wang, Molu Shi, Yufei Ge, Marko Cetina, and Isaac L Chuang. Microfabricated surface ion trap on a high-finesse optical mirror. *Optics letters*, 36(16):3045–7, August 2011.

[Jam98] D.F.V. James. Quantum dynamics of cold trapped ions with application to quantum computation. *Applied Physics B: Lasers and Optics*, 66(2):181–190, February 1998.

[JC63] E.T. Jaynes and F.W. Cummings. Comparison of quantum and semiclassical radiation theories with application to the beam maser. *Proceedings of the IEEE*, 51(1):89–109, January 1963.

[JRH+10] B. R. Johnson, M. D. Reed, A. A. Houck, D. I. Schuster, Lev S. Bishop, E. Ginossar, J. M. Gambetta, L. DiCarlo, L. Frunzio, S. M. Girvin, and R. J. Schoelkopf. Quantum non-demolition detection of single microwave photons in a circuit. *Nature Physics*, 6(9):663–667, June 2010.

[KAE67] O Kubaschewski, C B Alcock, and A L Evans. *Metallurgical thermochemistry*. Oxford : Pergamon, 4th ed. edition, 1967.

[KD10] Svetlana Kotochigova and David DeMille. Electric-field-dependent dynamic polarizability and state-insensitive conditions for optical trapping of diatomic polar molecules. *Phys. Rev. A*, 82(6):063421, December 2010.

[Kha13] New Mechanism for Oxidation of Native Silicon Oxide. *The Journal of Physical Chemistry C*, 117(19):9819–9825, May 2013.

[KHG+12] T. Kessler, C. Hagemann, C. Grebing, T. Legero, U. Sterr, F. Riehle, M. J. Martin, L. Chen, and J. Ye. A sub-40-mHz-linewidth laser based on a silicon single-crystal optical cavity. *Nature Photonics*, 6(10):687–692, September 2012.

[Kim98] H. J. Kimble. Strong Interactions of Single Atoms and Photons in Cavity QED. *Physica Scripta*, T76(1):127, 1998.

[Kim08] H J Kimble. The quantum internet. *Nature*, 453(7198):1023–30, June 2008.

[Kim11] Tony Hyum Kim. An optical-fiber interface to a trapped-ion quantum computer. Master's thesis, MIT, Department of Electrical Engineering and Computer Science, 2011.

[KKC+12] S Korenblit, D Kafri, W C Campbell, R Islam, E E Edwards, Z-X Gong, G-D Lin, L-M Duan, J Kim, K Kim, and C Monroe. Quantum simulation of spin models on an arbitrary lattice with trapped ions. *New Journal of Physics*, 14(9):095024, September 2012.

[KMW02] D Kielpinski, C Monroe, and D J Wineland. Architecture for a large-scale ion-trap quantum computer. *Nature*, 417(6890):709–11, June 2002.

[KRG+03] A Kiraz, C Reese, B Gayral, Lidong Zhang, W V Schoenfeld, B D Gerardot, P M Petroff, E L Hu, and A Imamoglu. Cavity-quantum electrodynamics with quantum dots. *Journal of Optics B: Quantum and Semiclassical Optics*, 5(2):129–137, April 2003.

[KT06] S Kotochigova and E Tiesinga. Controlling polar molecules in optical lattices. *Phys. Rev. A*, 73(4):041405, April 2006.

[Lab08] Jaroslaw Labaziewicz. *High Fidelity Quantum Gates with Ions in Cryogenic Microfabricated Ion Traps.* PhD thesis, MIT, Department of Physics, 2008.

[LE96] C. K. Law and J. H. Eberly. Arbitrary Control of a Quantum Electromagnetic Field. *Physical Review Letters*, 76(7):1055–1058, February 1996.

[Lei09] David R. Leibrandt. *Integrated chips and optical cavities for trapped in quantum information processing.* PhD thesis, MIT, Department of Physics, 2009.

[Lei12] D Leibfried. Quantum state preparation and control of single molecular ions. *New J. Phys.*, 14(2):023029, February 2012.

[LGA+08] J Labaziewicz, Y F Ge, P Antohi, D Leibrandt, K R Brown, and I L Chuang. Suppression of heating rates in cryogenic surface-electrode ion traps. *Phys. Rev. Lett.*, 100(1):13001, January 2008.

[LLC+11] L. Lamata, D. R. Leibrandt, I. L. Chuang, J. I. Cirac, M. D. Lukin, V. Vuletić, and S. F. Yelin. Ion Crystal Transducer for Strong Coupling between Single Ions and Single Photons. *Physical Review Letters*, 107(3):030501, July 2011.

[Llo96] S. Lloyd. Universal Quantum Simulators. *Science*, 273(5278):1073–1078, August 1996.

[LLVC09] D R Leibrandt, J Labaziewicz, V Vuletic, and I L Chuang. Cavity Sideband Cooling of a Single Trapped Ion. *Phys. Rev. Lett.*, 103(10):103001, September 2009.

[Lon77] D. A. Long. *Raman Spectroscopy.* McGraw-Hill International Book Company, London, 1977.

[LST09] Alexander I. Lvovsky, Barry C. Sanders, and Wolfgang Tittel. Optical quantum memory. *Nature Photonics*, 3(12):706–714, December 2009.

[MAML76] Thomas L. Estle Michael A. Morrison and Neal F. Lane. *Quantum States of Atoms, Molecules, and Solids.* Prentice-Hall Inc., 1976.

[MBD06] Edmund R Meyer, John L Bohn, and Michael P Deskevich. Candidate molecular ions for an electron electric dipole moment experiment. *Phys. Rev. A*, 73(6):062108, June 2006.

[MBR+04] Christian Maurer, Christoph Becher, Carlos Russo, Jürgen Eschner, and Rainer Blatt. A single-photon source based on a single Ca^+ ion. *New Journal of Physics*, 6(1):94–94, July 2004.

[ME88] Peter W. Milonni and J. H. Eberly. *Lasers*. Wiley, 1988.

[MECZ99] G. Morigi, J. Eschner, J. I. Cirac, and P. Zoller. Laser cooling of two trapped ions: Sideband cooling beyond the Lamb-Dicke limit. *Physical Review A*, 59(5):3797–3808, May 1999.

[mis15] The interactive ellingham diagram. University of Cambridge, http://www.doitpoms.ac.uk/tlplib/ellingham_diagrams/interactive.php, March 2015.

[MMK+95] C. Monroe, D. M. Meekhof, B. E. King, W. M. Itano, and D. J. Wineland. Demonstration of a Fundamental Quantum Logic Gate. *Physical Review Letters*, 75(25):4714–4717, December 1995.

[MMO+07] P. Maunz, D. L. Moehring, S. Olmschenk, K. C. Younge, D. N. Matsukevich, and C. Monroe. Quantum interference of photon pairs from two remote trapped atomic ions. *Nature Physics*, 3(8):538–541, June 2007.

[MNAU02] John Martinis, S. Nam, J. Aumentado, and C. Urbina. Rabi Oscillations in a Large Josephson-Junction Qubit. *Physical Review Letters*, 89(11):117901, August 2002.

[MOL+99] J. E. Mooij, T. P. Orlando, L. Levitov, L. Tian, C. H. Van der Wal, and S. Lloyd. Josephson Persistent-Current Qubit. *Science*, 285(5430):1036–1039, August 1999.

[Moo65] G. E. Moore. Cramming More Components onto Integrated Circuits. *Electronics*, (19):114–117, April 1965.

[MRR+14] C. Monroe, R. Raussendorf, A. Ruthven, K. R. Brown, P. Maunz, L.-M. Duan, and J. Kim. Large-scale modular quantum-computer architecture with atomic memory and photonic interconnects. *Physical Review A*, 89(2):022317, February 2014.

[MS99] Klaus Mølmer and Anders Sørensen. Multiparticle Entanglement of Hot Trapped Ions. *Phys. Rev. Lett.*, 82(9):1835, March 1999.

[MSW+99] A. Y. Mao, K. A. Son, J. M. White, D. L. Kwong, D. A. Roberts, and R. N. Vrtis. Effects of vacuum and inert gas annealing of ultrathin tantalum pentoxide films on Si(100). *Journal of Vacuum Science & Technology A: Vacuum, Surfaces, and Films*, 17(3):954, May 1999.

[MSW+08] A H Myerson, D J Szwer, S C Webster, D T C Allcock, M J Curtis, G Imreh, J A Sherman, D N Stacey, A M Steane, and D M Lucas. High-Fidelity Readout of Trapped-Ion Qubits. *Phys. Rev. Lett.*, 100(20):200502, May 2008.

[MW01] Florian Mintert and Christof Wunderlich. Ion-Trap Quantum Logic Using Long-Wavelength Radiation. *Phys. Rev. Lett.*, 87(25):257904, November 2001.

[NC00] Michael A. Neilsen and Isaac L. Chuang. *Quantum computation and quantum information*, chapter 9.2.2. Cambrige University Press, 2000.

[O'B07] Jeremy L O'Brien. Optical quantum computing. *Science (New York, N.Y.)*, 318(5856):1567–70, December 2007.

[ODD+06] W. Oskay, S. Diddams, E. Donley, T. Fortier, T. Heavner, L. Hollberg, W. Itano, S. Jefferts, M. Delaney, K. Kim, F. Levi, T. Parker, and J. Bergquist. Single-Atom Optical Clock with High Accuracy. *Physical Review Letters*, 97(2):020801, July 2006.

[OLA+08] C Ospelkaus, C E Langer, J M Amini, K R Brown, D Leibfried, and D J Wineland. Trapped-Ion Quantum Logic Gates Based on Oscillating Magnetic Fields. *Phys. Rev. Lett.*, 101(9):090502, August 2008.

[OWC+11] C Ospelkaus, U Warring, Y Colombe, K R Brown, J M Amini, D Leibfried, and D J Wineland. Microwave quantum logic gates for trapped ions. *Nature*, 476(7359):181–184, August 2011.

[Pau90] Wolfgang Paul. Electromagnetic traps for charged and neutral particles. *Reviews of Modern Physics*, 62(3):531–540, July 1990.

[PBVL97] Jérôme Poirson, Fabien Bretenaker, Marc Vallet, and Albert Le Floch. Analytical and experimental study of ringing effects in a Fabry-Perot cavity. Application to the measurement of high finesses. *J. Opt. Soc. Am. B*, 14(11):2811–2817, November 1997.

[PD12] Gregers Poulsen and Michael Drewsen. Adiabatic cooling of a single trapped ion. *arXiv:1210.4309*, October 2012.

[PGCZ95] T. Pellizzari, S. A. Gardiner, J. I. Cirac, and P. Zoller. Decoherence, Continuous Observation, and Quantum Computing: A Cavity QED Model. *Physical Review Letters*, 75(21):3788–3791, November 1995.

[PMD12] G. Poulsen, Y. Miroshnychenko, and M. Drewsen. Efficient ground-state cooling of an ion in a large room-temperature linear Paul trap with a sub-Hertz heating rate. *Phys. Rev. A*, 86(5):051402, November 2012.

[RDD+06] P. Rabl, D. DeMille, J. Doyle, M. Lukin, R. Schoelkopf, and P. Zoller. Hybrid Quantum Processors: Molecular Ensembles as Quantum Memory for Solid State Circuits. *Physical Review Letters*, 97(3):033003, July 2006.

[RGR+01] H Rohde, S T Gulde, C F Roos, P A Barton, D Leibfried, J Eschner, F Schmidt-Kaler, and R Blatt. Sympathetic ground-state cooling and coherent manipulation with two-ion crystals. *Journal of Optics B: Quantum and Semiclassical Optics*, 3(1):S34–S41, February 2001.

[RKDS06] B Roth, J C J Koelemeij, H Daerr, and S Schiller. Rovibrational spectroscopy of trapped molecular hydrogen ions at millikelvin temperatures. *Phys. Rev. A*, 74(4):040501, October 2006.

[Roo00] Christian Flex Roos. *Controlling the quantum state of trapped ions*. PhD thesis, University of Innsbruck, Institute for Experimental Physics, 2000.

[RSM+14] N. Roch, M. E. Schwartz, F. Motzoi, C. Macklin, R. Vijay, A. W. Eddins, A. N. Korotkov, K. B. Whaley, M. Sarovar, and I. Siddiqi. Observation of Measurement-Induced Entanglement and Quantum Trajectories of Remote Superconducting Qubits. *Physical Review Letters*, 112(17):170501, April 2014.

[RTKL92] G. Rempe, R. J. Thompson, H. J. Kimble, and R. Lalezari. Measurement of ultralow losses in an optical interferometer. *Optics Letters*, 17(5):363, March 1992.

[SBC+11] D I Schuster, Lev S Bishop, I L Chuang, D DeMille, and R J Schoelkopf. Cavity QED in a molecular ion trap. *Phys. Rev. A*, 83(1):012311, January 2011.

[SC04] R Stutz and E Cornell. Search for the electron EDM using trapped molecular ions. *Bull. Am. Soc. Phys.*, 89:76, 2004.

[Sha48] C. E. Shannon. A mathematical theory of communication. *Bell System Tech. J.*, 27:379–623, 1948.

[SHDC13] M Shi, P F Herskind, M Drewsen, and I L Chuang. Microwave quantum logic spectroscopy and control of molecular ions. *New Journal of Physics*, 15(11):113019, November 2013.

[Sho] P.W. Shor. Fault-tolerant quantum computation. In *Proceedings of 37th Conference on Foundations of Computer Science*, pages 56–65. IEEE Comput. Soc. Press.

[Sho83] P.W. Shor. Algorithms for quantum computation: discrete logarithms and factoring. In *Proceedings 35th Annual Symposium on Foundations of Computer Science*, pages 124–134. IEEE Comput. Soc. Press, 1983.

[SHS+10] P F Staanum, K Højbjerre, P S Skyt, A K Hansen, and M Drewsen. Rotational laser cooling of vibrationally and translationally cold molecular ions. *Nat Phys*, 6:271–274, 2010.

[Sit83] J. R. Sites. Ion beam sputter deposition of optical coatings. *Optical Engineering*, 22(4):224447, August 1983.

[SK05] S Schiller and V Korobov. Tests of time independence of the electron and nuclear masses with ultracold molecules. *Phys. Rev. A*, 71(3):032505, March 2005.

[SKHR+03] Ferdinand Schmidt-Kaler, Hartmut Häffner, Mark Riebe, Stephan Gulde, Gavin P T Lancaster, Thomas Deuschle, Christoph Becher, Christian F Roos, Jürgen Eschner, and Rainer Blatt. Realization of the Cirac-Zoller controlled-NOT quantum gate. *Nature*, 422(6930):408–11, March 2003.

[SKK+00] CA Sackett, D Kielpinski, BE King, C Langer, V Meyer, CJ Myatt, M Rowe, QA Turchette, WM Itano, DJ Wineland, and C Monroe. Experimental entanglement of four particles. *Nature*, 404(6775):256–9, March 2000.

[SLM+12] J. D. Sterk, L. Luo, T. A. Manning, P. Maunz, and C. Monroe. Photon collection from a trapped ion-cavity system. *Physical Review A*, 85(6):062308, June 2012.

[SM99] Anders Sørensen and Klaus Mølmer. Quantum Computation with Ions in Thermal Motion. *Physical Review Letters*, 82(9):1971–1974, March 1999.

[SMD+13] Matthias Steiner, Hendrik M. Meyer, Christian Deutsch, Jakob Reichel, and Michael Köhl. Single Ion Coupled to an Optical Fiber Cavity. *Physical Review Letters*, 110(4):043003, January 2013.

[SRD+10] T Schneider, B Roth, H Duncker, I Ernsting, and S Schiller. All-optical preparation of molecular ions in the rovibrational ground state. *Nat Phys*, 6:275–278, 2010.

[SRK+06] P O Schmidt, T Rosenband, J C J Koelemeij, D B Hume, W M Itano, J C Bergquist, and D J Wineland. Spectroscopy of atomic and molecular ions using quantum logic. *AIP Conf. Proc.*, 862(1):305–312, October 2006.

[SRL+05] P O Schmidt, T Rosenband, C Langer, W M Itano, J C Bergquist, and D J Wineland. Spectroscopy using quantum logic. *Science*, 309(5735):749–752, July 2005.

[Ste13] Daniel Adam Steck. Quantum and atomic optics. http://atomoptics-nas.uoregon.edu/~dsteck/teaching/optics/, September 2013.

[TBJ+11] N Timoney, I Baumgart, M Johanning, A F Varon, M B Plenio, A Retzker, and Ch. Wunderlich. Quantum gates and memory using microwave-dressed states. *Nature*, 476(7359):185–188, August 2011.

[Tur38] A. M. Turing. On Computable Numbers, with an Application to the Entscheidungsproblem. A Correction. *Proceedings of the London Mathematical Society*, s2-43(6):544–546, January 1938.

[TWW10] Xin Tong, Alexander H Winney, and Stefan Willitsch. Sympathetic Cooling of Molecular Ions in Selected Rotational and Vibrational States Produced by Threshold Photoionization. *Phys. Rev. Lett.*, 105(14):143001, September 2010.

[VMD06a] I S Vogelius, L B Madsen, and M Drewsen. Probabilistic state preparation of a single molecular ion by projection measurement. *J. Phys. B: At. Mol. Opt. Phys.*, 39(19):S1259–S1265, October 2006.

[VMD06b] I S Vogelius, L B Madsen, and M Drewsen. Rotational cooling of molecular ions through laser-induced coupling to the collective modes of a two-ion Coulomb crystal. *J. Phys. B: At. Mol. Opt. Phys.*, 39(19):S1267, 2006.

[VSB+01] L M Vandersypen, M Steffen, G Breyta, C S Yannoni, M H Sherwood, and I L Chuang. Experimental realization of Shor's quantum factoring algorithm using nuclear magnetic resonance. *Nature*, 414(6866):883–7, January 2001.

[Wan12] Shannon Xuanyue Wang. *Quantum Gates, Sensors, and Systems with Trapped Ions.* PhD thesis, MIT, Department of Physics, 2012.

[WBGS08] S Willitsch, M T Bell, A D Gingell, and T P Softley. Chemical applications of laser and sympathetically-cooled ions in ion traps. *Phys. Chem. Chem. Phys.*, 10:7200–7210, 2008.

[Wes08] J. H. Wesenberg. Electrostatics of surface-electrode ion traps. *Physical Review A*, 78(6):063410, December 2008.

[WHL+11] Shannon X. Wang, Guang Hao Low, Nathan S. Lachenmyer, Yufei Ge, Peter F. Herskind, and Isaac L. Chuang. Laser-induced charging of microfabricated ion traps. *Journal of Applied Physics*, 110(10):104901, November 2011.

[WI79] D. J. Wineland and Wayne M. Itano. Laser cooling of atoms. *Physical Review A*, 20(4):1521–1540, October 1979.

[Win13] David J. Wineland. Nobel Lecture: Superposition, entanglement, and raising Schrödinger's cat. *Reviews of Modern Physics*, 85(3):1103–1114, July 2013.

[WMI+98] D.J. Wineland, C. Monroe, W.M. Itano, D. Leibfried, B.E. King, and D. M. Meekhof. Experimental issues in coherent quantum state manipulation of trapped atomic ions. *J. Res. Natl. Inst. Stand. Tech.*, 103:259, 1998.

[XVT14] Keyu Xia, Michael R Vanner, and Jason Twamley. An opto-magneto-mechanical quantum interface between distant superconducting qubits. *Scientific reports*, 4:5571, January 2014.

[YDN92] N Yu, H Dehmelt, and W Nagourney. The 31S0-33P0 transition in the aluminum isotope ion 26A1+: a potentially superior passive laser frequency standard and spectrum analyzer. *Proceedings of the National Academy of Sciences of the United States of America*, 89(16):7289, August 1992.

[YKU+06] D. D. Yavuz, P. B. Kulatunga, E. Urban, T. A. Johnson, N. Proite, T. Henage, T. G. Walker, and M. Saffman. Fast Ground State Manipulation of Neutral Atoms in Microscopic Optical Traps. *Physical Review Letters*, 96(6):063001, February 2006.

[YN13] Sang Jae Yun and Chang Hee Nam. Quantum computation with rotational states of nonpolar ionic molecules. *Physical Review A*, 87(4):040302, April 2013.

[ZBDB98] Jun-Ying Zhang, Li-Jian Bie, Vincent Dusastre, and Ian W Boyd. Thin tantalum oxide films prepared by 172 nm Excimer lamp irradiation using sol-gel method. *Thin Solid Films*, 318(1-2):252–256, April 1998.